TÉCNICO LISBOA

A New Methodology for Efficiency Scaling of Pumps-as-Turbines (PATs) and its Application to two South Africa 13kW and 100kW Micro Hydropower Systems

Ricardo Nunes Van Zeller

Thesis to obtain the Master of Science Degree in

Energy Engineering and Management

Supervisors: Prof. Paulo José da Costa Branco
Prof. João Filipe Pereira Fernandes

Examination Committee

Chairperson: Prof. Edgar Caetano Fernandes
Supervisor: Prof. Paulo José da Costa Branco
Member of the Committee: Prof. Modesto Pérez Sánchez

May 2020

Para a Avó Júju, a Yodazita e o Pugzito...

Acknowledgments

Although this thesis is written in english, I wish to express my gratitude in my native language, the portuguese.

Quero começar por agradecer aos meus orientadores, Professor Paulo Branco e Professor João Fernandes do Instituto Superior Técnico, pelo apoio que me prestaram ao longo do desenvolvimento desta dissertação: ao Professor Paulo Branco pela orientação, disponibilidade e compreensão durante o último ano; e ao Professor João Fernandes pela ajuda fornecida na fase inicial de desenvolvimento desta nova metodologia.

Agradeço ainda ao Professor Luís Gato, também do Instituto Superior Técnico, pelo aconselhamento e esclarecimento do caminho a seguir de forma a prever as curvas de eficiência de uma bomba a funcionar como turbina. Mais ainda, aproveito para agradecer ao Professor Modesto Sánchez da Universidade Politécnica de Valência pela disponibilidade no esclarecimento de diversas dúvidas relacionadas com o desenvolvimento da teoria por trás da metodologia neste trabalho apresentada.

Finalmente, agradeço a todos aqueles que me acompanharam: À paz de alma da minha família e que carrega os 3 rapazes às costas; ao que abdica de tudo por nós e que nos abana quando mais precisamos; e àquele que nos mostra todos os dias o que é ter emoção à vida... A toda a minha família, com um chi-coração especial para a minha querida Tia Jú e para o meu Tio Cabé (vamooos Tio, está feita). Ao meu par, número primo e namorada, Mariana. À Bea, à dupla Diogo e Tiago, ao Hugo, ao Joshua, ao Rodrigo e ao Zé. Resta-me assim agradecer aos meus colegas do Instituto Superior Técnico: Miguel Sousa, Gonçalo Cunha e João Melo - se superámos isto de forma tão bonita, foi porque o fizemos juntos...

Resumo

A energia hídrica é o recurso de energia renovável mais desenvolvido do mundo. Além de representar grande parte da energia renovável produzida em todo o mundo, estima-se que a maior parte do seu potencial ainda esteja por explorar, com o principal foco em micro e pequenos sistemas hidroelétricos. No entanto, a relação custo-benefício destes sistemas ainda precisa de melhorar, com as bombas-como-turbinas (PATs) a desempenhar um papel fundamental na redução dos custos de investimento.

A desvantagem deste tipo de turbomáquinas consiste no fato de os fabricantes de bombas não fornecerem, nem testarem, as condições de funcionamento de uma bomba a funcionar como turbina. Nesta tese, foi desenvolvida uma nova metodologia para prever as curvas de eficiência de uma bomba centrífuga de funcionamento inverso. Este método numérico é baseado numa teoria desenvolvida por Gülich para prever as curvas de eficiência de uma bomba centrífuga, tomando em consideração a influência da rugosidade e do número de Reynolds na escala de eficiências. Posteriormente, o método numérico foi implementado no Microsoft Excel para criar o programa Scaling of PAT Efficiency Curves, ou SPATEC.

Além disso, o modelo numérico foi aplicado a um extenso número de casos que correlacionam diferentes PATs encontradas na literatura. Como consequência, os intervalos de erro absoluto e relativo foram determinados com sucesso para as curvas de eficiência dependentes do caudal e da altura de queda. Para terminar, o mesmo modelo foi aplicado a dois sistemas reais de micro geração hídrica e a precisão da previsão de eficiências avaliada.

Palavras-chave: Energia hídrica, poupança energética, PAT, previsão de eficiências, leis de semelhança.

Abstract

Hydropower is the most mature renewable energy resource in the world. Not only it represents a large portion of the renewable energies generated in the world, as it is estimated that most of its potential is yet to be explored, with the biggest focus on micro and small hydropower systems. However, the cost-effectiveness of these systems still needs to improve, with pump-as-turbines (PATs) playing a key role on the reduction of the investment costs.

The drawback of these types of turbomachines relies on the fact that pump manufacturers do not provide, nor test, the operating condition of a pump working as a turbine. In this thesis, it was developed a new methodology to predict the efficiency curves of a reverse-running centrifugal pump. This numerical method is based on a theory developed by Gülich to predict the efficiency curves of a centrifugal pump taking into account the influence of the roughness and Reynolds number on the efficiency scaling. Later, the numerical method was implemented in Microsoft Excel in order to create the Scaling of PAT Efficiency Curves program, or SPATEC.

In addition, the numerical model was applied to an extensive number of cases that correlate different PATs found in literature. As a consequence, the absolute and relative error ranges were successfully ascertained for both the flow rate and head efficiency curves. Finally, the same model was applied to two real-life cases of micro hydropower systems and the precision of the efficiency prediction assessed.

Keywords: Hydropower, energy saving, PAT, efficiency prediction, similarity laws.

Contents

List of Tables

List of Figures

List of Acronyms

M model.

i initial estimated values prior to any iteration.

lam laminar.

p prototype.

rp resembling prototype.

st per stage.

BEP best (maximum) efficiency point.

CF Correction Factors.

DC Diameter Correction.

opt operation at maximum (best) efficiency (BEP).

PAT pump-as-turbine.

RRC Roughness and Reynolds number Correction.

SL Similarity Laws.

SPATEC Scaling of Pump-As-Turbine Efficiency Curves.

List of Symbols

D_2 Impeller outlet diameter.

D_h Hydraulic Diameter.

H Total head of a pump.

H_{th} Theoretical head in ideal flow conditions (no losses).

L Length of the flat plate.

N Rotational speed.

P_L Remaining volumetric losses apart from P_{s3} (power loss to pump leakages Q_{sp}, Q_E, Q_h).

P_a Available power.

P_u Useful power.

P_{RR} Disk friction losses.

P_{eR} Thrust balance friction losses.

P_{hyd} Hydraulic losses.

P_{mec} Mechanical losses.

P_{rec} Recirculation losses.

P_{s3} Inter-stage seal losses (throttling losses).

P_{vh} Remaining hydraulic losses apart from P_{RR}, P_{er}, P_{rec}.

P_{vol} Volumetric losses.

Q Flow that is continuously passing through the pump.

Q_E Leakage for axial thrust balance device (either occur in balance holes or pistons or disks).

Q_h Additional fluid that circulates through the pump to feed the hydrostatic bearing, flush, seal or cool the pumps.

Q_{s3} Leakage flow through the inter-stage seal.

Q_{sp} Leakage through annular seal at impeller inlet.

Re Reynolds number.

Re_{crit} Critical Reynolds number.

Tu Turbulence intensity of the flow.

U Transport velocity - tangential velocity at the tip of the blades.

Y_{th} Specific work done by impeller blades.

ΔH_{s3} Throttling loss imposed by the annular seal.

Ω Dimensionless specific speed.

Ψ Head coefficient.

ϵ Equivalent sand roughness or only roughness.

ϵ_a Arithmetic mean roughness.

ϵ_{max} Maximum roughness dept.

η Overall efficiency.

η_{hyd} Hydraulic efficiency.

η_{mec} Mechanical efficiency.

η_{vol} Volumetric efficiency.

η_{vol} Volumetric efficiency.

λ_r Pipe friction coefficient.

ν Kinematic viscosity.

ω Angular velocity.

ρ Specific mass or density of the fluid.

ε/L Relative roughness of a flat plate.

ζ_F Hydraulic friction losses.

ζ_M Hydraulic mixing losses.

a Constant parameter for the flow leakage Q_{sp}.

c_f Flat plate friction coefficient.

c_u Circumferential component of the absolute velocity.

c_{eq} Equivalence factor.

$f\eta_{hyd}$ Influence of the Reynolds number and roughness on the hydraulic losses.

$f\eta_{mec}$ Influence of the Reynolds number and roughness on the mechanical losses.

$f\eta_{vol}$ Influence of the Reynolds number and roughness on the volumetric losses.

f_L Leakage correction factor.

f_R Roughness correction factor.

f_q Number of impeller eyes per impeller.

f_H Correction factor for head.

f_Q Correction factor for flow rate.

f_η Correction factor for efficiency.

f_{geo} Geometrical factor.

j Characteristic parameter of the leakage correction factor.

k_o Disk friction coeffcient with zero leakages (Q_{sp} = 0).

k_s Sand roughness.

k_{RR} Disk friction coefficient.

m Constant parameter for the flow leakage Q_{sp}.

r_2 Impeller outlet radius.

r_w Casing radius.

s_{ax} Axial clearance between impeller's shrades and the casing.

t_{ax} Axial casing part in impeller's side wall gap.

w Relative velocity.

z_A Hydraulic loss at the casing outlet.

z_E Hydraulic loss at the casing inlet.

z_H Parameter as a function of the presence of balance holes in the pump.

z_{La} Hydraulic loss at the impeller.

z_{Le} Hydraulic loss at the diffuser.

z_{sp} Hydraulic loss at the volute.

z_{st} Number of stages.

Chapter 1

Introduction

The global electricity consumption and consequent demand have been increasing as a result of the population growth and the socioeconomic development within nations [1]. Not only is the total amount of generated electricity insufficient to feel everyone's needs [2], as there is almost 850 million people around the world that lack electricity access [3]. In addition, researchers are seeking for improved techniques to overcome some relevant issues associated with power generation, such as environmental impacts and energy production costs, that mainly arise from fossil fuels. One of the most suitable solutions is thought to be renewable energy.

Since the last century, many researchers have been focusing on new and alternative ways to generate clean energy. From solarpower, windpower, fuel cells, biofuels and many other renewable energy sources, hydropower is unarguably the most important source of energy generation [4]. In many developing countries, specially within the Sahara African region, small and micro hydropower systems represent a significant solution to generate electricity. An energetically efficient solution in these types of systems, is the usage of a conventional turbine to transform the kinetic energy of a fluid into electrical energy. However, the total investment share that corresponds to the eletromechanical components simply does not make their implementation attractive enough, specially for small hydropower [5], [6], [7], [8], [9] and [10].

The solution relies on the idea of pumps working as turbines (also known as *pump-as-turbine* (PAT)). Whenever reverse-runned, pumps can generate and recover power in small and micro hydropower schemes with very satisfying efficiencies. Their relatively simple layout, accessible purchase cost and "off-the-shelf" worldwide readiness are some advantages of pumps-as-turbines. In addition, lower maintenance efforts, high spare parts (for example seals and bearings) availability and a particularly straightforward installation (capable of adapting to standard pipes and fittings), naturally promote the choice of PATs over hydraulic turbines. Moreover, the wider flow and head operation ranges along with the extensive number of standard sizes represents an added value to pumps. Finally, the fact that a pump and a motor set can be purchased to operate as a turbine and generator, respectively, immediately reduces the price of the eletromechanical equipment and thus, increases the worthiness of the project. At an economic point of view, reverse-running pumps are able to reach a capital payback period lower than 2

years, for capacities varying between 5 kW and 50 kW [11], [12]. However, in the majority of the cases, the payback period of PATs varies between 7 to 8 years.

Despite the advantages associated with the implementation of PATs in hydropower schemes, there is still a significant drawback that researchers have been trying to overcome for a while: to predict the actual PAT performance for a specific point of operation, specially the *best (maximum) efficiency point* (BEP). This problem arises from the fact that pump manufactures do not provide, nor test, any pump characteristics running in turbine-mode. From numerical models, to experiments or theoretical procedures, there have been several methodologies applied to predict the characteristics of a PAT [8], [9], [10], [11], [12], [13] and [14]. Additionally, a few researchers on the area, such as Stepanoff, Childs, Sharma, Wong, Williams, Alatorre-Frenk and others, have formulated some correlations based on theoretical approaches. However, results felt short on expectations and, in general, it were found deviations between experimental and theoretical results of 20% or higher [15].

In this thesis, it is presented an alternative methodology to predict PAT performance curves. Based on turbine-mode operating points of several PATs, the efficiency curves of a particularly intended PAT might be achieved (for a specific speed between 0.12 and 1.18, as this was the range available in the database used in this thesis). This work is based on a methodology developed by [16] to predict efficiency curves for geometrically similar centrifugal pumps, taking into account the influence that the roughness and the Reynolds number have on the performance.

In chapter 2, it is provided an overview related to the published knowledge on PATs, comprehending their geometrical characteristics, applicability limits and examples of application.

Chapter 3, covers the non-dimensional theory that is utilized to obtain information regarding the efficiency curves of a certain PAT, through the characteristics of a geometrically similar PAT.

Alike the flow in a pipe or a flat plate, energy losses (i.e. mechanical, hydraulic and volumetric losses) in a turbomachinery are affected by the roughness and Reynolds number. In chapter 4, the distinct forms of losses inherent to a centrifugal pump are clarified so that in chapter 5 they can be used to formulate the reasoning behind the *Scaling of Pump-As-Turbine Efficiency Curves* (SPATEC) program developed in this thesis. In addition to the explanation provided in chapter 6 regarding SPATEC, it is also described the collecting and treatment of the data used in this work.

Moreover, in chapter 7, an extensive analysis of the errors associated with the prediction of the PAT efficiency curves is carried. Both specific speed and diameter deviations are evaluated and the differences between predicted and experimental results assessed. In addition, an extensive analysis is applied on three distinct predicting cases: an accurate case, a special case and an inaccurate case. At the end of the chapter, a sensitivity analysis is also carried out in order to understand the impact that a 10% variation on the roughness and Reynolds number has on the efficiency scaling.

To test the feasibility of the proposed methodology, in chapter 8 SPATEC is applied to two independent cases of micro hydropower systems that use a PAT to generate power.

Finally, chapter 9 presents the most relevant conclusions to take from this thesis, as well as future work that might be interesting to study in order to improve the developed work.

Chapter 2

Background

A pump-as-turbine is a pump that runs with rotation speed and flow direction in an opposite way to that defined for the operation mode as a pump. In this chapter, it will be seen how did the concept of a PAT emerged, what are its characteristics and application limits, and also in what type of projects can they be useful.

2.1 Origin

The pump operating as a turbine is though to have had its first appearance back in 1926 in Orchard Mesa (Colorado, USA), much earlier than the publication of the initial formal studies on pump-as-turbines [17]. Curiously, the discovery of the turbine mode of a pump was unintentional. During the experimental analysis of a pump's water-hammer in large pumping stations, D. Thoma and C. P. Kittredge found that a reverse-running pump was, in fact, an efficient turbine [18]. Subsequently, they also proposed the possibility of using the same turbomachine to work as both pump and turbine in storage stations [19]. Moreover, it was [20] turn to suggest the usage of a pump to solely work as a turbine.

As stated above, the development and dissemination of the reversible pump technology that followed its discovery, was a result of the research focused on the water-hammer in pumping stations and on pump-turbine schemes. It is interesting to perceive that, alike pump-as-turbines, many other low-cost discoveries from distinct areas are the outcome of the research and development on advanced technologies [21].

2.2 Geometrical characteristics of a PAT

On the contrary to conventional turbines, PATs do not exhibit any type of regulation, which is a natural consequence of running a pump in the opposite direction. Additionally, it was also verified through the comparison of a PAT and an intentionally unregulated turbine that the former has a larger runner with the blades' curvature in a opposite direction, Fig. 2.1.Despite the extra cost associated with a larger runner and the small efficiency loss inherent to the unregulated operation mode, PATs still manage to be

cost-effective due to its mass production.

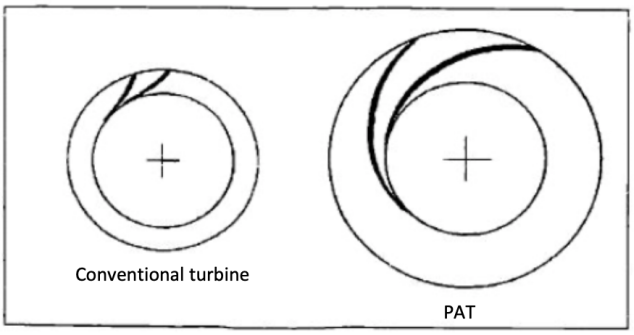

Figure 2.1: Geometrical differences between a conventional turbine (left) and a PAT (right) (adapted from [22]).

The size differences verified between a PAT and a turbine with similar operating characteristics result from the PAT defaulted design to operate in pump mode. The flow through a pump is associated with flow separation issues and diffusion losses. To avoid this issues, the pump's impeller must be bigger than the turbine's impeller (around 30% to 40% bigger), with long and gradually diverging channels. In addition, reversed curvatures and small angles at the tip of the blades are also some geometrical characteristics that must be adopted to increase the stability of the flow. Such aspect is not verified with such influence in a turbine.

Even though pumps can work as turbines with reasonable efficiencies, the opposite is not unquestionably true. The fact that turbines have relatively short channels and large blades angles would result in an excessive deceleration and an unsteady flow. As such, pumps-as-turbines are much more likely to be used than turbines operating as pumps. For example, in energy storage schemes, several purpose-made reversible machines (pump-turbines) are manufactured with a geometry closer to a pump, than a turbine [15], [23], [22], [24], [25], [26], [27] and [28].

2.3 PAT application limits

2.3.1 Power limits

The maximum power limit of a PAT varies according to different authors, ranging from as low as 15 kW to several megawatts (MW). In the opinion of the researchers from [29] or [30], an immediately available PAT that does not need to be specially manufactured to suit particular specifications can only be found with maximum power of 100 kW and 250 kW, respectively. However, there are still other authors who claim that it is more cost-effective to produce PATs with higher power than conventional turbines, even if the former have to be manufactured to order: in the case of [31], power capacities go up to 1.5 MW;[32] sets an upper limit of 2 MW; as for [33], power capacities can reach values of several MW with various 500 kW machines in parallel; and finally, [34] even exemplifies the Swiss hydropower station composed by seven 931 kW PATs connected in parallel that uses a cheap and solid pump model that is frequently applied in South African gold mines and Gulf countries. Opposing these high power

PAT limits, there are a few other countries that, due to the scarcity of pump turbomachines and a great amount of locally-made cross-flow turbines, hardly own PATs with power capacities superior to 15 kW , for relatively low specific speeds. Nepal and Pakistan are some examples of the countries where this problem is frequent [35].

2.3.2 Specific speed limits

The specific speed Ω is a non-dimensional parameter of turbomachines used to understand which flow properties (namely, flow rate Q and head H) are accepted to circulate through the machine with a particular rotational speed N. By analyzing the specific speed equation (i.e. Eq. 2.1), it is easily perceived that low specific speeds are associated with high head potentials and low flow rates, whilst low heads and high flow rates induce high specific speeds.

$$\Omega = \frac{\omega Q^{1/2}}{(gH)^{3/4}} \tag{2.1}$$

with g representing the gravitational constant given approximately by 9.81 m^2/s, $\omega = 2\pi \cdot N/60$ the rotational speed in rads/s, Q the flow rate in m^3/s and H the head in m.

As a consequence of defining the flow properties with which the turbomachine operates, the specific speed also influences the geometry of the impeller is designed, but this will be clarified later, in chapter 3. Meanwhile, it shall be understood the applicability of PATs according to their specific speed.

In a general way, it is not possible to ascertain a particular range to define lower and upper specific speed limits of applicability of PATs. This results from the fact that these limits not only vary from country to country, but also according to the availability and cost of pumps and turbines.

When it comes to lower specific speeds, researches from [36] defend that PATs cannot compete with Pelton turbines for $\Omega \leq 0.2$. The former, have not only higher manufacturing costs, but higher maintenance costs as well, [37]. However, researchers from [34], [38], [39] and [40] state that multistage PATs can still be a cost-effective solution in countries where the cost of manufacturing is competitive enough with impulse turbines (i.e. Pelton turbines). In this way, countries like Nepal and Peru, that are masters in the manufacture of Pelton turbines, are most likely to have lower application limit around 0.2, just as inferred by [36].

Alike radial PATs, axial PATs also have their disadvantages: apart from being more costly than other pumps and lacking experimental information when operating in turbine-mode [41], axial PATs also present a blade shape that considerably impairs the stability of the flow once it was designed to operate in pump-mode [42]. In addition, their bias towards cavitation and low efficiencies led [38] to suggest the possibility of using several parallel-connected mixed-flow PATs rather than axial PATs. In fact, researcher from [38] still found that in the United States of America, a set-up of five mixed-flow PATs was cheaper than a typical turbine with similar operating characteristics. Besides, in the case of a single PAT failure or low-flow seasons, the system is still capable of generating power. In conclusion, high specific speed axial-flow or mixed-flow PATs might be the most suitable PAT types to install in low head hydropower sites, that represent most of the small hydro potential in the world [43].

2.4 Examples of applications

The reduced manufacturing cost, the easy handling and the ability to handle abrasive or corrosive liquids led to the wide and distinct variety of PAT applications:

- A well known hydropower scheme where PATs are applied is the run-of-river system. Water is diverted through a weir and flows inside a penstock until it reaches a PAT at a lower water level. Thereafter, a connection between the rotating PAT and a generator allows the transformation of the water's kinetic energy into electrical energy;
- Sewage and water supply systems are another type of systems where PATs can be installed [30], [44], [45] and [46]. It is thought that this type of energy recovery might have a potential of 64 MW in Germany [47];
- Frequently, PATs are also deployed in lower branches of pumping stations where a single pump must elevate water up to a different water level, just like what happens in irrigation stations [48];
- Alternatively to the last two hydropower schemes, PATs might even replace actual pumps in irrigation and sewage systems to operate in both pump and turbine modes throughout the year [49]. The system described by [50] is a good example of these types of schemes, with three 4.5 MW pumps.
- In addition, PATs may also be direct coupled to pumps so that the latter delivers the fluid to an upper level as a consequence of the rotation of the former [51], [52], [53] and [54]. Some examples of these types of systems may be found in [55] and [56]. Later in this work it will be seen an example of this type of scheme (chapter 8.2.2);
- In the industrial sector, PATs are also utilized in many applications to drive generators or machines: for explosive environments PATs are preferred to eletrical drives [48], as for the oil-related industry, they can be applied in wells [30], gas and oil separation plants [41], synthetic ammonia production facilities and refineries [30] and [57]. It is interesting to point that, in many of these applications, PATs deal with the circulation of two-phase flows, being able to harness, even if with a low efficiency, the energy that is contained in the gaseous part of the solution [58], [59], [60], [61], [62], [63], [64], [65], [66], [67] and [68].
- Lastly, PATs have even been identified in characteristic systems such as mine-cooling applications (see for instance [37] and [69]) and reverse osmosis schemes (for example [30] and [70]).

Chapter 3

Dimensionless coefficients and similarity laws

The application of dimensional analysis is most useful in the scientific field of turbomachines. In this chapter, it is seen how this theory can be applied to determine the operating curves of a certain pump. Perceiving how the characteristics of a pump are determined based on the characteristics of a geometrically similar pump is the first step to understand the numerical model developed in this thesis.

3.1 Pi or Buckingham's theorem

Consider a variable Q_1, as function of $(n-1)$ independent variables $Q_2, Q_3, ..., Q_n$, which expresses a certain physical meaning due to the mathematical relation presented in Eq. 3.1, or in Eq. 3.2.

$$Q_1 = f(Q_2, Q_3, ..., Q_n) \tag{3.1}$$

$$F(Q_1, Q_2, Q_3, ..., Q_n) = 0 \tag{3.2}$$

In addition, let p be the number of fundamental dimensions necessary to defined the physical quantities involved in the mathematical relations expressed by Eqs. 3.1 or 3.2. For example, if those dimensions are represented by the mass M, the length L and the time T, then $p = 3$.

To simplify the mathematical problem, an initial group composed by p variables (out of the n variables) must figure, at least one time, each fundamental dimension. Subsequently, the remaining $(n-p)$ variables are expressed in the form of non-dimensional parameters generated through the power rating product of the respective dimensional variable and the initial group of variables. In this way, Eqs. 3.1 and 3.2 are rewritten as Eq. 3.3 shows [71]. This simplification methodology is known as the Buckingham's theorem.

$$\Phi\left(\Pi_1, \Pi_2, ..., \Pi_{n-p}\right) = 0 \tag{3.3}$$

3.2 Variables that characterized the operation of a turbomachine

In a pump with incompressible flow there are different types of variables that characterize its operation, such as control variables, fluid properties and geometric variables.

The control variables can be interpreted as parameters that are deliberately altered to regulate the operation of the turbomachinery, for example, the flow rate Q and the rotational speed of the rotor N. Consider the particular case of a system composed by a pump connected to a variable speed electric motor and with an adjustable opening valve at the pump outlet. By independently changing the flow rate and the rotation speed, it is possible to obtain all operating points within the machine's operational limits. Naturally, for each set of values Q and N, correspond characteristic values of the torque L transmitted by the shaft, head H and power P supplied by the motor. It should also be noted that, in the same way that Q and N were fixed, L it could also be restricted instead of N and, H instead of Q, thereby making Q and N dependent variables [71].

As for the properties of the fluid, it is easily noticed that properties such as the specific mass ρ and the viscosity μ considerably affect the operating characteristics of the turbomachine.

Finally, when it comes to geometric variables, changing the turbomachine clearly implies a different functioning of the system. Its operation not only depends on the absolute dimensions of the machine (for example, the outlet impeller diameter), but also on a large number of angles and dimensionless relations α, β, etc. In fact, some of these parameters are often adjusted in order to make the turbomachine operate under different conditions, just like the case of the fixing angles of the rotor or stator blades for certain types of turbomachines.

The Buckingham's theorem, along with the control variables, the fluid properties and the geometric variables that characterize a turbomachine, allow the determination of the remaining variables that are also present in the system, but are dependent of the dimensional parameters. Therefore, the torque L transmitted by the turbomachine shaft can, for example, be written according to Eq. 3.4.

$$L = f(Q, N, \rho, \mu, ..., D_2, \alpha, \beta, ...) \tag{3.4}$$

If Buckingham's theorem is applied to Eq. 3.4, assuming MLT as the fundamental dimensions of the system and D_2, N and ρ as the primary variables (i.e. p = 3), then it comes that the torque can be expressed by the Eq. 3.5 shown below [71].[1]

$$\frac{L}{\rho N^2 D_2^5} = \phi\left(\frac{Q}{ND_2^3}, \frac{\rho N D_2^2}{\mu}, ..., \alpha, \beta, ...\right), \tag{3.5}$$

with $[D_2] = L$, $[N] = T^{-1}$ and $[\rho] = ML^{-3}$. In addition, $\frac{L}{\rho N^2 D_2^5}$ characterizes the torque coefficient, $\frac{Q}{ND_2^3}$ the flow rate coefficient and $\frac{\rho N D_2^2}{\mu}$ the Reynolds number, once ND_2 affects proportionally the transport velocity at the tip of the blades and so, is related to the flow velocity.

Equation 3.5 expresses the torque behavior for the possible types of operation of a turbomachine.

[1] Notice that the definition of three fundamental properties resulted in a (n-3) variable system in Eq. 3.5.

However, for this equation to be more useful it is essential to disregard or assume certain dimensionless parameters as constant: knowing that dimensionless parameters are constant in a family of geometrically similar turbomachines, it is deemed that α, $\beta \cdots$ can be omitted from Eq. 3.5; in addition, the Reynolds number is disregarded taking into account that its impact on the turbomachine functioning is relatively insignificant when compared to the impact of the flow coefficient (unless there is cavitation, but that will not be deepened in this thesis, see chapter 10 of [71]). Therefore, the law that conducts the torque of a family of geometrically similar turbomachines can be expressed simply by a curve dependent on the flow coefficient, Eq. 3.6.

$$\frac{L}{\rho N^2 D_2^5} = \phi\left(\frac{Q}{N D_2^3}\right) \tag{3.6}$$

3.3 Characteristic operating curves

Analogously to the binary, any other dependent variable can also be defined as a function of dimensionless parameters. Therefore, it is concluded that a family of geometrically similar turbomachines is represented, in general, by Eq. 3.7 [71].

$$Y = f(X) \tag{3.7}$$

with the dependent variable inserted in the dimensionless group Y and with the independent variables present in X and Y given by two control variables (for example Q and N), a fluid property (specific mass ρ) and a geometric variable (impeller diameter D_2). Note that this simple way of characterizing the operation of a turbomachine is only valid if all the fluid properties at the exception of the specific mass ρ are disregarded. Latter in this work, it will be seen that several correction factors must be applied to these laws if the viscosity μ is not neglected.

The dimensionless parameters that most often characterize the X and Y groups are the following:

$$\frac{L}{\rho N^2 D_2^5} \qquad Torque\ coefficient$$
$$\frac{F}{\rho N^2 D_2^4} \qquad Force\ coefficient$$
$$\frac{P}{\rho N^3 D_2^5} \qquad Power\ coefficient$$
$$\frac{gH}{\rho N^2 D_2^2} \qquad Head\ coefficient$$
$$\frac{Q}{\rho N D_2^3} \qquad Flow\ rate\ coefficient$$
$$\eta \qquad Efficiency$$
$$\Omega = \frac{NQ^{1/2}}{(gH)^{3/4}} = \frac{NP^{1/2}}{\rho^{1/2}(gH)^{5/4}} \qquad Specific\ Speed$$

The fact that these parameters are non-dimensional implies that they do not depend on the unit system considered, as long as it remains consistent. It might happen that some of these non-dimensional parameters are transformed into dimensional variables by neglecting some constant factor that is inherent to themselves. This is the case of, for example, the specific mass ρ in hydraulic turbines and

the gravitational acceleration g in the head coefficient $\frac{gH}{N^2D_2^2}$. However, dimensionalized parameters naturally represent an inconvenience for countries to compare their turbomachines with turbomachines from countries, whose curves are dimensionalized with a distinct unit systems. In the mean time, dimensionless variables allow the characterization of a single curve for a family of geometrically similar turbomachines, instead of representing a curve for each turbomachine considered. Despite the undesirable exchange of pumps between countries with different units systems, pumps with dimensionalized curves are still very useful for pump operators in the theoretical study of several projects [71].

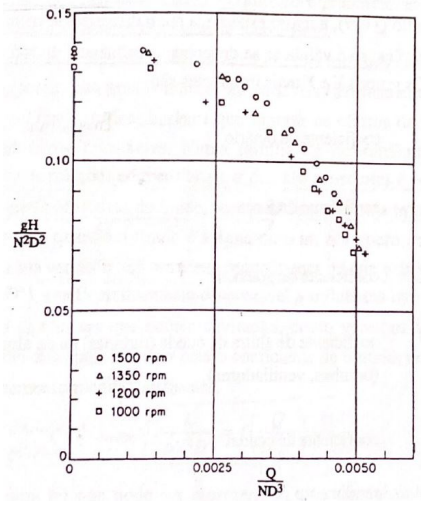

Figure 3.1: Dimensionless representation of the head coefficient as a function of the flow for a pump tested in the laboratory (adapted from [71]).

See Fig. 3.1, which represents the response of the head coefficient of a pump as a function of its flow coefficient. Note that the graphical representation of the four operating conditions is the same for each case, even though the impeller rotational speed varies [2]. However, if it was opted to illustrate the results obtained in the laboratory through dimensional parameters, for example H = F (Q), then instead of having four curves forming a single curve, we would have four curves with considerably significant deviations. Consider now that the same experimental tests are applied to another geometrically similar pump, but with different absolute dimensions. Then, the dimensionless representation of the new curves would be equal to the graphical representation of the initial pump. The dimensional representation, on the other hand, would imply eight different curves, all distinct from each other.

The exchange between dimensional and non-dimensional curves is rather straightforward: both the transformation from the dimensionless curve to the dimensional curve, and the transformation from the dimensional curve to the dimensionless curve, only require the knowledge of two characteristics of the pump's operation, for example, the diameter D_2 and the rotation speed N.

The ability to exchange between dimensional and non-dimensional curves also allows the modification of a certain pump characteristics without incurring to the dimensionless representation of the pump curve. From Fig. 3.2, observe point P_A from curve A which has a rotational speed N_A equal to 1000 rpm, a flow rate Q_A, a head H_A and an impeller diameter D_A. Its characteristics allow the definition of

[2]The slight deviations between the curves is a consequence of disregarding the influence of the Reynolds number. Nonetheless, it is still acceptable to state that the four curves represent a single family of geometrically similar turbomachines.

the flow rate and head coefficients, $\frac{Q_A}{N_A D_{2A}^3}$ and $\frac{gH_A}{N_A^2 D_{2A}^2}$, respectively [71].

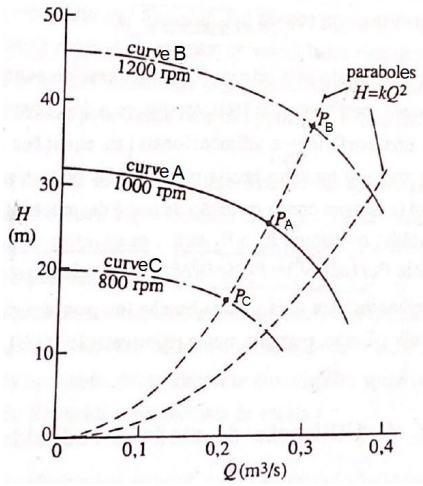

Figure 3.2: Characteristic curves $H(Q)$ of a pump, for three values of rotational speed. There are also represented two paraboles of the type $H = kQ^2$ (adapted from [71]).

Knowing that in curve B there must be a point P_B with the same dimensionless characteristics of point P_A, it comes that the flow rate and head[3] coefficients are the same for both points, Eqs. 3.8 and 3.9, respectively.

$$\frac{Q_B}{N_B D_{2B}^3} = \frac{Q_A}{N_A D_{2A}^3} \tag{3.8}$$

$$\frac{gH_B}{N_B^2 D_{2B}^2} = \frac{gH_A}{N_A^2 D_{2A}^2} \, , \tag{3.9}$$

Taking into account that the dimensionless transformation is applied for the same pump, meaning, with the same diameter (i.e. $D_{2A} = D_{2B}$), the previous equations result in Eq. 3.10.

$$\frac{Q_B}{Q_A} = \left(\frac{H_B}{H_A}\right)^{1/2} = \frac{N_B}{N_A} \tag{3.10}$$

Therefore, by knowing the values of Q_A, H_A, N_A and N_B, the characteristic coordinates of point P_B (i.e. Q_B and H_B) are attained.

Equation 3.10 demonstrates that, in the plane (Q, H), all operating points characterized by the same dimensionless coefficients, accent on a second degree polynomial curve, see Fig. 3.2 above. Such points are defined as dynamically similar points, that is, points whose current lines have the same orientation and where velocities, accelerations and forces are distinguished only by constant proportionality factors.

If the characteristics of a pump are determined by the characteristics of another geometrically similar pump, but with different absolute dimensions, then the diameters in Eqs. 3.8 and 3.9 do not cancel each other out. Thus, Eq. 3.10 is no longer valid and the Eqs. 3.11 and 3.12 are considered. These types of

[3]Notice that the dimensionless parameters may vary according to the author. For example, Gulich assumes an head coefficient equal to $2gH/N^2D_2^2$, that will be the value assumed in the development of this thesis.

equations, which relate two geometrically similar turbomachines, are known as similarity or affinity laws.

$$\frac{Q_B}{Q_A} = \frac{N_B}{N_A}\left(\frac{D_{2B}}{D_{2A}}\right)^3 \tag{3.11}$$

$$\frac{H_B}{H_A} = \left(\frac{N_B}{N_A}\right)^2\left(\frac{D_{2B}}{D_{2A}}\right)^2 \tag{3.12}$$

Analogously to the flow rate and head coefficients, which are the same for both point P_A and point P_B, it can be concluded from Eq. 3.7 that any other dimensionless coefficient corresponding to the operating point P_A is also equal to the respective dimensionless coefficient associated with point P_B (not forgetting that the influence of the number of Reynols was negligible). This means that similarity laws can also be written for any dimensionless coefficient. Below, Eqs. 3.13, 3.14 and 3.15 represent other well-known similarity laws that will later be used in this thesis.

$$\eta_B = \eta_A \tag{3.13}$$

$$\frac{P_B}{P_A} = \frac{\rho_B}{\rho_A}\left(\frac{D_{2B}}{D_{2A}}\right)\left(\frac{N_B}{N_A}\right)^3 \tag{3.14}$$

$$\Omega_B = \Omega_A \tag{3.15}$$

From all dimensionless parameters, the most frequently used to correlate geometrically similar pumps is the specific speed $\Omega = \frac{NQ^{1/2}}{(gH)^{3/4}}$. Despite being a dimensionless parameter, it can often be written in different dimensional forms as long as the used system of units is coherent, see detailed information in [16]. As previously mentioned in chapter 2, the specific speed is also a characteristic parameter of turbomachines: it defines the geometry with which a machine must be designed.

These similarity laws may lead to modified similarity laws, varying from author to author. Later in this thesis, it will be used the modified similarity laws from [16] that considers particular factors essential for the efficiency scaling: the specific mass ρ of the fluid and the number of stages z_{st} in a centrifugal pump represent the factors in question.

3.4 Use of reduced models

The fact that geometrically similar turbomachines imply similar dimensionless operating curves, allows the estimation of the dimensionless curve of a reduced model to perceive the behavior of the respective prototype in the conditions of the system that is intended to design. However, it is important to realize that, because the influence of factors such as the Reynolds number and the scale effects have been neglected, the efficiency curve of the prototype will present different results from those that are verified in reality. The scale effects result from the natural impossibility of the prototype to obtain a geometry perfectly similar to that of the model. For example, the relative roughness and axial clearances between the rotor and the stator are absolute dimensions that change depending on the size of the turbomachine; later on, the prediction of a PAT's operating curves will be studied, taking into account each of these factors.

Chapter 4

Power Balance and Efficiencies

Whenever operating with a turbomachine, there are losses associated with the process of machining. In other words, the useful power P_u is lower than the actual power P_a available at the shaft. In this chapter, it will be seen the different types of losses that may occur in a centrifugal pump and how can they be determined.

According to [16] , these losses are dissipated into heat and can be divided into mechanical losses P_{mec}, volumetric losses P_{vol}, disk friction losses P_{RR}, thrust balance friction losses P_{eR}, throttling losses P_{s3}, hydraulic losses P_{hyd} and recirculation losses P_{rec}.

Such loss-arrangement can often be considered as complex and confusing. In this thesis, an alternative reasoning is taken into account with the aim of developing a more intuitive arrangement. The losses are now divided in three major types of losses: mechanical P_{mec} , volumetric P_{vol} and hydraulic losses P_{hyd} . The volumetric losses are divided into throttling losses P_{s3} and leakages losses P_L that represent leakages through balances holes, annular seals and others (later, these losses will be deepened). In addition, the hydraulic set of losses embraces disk friction losses P_{RR} , thrust balance friction losses P_{er}, recirculation losses P_{rec} and the remaining hydraulic losses P_{vh} that do not arise from any of the mentioned losses. Figure 4.1 shows the modified losses scheme.

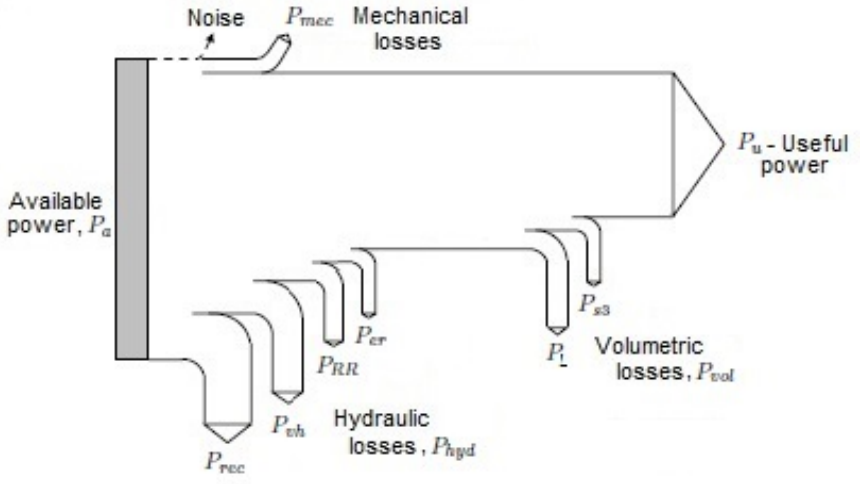

Figure 4.1: Distinct types of losses verified in a centrifugal pump (analogous scheme for a PAT) (adapted from [16]).

4.1 Mechanical losses

Inside a centrifugal pump, mechanical losses are due to the friction forces exerted on the radial bearings, axial bearing and shaft seals. These losses can vary according to the design of the pump once its mechanical seal can be replaced by a stuffing box and its anti-friction bearings by the journal-type bearing.

Mechanical seals and stuffing boxes (also known as gland packing) are design to prevent the fluid from seeping outside the pump casing towards the motor, Fig. 4.2(a). As for the anti-friction and journal (plain) bearings, their intent in a centrifugal pump is to allow the shaft to rotate with the minimum friction possible, Fig. 4.2(b). Since these do not establish any contact with the transported fluid (meaning, its losses do not heat up the fluid), mechanical losses are also denominated external losses.

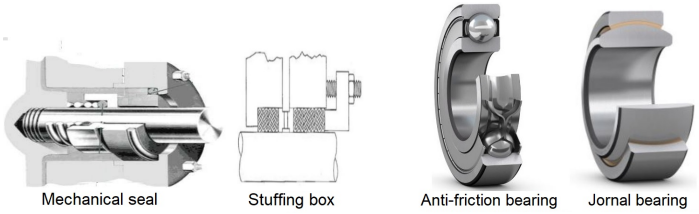

Figure 4.2: (a) Mechanical seal and stuffing box (b) anti-friction and journal bearings (adapted from [72], [73] and [74]).

Opposing large pumps that can achieve mechanical efficiencies η_{mec} of 99.5%, small pumps (with power capacities below 5 kW) might consume a significant amount of the coupling power. If no documentation is available, [16] states that the mechanical losses can be calculated with respect to Eq. 4.1.

$$\frac{P_{mec}}{P_{opt}} = 0.0045 \left(\frac{Q_{Ref}}{Q}\right)^{0.4} \cdot \left(\frac{N_{Ref}}{N}\right)^{0.3} \tag{4.1}$$

with $Q_{ref} = 1$ m^3/s, $N_{ref} = 1500$ rpm and P_{opt} representing the pump power at its best efficiency point.

4.2 Volumetric losses

For the general case of pumps, fans and compressors, manufacturers tend to use closed-type impellers, although semi-open and open impellers can be of great use as well, Fig. 4.3. These last two types, which are known for lacking the front and both shrouds, respectively, require a much lower clearance between the casing and the impeller so that the fluid's passage from the pressure to the suction surface remains as lower as possible (something that does not happen with closed impellers). If not prevented, high clearances can cause high losses of kinetic energy and, consequently, significant reductions of the head and efficiency [75].

Although closed impellers are designed with the front and rear shrouds, this does not prevent leakages through the casing and front shroud. In fact, behind the rear shroud there is an annular seal to

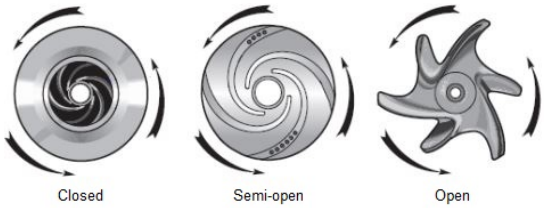

Figure 4.3: Closed, semi-open and open impellers (adapted from [76]).

balk the fluid's passage and throttle it (i.e. the mechanical seal or stuffing box illustrated previously in Fig. 4.2(a). The leakage flow Q_{sp} that returns to the impeller inlet is then expressed by Eq. 4.2, [16].

$$\frac{Q_{sp}}{Q_{opt}} = \frac{a\ z_H}{(52.9\ \Omega)^m} \qquad with \qquad \begin{cases} a = 4.1 \quad m = 1.6 \quad for \quad \Omega < 0.510 \\ a = 0.15 \quad m = 0.6 \quad for \quad \Omega \geq 0.510 \end{cases} \tag{4.2}$$

In Eq. 4.2, a and m represent constant variables that depend on the non-dimensional specific speed Ω of the pump. In addition to the annular seal leakages, there are also leakages through the axial thrust balancing device that is used to counter-balance the axial thrust imposed by the flow on the impeller. These types of devices are known as balance pistons, balance disk or balance holes. The latter consist of pierced holes through the rear shroud to generate individual impeller balancing. If this is the type of balance device present in the pump, then the parameter z_H is equal to two. Otherwise, $z_H = 1$.

These axial thrust balancing leakages Q_E return to the impeller near the leading edge of the blades. Later on this work, these leakages will be assumed as equal to the leakages through the annular seal, $Q_{sp} = Q_E$.

Finally, in order to flush, seal or cool a turbomachine or even feed a hydrostatic bearing, a supplementary fluid Q_h is transferred within several branches of the pump.

The total power required to pump the annular seal leakages, the axial thrust balancing leakages and the supplementary fluid leakages[1] is stipulated to be given by Eq. 4.3, [16].

$$P_L = \rho\ g\ H_{th}\ \left(Q_{sp} + Q_E + Q_h\right) = \rho\ g\ H_{th}\ Q\ \frac{(1-\eta_{vol})}{\eta_{vol}} \tag{4.3}$$

with H_{th} representing the theoretical head of the flow in ideal flow condition (i.e. no losses), η_{vol} the volumetric efficiency, ρ the density of the fluid and g the gravitational constant equal to 9.81 m/s^2.

4.2.1 Leakage losses through annular seals

As referred above, in closed impellers, annular seals are used to restrict flow leakages that circulate from the impeller outlet to the impeller inlet and prevent wear of its surrounding components. These seals are composed by a casing wearing and a rotating inner cylinder, mostly known as impeller wearing, see Fig. 4.4.

[1] Notice that the volumetric losses under discussion do not include the inter-stage losses P_{s3} defined in the begining of chapter 4. In fact, the total volumetric efficiency η_{vol} must take them into account as will be seen later.

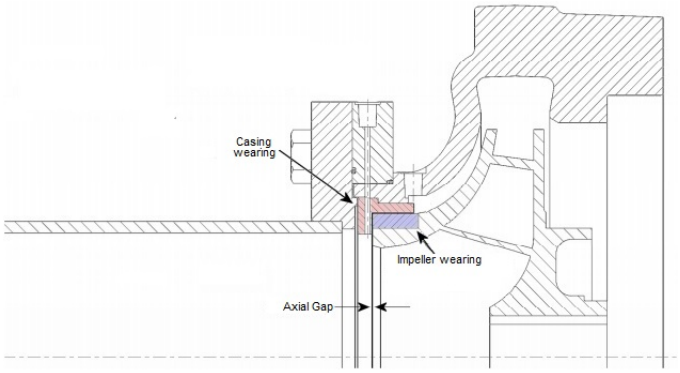

Figure 4.4: Example of the casing and impeller wearings in a centrifugal pump (adapted from [77]).

The resistance of an annular seal not only depends on the roughness of its walls but also on its geometry. As a result, these components can assume a variety of designs, from simple smooth surfaces to geometries with different types of grooves and isotropic patterns, only to increase the flow resistance, Fig. 4.5.

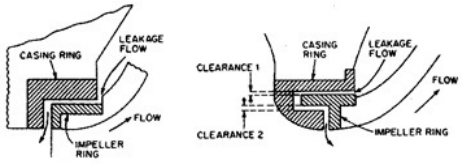

Figure 4.5: Different types of seals: L-shaped at the left side and single labyrinth at the right (adapted from [78]).

If one percent of the total flow leaks from the annular seal, this means that one percent of the flow rate is throttled and transformed into heat. Thus, there is a reduction of one percent in the pump's efficiency. The same reasoning is applied for leakages through axial thrust balance devices (i.e. balance holes or balance piston) once the augmented head pressure on the leakage flow is converted into the suction pressure.

Seal leakages, that lead to efficiency impairment, lose impact with increasing specific speed since the pressure difference over the seal is smaller and leakages are associated with an increasingly larger useful flow rate Q_{sp}/Q. For $\Omega > 1.13$ the leakage flow represents 1% or less of the total flow rate (2% if the impeller's designed include balance holes).

Due to the lack of relevant test data and numerous factors like turbulence, roughness, pressure difference over the seal and many others, the leakage calculations are subject to uncertainties close to $\pm$ 30%.

4.2.2 Leakage losses through inter-stage seals

Apart from the annular seal at the impeller inlet, multistage pumps also include an annular seal that balks the leakages between two adjacent stages, known as the inter-stage seal, Fig. 4.6.

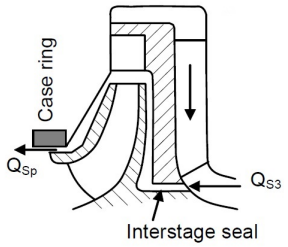

Figure 4.6: Inter-stage seal of a centrifugal pump (adapted from [16]).

At the inter-stage seal, the energy of the leakage flow is equal to the energy of the fluid that was in its gap previously. In addition, as the flow in the axial clearance only receives part of the full blade work, because it does not pass through the impeller, the leakages are not imparted the full blade work. However, at the inlet of the inter-stage seal, these leakages withhold the optimal pressure head. This implies that the amount of dissipated energy through the annular seal is equal to the difference between the optimal head and the partload-channel head.

According to [16], the throttling loss ΔH_{s3} frequently imposed by the seal should be evaluated with only 40% of the optimal head, Eq. 4.4.

$$\frac{\Delta H_{s3}}{H_{st}} = 0.4 \tag{4.4}$$

In addition, [16] also states that the leakage flow through the annular seal Q_{s3} can be estimated through Eq. 4.5 and that, Eq. 4.6 provides a good approximation of the inter-stage seal losses P_{s3}. From this equation, it can also be seen that an increase of the non-dimensional specific speed Ω lead to a reduction of the inter-stage losses.

$$\frac{Q_{S3}}{Q_{opt}} = \frac{0.004347}{\Omega^{1.8}} \tag{4.5}$$

with Q_{opt} representing the flow rate at the BEP.

$$\frac{P_{s3}}{P_{u,st,opt}} = \frac{0.001739}{\Omega^{1.8}} \tag{4.6}$$

with $P_{u,st,opt}$ characterizing the useful power *per stage* (st) for the *operation at maximum (best) efficiency (BEP)* (opt).

4.3 Hydraulic losses

Any friction or vortex dissipation of energy that takes place between the suction and discharge nozzle is defined as a *hydraulic loss*. These losses, that impair the useful head according to Eq. 4.7, can occur in components such as the casing inlet z_E, the impeller z_{La}, the diffuser z_{Le}, the volute z_{sp} and the outlet casing z_A

$$H = \eta_{hyd} \cdot H_{th} = H_{th} - Z_E - Z_{La} - Z_{Le} - Z_{sp} - Z_A \tag{4.7}$$

Skin friction losses are a consequence from the shear stresses created between the fluid and the boundary layer of a body. These losses depend on the Reynolds number Re and the roughness ϵ and,

unlike vortex losses, they have more importance in thin boundary layers and attached flows (i.e. flows with a low separation form the surface).

The thickening of the boundary layers in decelerated flows entails non-uniform velocity distributions. With the increase of momentum exchange between the streamlines, large eddies collapse and form a small-scale turbulent flow. Moreover, fluid particles boost their molecular movement resulting in a slight rise of its temperature. Such losses are known as vortex, turbulent or mixing losses.

4.3.1 Friction losses

The presence of velocity gradients in non-separated boundary layers creates wall shear stresses that result in the dissipation of energy. This loss of energy is known as friction resistance and the shear stresses associated to it are characterized by the friction coefficient c_f.

Usually, the calculation of the friction coefficient is based on a flat plate geometry and can either be achieved from tests, Fig. 4.7 , or boundary layer correlations. In turbulent flow, Eq. 4.8 is most suitable to attain the approximate value of the friction coefficient, whereas in *laminar* (lam) conditions another expression, namely Eq. 4.9, must be applied, [16]. In this equation, the flat plate Reynolds number is directly proportional to the relative velocity of the fluid w.

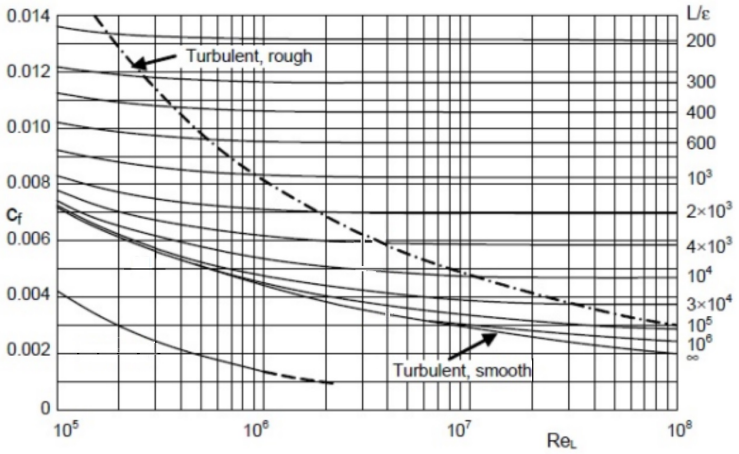

Figure 4.7: Friction coefficient c_f of a flat plate (adapted from [16]).

In the case where $Re_{crit} < 10^5$, the graphic from Fig. 4.7 should be used instead of extrapolating from Eqs. 4.8 and 4.9 to avoid unnecessary errors. The critical Reynolds number Re_{crit} defines the transition between laminar and turbulent flows, Eq. 4.11. It depends on the turbulence intensity of the flow Tu and on the relative roughness of the plate ε/L, with ε representing its roughness. In literature, it can be found several documents exemplifying frequent turbulence levels Tu inside a pump, see for instance [79] and [80].

$$c_{f,turb} = \frac{0.136}{\left\{ -\log\left(0.2 \cdot \frac{\varepsilon}{L} + \frac{12.5}{Re_L}\right)\right\}^{2.15}} \qquad with \quad \begin{cases} 10^5 < Re_L < 10^8 \\ 0 < \varepsilon/L < 10^{-3} \end{cases} \tag{4.8}$$

$$c_{f,lam} = \frac{2.65}{{Re_L}^{0.875}} - \frac{2}{8Re_L + 0,016/Re_L} + \frac{1.328}{\sqrt{Re_L}} \qquad with \qquad 0.01 < Re_L < Re_{crit} \tag{4.9}$$

$$considering \qquad Re_L = \frac{wL}{\nu} \qquad with \qquad L \equiv flat\ plate\ length \tag{4.10}$$

$$and \qquad Re_{crit} = \frac{3 \times 10^6}{1 + 10^4 Tu^{1.7}} \quad for \quad Tu < 0.1 \tag{4.11}$$

Notice that the equations introduced in this sub-chapter represent the total friction coefficient of a flat plate, and not specific points along its surface. These depend on local boundary layers and tend to be 10 to 30% smaller.

Influence of roughness on friction losses

Conversely to what experience might suggest, a roughness increase in a specific flow does not always imply a rise of the flow resistance. It depends on the roughness elements that constitute the surface of the wall. Therefore, friction losses can vary according to different roughness conditions:

- In laminar flow all roughness peaks are located below the laminar sub-layer, resulting in the lowest friction coefficient possible. Additionally, as there is no exchange of momentum between the flow and the wall, it is deduced that the roughness does not affect the resistance and the losses are solely Re-dependent. Whenever this happens, the wall is termed as *hydraulically smooth*.
- When several roughness peaks protrude the laminar sub-layer, but not in a sufficient way to imply a fully developed turbulent flow, the wall is in region of the transition from smooth to turbulent flow. These peaks are the only ones influencing the friction losses, that now depend on both the roughness and Reynolds number.
- Finally, with increasing Reynolds number, the boundary layer thickness and, consequently, the allowable roughness depth drop. If the roughness peaks of the wall are much larger than the laminar sub-layer, the wall is hydraulically rough. Herein, the friction losses depend only on the roughness, meaning, Reynolds number lost its influence.

Figure 4.7, presented above, represents the variation of the friction coefficient c_f with the roughness ε and Reynolds Re parameters.

Table 4.1 depicts the roughness limits applied to a flat plate geometry. Generally, these limits are useful to determine if the improvement of the pump's surface, and thus, a reduction of the losses, is worth the investment and effort. This can be achieved, for instance, by reducing the kinematic viscosity ν of the fluid or by increasing the flow velocity. Both result in lower limits of the wall roughness and thus, better surface finishes. Furthermore, to avoid stalled regions, the surface roughness of a component's inlet should be lower than at its outlet. Finally, the consideration of higher turbulence levels in pumps than in flat plates, implies lower roughness limits than the values presented in Table 4.1.

Hydraulically smooth	Transition from smooth to rough	Hydraulically rough
$\varepsilon < 100\frac{\nu}{w}$	$100\frac{\nu}{w} < \varepsilon < 1000\frac{\nu}{w}$	$\varepsilon > 1000\frac{\nu}{w}$

Table 4.1: Surface roughness limits for a flat plate (adapted from [16]).

As mentioned above, the friction coefficient c_f depends not only on the number of roughness peaks, but on their depth too. In his research, [81] characterized different types of roughness by gluing sand grains on test plate surfaces and measuring their friction coefficient. The variation of the grains' diameter allowed to evaluate the impact of different roughness depths on the flow resistance. These roughness heights are represented by the sand roughness parameter k_s.

Although [81] assumes a uniform wall roughness imposed by the sand grains, in reality, the pumps' technical surfaces (such as ground, cast or machined) are composed by various roughness peaks with different depths. These amorphous roughnesses are defined, for example, by the maximum roughness depth (epsilon max), and described as the "technical roughness" of a surface. Remembering what was explained in the beginning of this chapter, in these technical surfaces the friction coefficient will gradually cross from the laminar to the rough domain.

The calculation of the technical roughness is quite complex since the estimation of the maximum roughness depth ϵ_{max} requires the knowledge of all roughness peaks and troughs. As an alternative, surface tests are frequently conducted to compare the roughness of a specific plate with the roughness of other plates. The value that comes out of the surface test is defined as the arithmetic mean roughness ϵ_a and corresponds to the center line average of the roughness (CLA), see Fig. 4.8.

The resulting roughness is then classified according to a predefined roughness classes[2] stated by N1, N2, N3 etc. Each class is separated by a factor of 2, meaning, if $\varepsilon_{max}(N5) = 2.4$, thus, $\varepsilon_{max}(N6) = 4.8$, and so on.

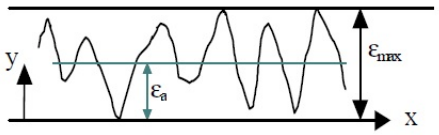

Figure 4.8: Maximum and arithmetic roughness depth (adapted from [16]).

Moreover, the maximum roughness depth ε_{max} is obtained with the arithmetic mean roughness ε_a through Eq. 4.12. The ratio $\varepsilon_{max}/\varepsilon_a$ varies between 5 and 7. In most cases it is assumed as equal to 6.

$$\varepsilon_{max} = (5\ to\ 7) \times \varepsilon_a \tag{4.12}$$

Consider a pipe with a certain roughness depth ε_{max}, whose friction coefficient is represented by λ_r, instead of c_f. If this friction coefficient is calculated from pressure loss analysis, then an equivalent sand roughness ε can be estimated according to Eq. 4.13, with D_h representing the hydraulic diameter of the

[2]For a more detailed description of the corresponding scale, check Table 4.4.

pipe [16]. Furthermore, the ratio between the maximum roughness ε_{max} and the achieved equivalent sand roughness ε results in the equivalence factor c_{eq}, Eq. 4.14.

$$\lambda_R = \frac{0.31}{\left\{ \log\left(0.135\frac{\varepsilon}{D_h} + \frac{6.5}{Re}\right) \right\}^2} \qquad with \qquad D_h \equiv hydraulic\ diameter \tag{4.13}$$

$$c_{eq} \equiv \frac{\varepsilon_{max}}{\varepsilon} \tag{4.14}$$

Literature does not hold much information regarding the equivalence factor c_{eq}. However, Table 4.2 still represents some typical values that this parameter can assume. See [82] for detailed information.

	c_{eq}
Manufacturing marks perpendicular to the flow direction	2.6
Manufacturing marks parallel to the flow direction	5
Drawn metal tubes	2 to 2.6
Smooth coating (e.g. paint)	0.63

Table 4.2: Equivalence factor c_{eq} of several materials (adapted from [16]).

In the case where the equivalent sand roughness cannot be calculated from pressure loss analysis, but ε_{max} and c_{eq} of the surface are known [3], Eq. 4.15 can be applied to determine the equivalent sand roughness ε .

$$\varepsilon = \frac{\varepsilon_{max}}{c_{eq}} \qquad or \qquad \varepsilon = \frac{6\,\varepsilon_a}{c_{eq}} \quad with \quad \varepsilon_{max} = 6\,\varepsilon_a \tag{4.15}$$

Table 4.3 exemplifies some materials with the corresponding equivalent sand roughnesses, ε . Such values result from roughness tests found in literature documents, such as [83], [84] and [85].

	ε (mm)
Glass, coatings, plastic, drawn metal tubes, polished surfaces	0.001 to 0.002
Drawn steel pipes, new	0.02 to 0.1
Drawn steel pipes, lightly rusted	0.15 to 1
Steel pipes, severely rusted or with deposits	1 to 3
Cast iron pipes and pump components	0.3 to 1
Concrete pipes	1 to 3

Table 4.3: Equivalent sand roughness ε of different materials.

Finally, with the estimated equivalent sand roughness, appeal to Eqs. 4.9 / 4.8 or Fig. 4.7 to obtain the flat plate friction coefficient c_f.

Table 4.4 represents the different roughness classes that can be considered when estimating a certain wall roughness. It contains the arithmetic mean roughness ε_a measured from surface tests, the maximum roughness depth ε_{max} obtained from Eq. 4.12 and the equivalent sand roughness ε determined via Eq. 4.15. The displayed values are rounded and, for each class, ε_a is the lower limit of the corresponding class.

It is yet important to acknowledge that the friction coefficient diagrams for technical roughness (Fig. 4.7) differ from the sand roughness diagrams only in the transition zone from smooth to rough flows.

[3] As seen from Eq. 4.15, it is not mandatory to aknowledge the value of ε_{max} as long as ε_a is known.

Roughness classes	Arithmetic average roughness	Maximum roughness	Equivalent sand roughness
	$\varepsilon_a\ (\mu m)$	$\varepsilon_{max}\ (\mu m)$	$\varepsilon\ (\mu m)$
N5	0.4	2.4	1
N6	0.8	4,8	2
N7	1,6	9,6	4
N8	3,2	19	8
N9	6.3	38	16
N10	12.5	75	32
N11	25	150	64
N12	50	300	128
N13	100	600	256

Table 4.4: Roughness classes.

Hence, they have the same resistance coefficients in the hydraulically smooth and rough regions for any value of the relative roughness ε/L .

When calculating the friction coefficient of a wall in turbulent flow, the major concern stands for the level of reliability of the estimated roughness, once a class deviation by a factor of 2 implies an uncertainty of the calculated losses of around 15 to 35%, [16].

Disk friction losses

As mentioned above, the friction coefficient depends on the roughness and Reynolds number. Apart from the friction coefficient defined for a flat plate c_f, in a circular disk (i.e. impeller) losses are also inherently associated with the passage of flow through itself. Therefore, it is necessary to specify a new variable in order to distinguish both friction coefficients. The latter is known as the disk friction coefficient k_{RR} and is expected to be from the same magnitude of the friction coefficient c_f.

The calculation of the disk friction coefficient k_{RR} is based upon correlations that were achieved from experiments with hydraulically smooth disks: Eq. 4.16 is obtained through [86]; Eqs. 4.17 to 4.20 were formulated by [87]; and Eq. 4.21 was experimentally found by [88], with the disk friction coefficient with zero leakages k_o given by Eq. 4.22.

The parameter s_{ax} represents the axial clearance between the rear surface of the impeller and the casing, while r_2 is defined as the impeller radius. Moreover, Eq. 4.22 denotes c_u has the circumferential component of the absolute velocity, t_{ax} as the axial casing part in the impeller sidewall gap and r_w as the casing radius, Fig. 4.9.

The leakages through the impeller sidewall gaps and the roughness effects are considered in hydraulic smooth disk. However, according to [86] and [88], the disk friction coefficient must take into account these aspects. As such, Eqs. 4.16 and 4.21 are both multiplied by a roughness and leakage correction factor, f_R and f_L, respectively.

$\underline{1^{st}\ Experiment\ :}$

$$k_{RR} = \frac{\pi r_2}{2Re \cdot s_{ax}} + \frac{0.02}{Re^{0.2}} \cdot \frac{1 + \frac{s_{ax}}{r_2}}{1 + \frac{s_{ax}}{2r_2}} \cdot f_L f_{R,La} \tag{4.16}$$

2^{nd} *Experiment* :

$$k_{RR} = \frac{\pi r_2}{2Re \cdot s_{ax}} \qquad for \quad Re_{lam} \leq 8.7 \left(\frac{s_{ax}}{r_2}\right)^{-1.87} \tag{4.17}$$

$$k_{RR} = \frac{0.925}{Re^{0.25}} \cdot \left(\frac{r_2}{s_{ax}}\right)^{1/6} \qquad for \quad Re_{lam} < Re < 2 \times 10^5 \tag{4.18}$$

$$k_{RR} = \frac{0.02}{Re^{0.25}} \cdot \left(\frac{r_2}{s_{ax}}\right)^{1/6} \qquad for \quad 10^5 < Re < 10^6 \tag{4.19}$$

$$k_{RR} = \frac{0.0255}{Re^{0.2}} \cdot \left(\frac{s_{ax}}{r_2}\right)^{0.1} \qquad for \quad Re > 2 \times 10^5 \tag{4.20}$$

3^{rd} *Experiment* :

$$k_{RR} = \frac{\pi r_2}{2Re \cdot s_{ax}} + \frac{0.0625}{Re^{0.2}} \cdot (1 - k_o)^{1.75} \cdot f_{R,La} \cdot f_L \qquad valid\ for \qquad Re > 10 \tag{4.21}$$

$$and\ with \quad k_o = \frac{c_u}{\omega r_2} = \frac{1}{1 + \left(\frac{r_\omega}{r_2}\right)^2 \cdot \sqrt{\left(\frac{r_\omega}{r_2} + 5\frac{t_{ax}}{r_2}\right) \cdot \frac{f_{R,A}}{f_{R,La}}}} \quad , \quad r_\omega = r_2 \quad , \quad t_{ax} = 0 \tag{4.22}$$

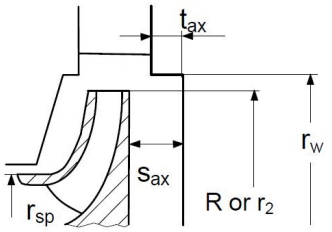

Figure 4.9: Part of the transverse section of the impeller of a centrifugal pump (adapted from [16]).

The roughness correction factor f_R is assessed by the ratio between the friction coefficients of hydraulically rough and smooth disks, meaning, $f_R = k_{RR}(\varepsilon_{rough})/k_{RR}(\varepsilon = 0)$, as represented by Eq. 4.23, [16].

$$f_{R,La} \equiv \frac{k_{RR}(\varepsilon_{rough})}{k_{RR}(\varepsilon = 0)} = \left\{ \frac{\log \frac{12.5}{Re}}{\log\left(0.2\frac{\varepsilon}{r_2} + \frac{12.5}{Re}\right)} \right\}^{2.15} \tag{4.23}$$

As for the case of the leakage flow correction factor f_L, its evaluation is determined on the basis of Eq. 4.24. Herein, the factor φ_{sp} estimates the leakage flow through the sidewall gap, r_{2sp} represents the radius of the impeller inlet annular seal and j as the characteristic parameter of the correction of the flow, being dependent on the direction of the flow, Fig. 4.9. In addition, it should be noted that the leakage effect can vary significantly depending on the direction of the flow inside the seal's clearance (radially inwards or outwards): not only the power of the exponential parameter changes, as the dependent variable a assumes different values.

$$f_L = \exp\left\{-350\ \varphi_{sp}\left(\left[\frac{r_2}{r_{2sp}}\right]^j - 1\right)\right\} \tag{4.24}$$

$$with \quad \begin{cases} \varphi_{sp} > 0 \; and \; j = 1.0 \quad for \quad radially \; inwards \; flow \\ \varphi_{sp} < 0 \; and \; j = 0.75 \quad for \quad radially \; outwards \; flow \end{cases}$$

Despite the variety of correlations presented above (i.e. the 1st, the 2nd and the 3rd experimental correlations), there are some drawbacks and advantages that should be noticed prior to the determination of the disk friction coefficient:

- Conversely to what is verified with in the 2nd experiment, Eq.4.16 covers the entire region from laminar to turbulent flow. Hence, not only it is more practical, but also implies a smaller error near the transition points of the different regimes, meaning, lower unsteadinesses.
- From several tests it is well-known that the axial casing clearance s_{ax} does not have a significant impact on the disk friction coefficient k_{RR} for turbulent flows. However, when the axial casing clearance converges to zero or infinity, the yielded flow resistance according to Eq. 4.20 tends to small and large coefficients, respectively. Therefore, this equation overestimates the disk friction coefficient in rough regimes. Regarding Eq.4.16, the resulting effect is the opposite: not only does the correlation obtain more sensible values, but also endures extreme axial clearances s_{ax} .
- Besides these methodologies, Eq.4.21 is also used to evaluate the disk friction coefficient k_{RR}. It considers the rotation of the fluid inside the impeller sidewall gap by analyzing the influence of the gap's geometry and the roughness of the impeller shrouds and casing. Despite being more useful when the casing and impeller have different roughnesses, this methodology developed by [88] ends-up being unpractical whenever the gap's geometry is not known, which can happen frequently.

Figure 4.10 illustrates the existing similarities between the different correlations [4] that can be applied to estimate k_{RR}. From this figure, it is concluded that both Eq. 4.16 and Eq. 4.21 provide similar resistance coefficients and represent reasonably Eqs. 4.17 to 4.20.

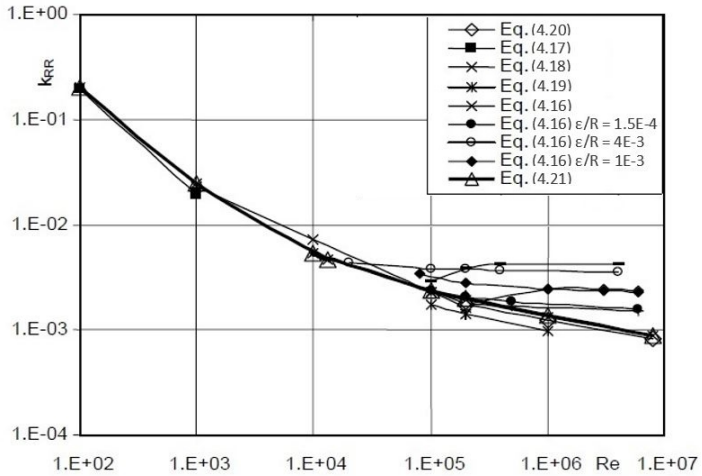

Figure 4.10: Disk friction coefficient k_{RR} variation as a function of the Reynolds number and the experimental procedure, meaning, 1st, 2nd or 3rd experiments, (adapted from [16]).

[4] Mind that Fig. 4.10 also represents some correlations beyond the three experiments referred above.

According to [16], the fraction of the useful power P_u to whom corresponds the disk friction losses P_{RR} is calculated according to Eq. 4.25, used for any flow conditions.

$$\frac{P_{RR}}{P_u} = \frac{8\sqrt{2} \cdot k_{RR,M} \cdot f_{geo}}{\omega_s^2 \cdot \Psi_{opt}^{2.5} \cdot f_q} = \frac{11.321 \cdot k_{RR,M} \cdot f_{geo}}{\Omega^2 \cdot \Psi_{opt}^{2.5} \cdot f_q} \tag{4.25}$$

In this equation, $\omega_s = 2\pi\ N/60$ represent the specific speed of the pump in rads/s, with N characterizing the rotational speed in rpm. The geometrical factor f_{geo} represents the corrections that must be considered since the impeller geometry varies from pump to pump. For typical radial impellers, $f_{geo} = 1.22$. In addition, f_q is acknowledge as the number of impeller eyes per impeller: single-entry implies $f_q = 1$, whilst double-entry entails $f_q = 2$. The head coefficient Ψ at the BEP is given by Eq. 4.26, with the transport velocity $U = \omega \cdot r$ representing the tangential velocity at the tip of the blades.

$$\Psi_{opt} = \frac{2gH}{U_2^2} \tag{4.26}$$

Alike disk friction coefficients, these losses depend on a variety of factors, such as: the roughness difference between the impeller shrouds and the casing, that affects the rotational velocity of the fluid inside the gap; the axial casing clearance that, in spite of being irrelevant in turbulent flows, matters in laminar flow conditions; and the leakages through the impeller sidewall gap, that can be large enough to decrease the pump's performance significantly. From the numerous factors that impair the disk, these three have the highest influence on the estimation of the disk friction losses, leading to uncertainties of around 25%, even for the best efficiency point (BEP).

4.3.2 Mixing losses

Besides being essentially non-uniform, the velocity distribution in real flows is more susceptible to high turbulence levels when the flow is decelerating. This explains why the conversion of energy from static pressure to kinetic energy is associated with small losses (accelerated flow), whilst the inverse process is inherent to large losses (decelerated flow).

As explained in the beginning of chapter 4.3, mixing or form losses are caused by turbulent dissipation that occurs when the streamlines exchange momentum between themselves. This process, stimulated by non-uniform flow distributions, can be achieved through several mechanisms:

- Fluid circulation through the blades that creates zones of decelerated flow or even separation (stalled zones). From this process, it may result cavitation of the fluid.
- Recirculation factors, such as adding the leakage flow that comes from the annular seal with the inlet flow rate. This results in non-uniform velocity distributions near the impeller front shroud.

In this way, it is natural to conclude that for a PAT, where the fluid is not intended to flow in a reversible direction, the presence of non-uniform flow distributions might occur with a greater frequency and thus, generate higher mixing losses.

Mixing losses are known for constituting a major part of the total losses, particularly for high specific speeds Ω. These losses are Re-independent and, due to the diverse flow paths of the fluid, they cannot be estimated theoretically: they are predicted through numerical methods or empirical correlations (check for example [84], [83] and [89]).

Chapter 5

New methodology for PAT efficiency scaling

Along this chapter it will be described the methodology used to calculate the efficiency and characteristics of operation[1] of a centrifugal pump working as a turbine (PAT) taking as reference the efficiency and characteristics of a geometrically similar pump (i.e. with the same dimensionless specific speed, Ω). The pump, whose characteristics need to be determined, is defined as the *prototype* (p), whilst the reference pump is known as the *model* (M).

Part of the numerical model used in this work is pointed towards efficiency scaling between two geometrically similar centrifugal pumps given by [16]. Nevertheless, the same theory is going to be applied for pumps working as turbines in order to evaluate the possibility of this alternative methodology of scaling efficiencies for geometrically similar turbomachinery.

The implementation of such procedure provides an understanding of the impact that the Reynolds number, roughness and specific speed have on the different types of losses and, subsequently, on the efficiency of a PAT. Additionally, this method can also be used in any type of flow conditions (even at transitory regime) and surface roughnesses, still providing stable results.

In the first section it is expressed both the model and resembling prototype operating characteristics required to apply the numerical methodology. Subsequently, it is explained how to calculated the distinct correction factor that allow the estimation of the flow rate and head prototype efficiency curves. This methodology is based on several corrections applied to different parameters such the efficiency, the specific speed and the PAT diameter. Throughout this chapter, it will be seen how to apply a proper correction of these parameters.

[1] Recall some of the operating characteristics presented in chapter 3 such as the flow rate, the head, the power and the rotational speed.

5.1 Model and prototype characterization

Hydroelectric projects are one of the many cases where efficiency scaling is applied. Herein, the real site flow conditions and the planned infrastructure (prototype) are reproduced in a small scale with the best possible precision (model) and tested in a laboratory to understand and evaluate the real project prior to its implementation. For that, it is mandatory to know several model and prototype characteristics.

Analogously to hydropower designs, in the specific numerical method some model and prototype characteristics must be obtained, such as the ones presented in Table 5.1.

Model, M		Prototype, p	
N_M	Rotational speed	N_p	Rotational speed
Q_M	Flow rate at the BEP	P_p	Total power
H_M	Head at the BEP	ν_p	Kinematic viscosity
D_M	Outlet impeller diameter	ε_p	Roughness of different components
η_M	Efficiency at the BEP		
ν_M	Kinematic viscosity		
ε_M	Roughness of different components		

Table 5.1: Required model and prototype characteristic for the application of the numerical model.

In a work published by [90], it is provided a list of 57 PATs with several points of operation. Other characteristics of theses pumps such as the impeller outlet diameter D_2, can be found in most cases as well. This information was not only collected from an extensive variety of sources in literature, but from unpublished sources as well. However, there are still several cases where its accuracy or origin is unknown, [90].

Moreover, [21] also estimated the BEPs for each pump operating in turbine mode by fitting polynomial regressions to the accessible data previously mentioned. Appendix A.3 displays the information relative to the PATs that were only used in this work.

From the 57-PAT list indicated in [90], two geometrically resembling pumps are selected based on the dimensionless specific speed Ω. One of them represents the *model*, while the other describes the *resembling prototype* (rp)[2]. This resembling prototype not only is considered as the reference to evaluate the dispersion of the estimated values, such as efficiency and diameter, but also as the element required to determine the prototype's initial characteristics.

Figure 5.1 represents the considered scheme of this numerical model. The main objective is to obtain the operating characteristics of a particular PAT, denoted as resembling prototype (yellow pump). By relying on a geometrically resembling PAT (i.e. model, small-size pink PAT), it is possible to predict the operating characteristics of a third PAT (known as prototype, normal-size pink PAT) with the same power and rotational speed (could be any two operating parameters) as the resembling prototype, Eqs.

[2]Understand that the prototype and the resembling prototype are two distinct elements. The first is geometrically similar to the model and illustrates how it would behave as a pump with the scaled conditions of the model. The second, represents the characteristics of a PAT more or less similar to the prototype and is used in this work to assess the precision of the estimated values operating as a turbine.

5.1 and 5.2.

$$N_{p,i} = N_{rp} \tag{5.1}$$

$$P_{p,i} = P_{rp} \tag{5.2}$$

Knowing that a family of geometrically similar pumps have the same non-dimensional parameters and that the prototype and the resembling prototype have very close specific speeds, it is acceptable to assume as a first approximation that these two turbomachines have the same efficiency curves[3]. Later in this work, it will be seen that this initial assumption might be invalid.

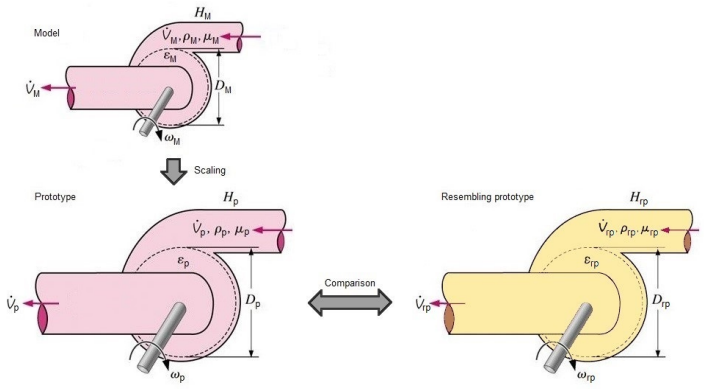

Figure 5.1: Scheme of the numerical method: efficiency scaling from the model to the prototype. The latter provides a prediction of the resembling prototype efficiency curves (adapted from [91]).

Opposing the rotational speed N_{rp} provided along with the respective PAT data, the total power P_{rp} oughts to be estimated via Eq. 5.3.

$$P_{rp,opt} = \rho \; g \; Q_{rp,opt} \; H_{rp,opt} \tag{5.3}$$

With both the power and rotational speed of the prototype, the remaining characteristics are calculated by means of the model characteristics and the affinity laws described in chapter 3: the impeller diameter $D_{2p,i}$ is determined through Eq. 3.14; subsequently, the head $H_{p,i}$ and flow rate $Q_{p,i}$ are estimated by Eqs. 3.12 and 3.11, respectively. The affinity laws also state that the efficiency of the model is equal to the efficiency of the prototype, therefore, $\eta_{M,i} = \eta_{p,i}$, Eq. 3.13.

The prototype characteristics achieved with the affinity laws are labeled with a subscript that represents the *initial estimated values prior to any iteration* (i). In the next chapters it will be seen that these values need to be corrected and thus, distinguished from the values stemming from other iterations.

5.2 Correction of the prototype characteristic point

The presence of the Reynolds number and roughness on a pump is frequently neglected. However, it can be of significant influence. This chapter explains how to consider these effects on the calculation

[3]Recall from chapter 3 that the efficiency is a non-dimensional parameter. Therefore is approximately equal for a family of geometrically similar pumps

of the PAT's performance.

5.2.1 Introduction to roughness and Re influence on the PAT performance

Accounting with all power losses described in chapter 4, the power consumption of the PAT and its respective efficiency can be determined by means of Eq. 5.4 and Eq. 5.5, respectively, with z_{st} equal to the pump number of stages.

$$P_a = \frac{\rho g H_{st} z_{st}\, Q}{\eta_{vol}\ \eta_{hyd}} + P_{RR} + P_{mec} \qquad with \qquad H = H_{st} \cdot z_{st} \tag{5.4}$$

$$\eta = \frac{P_u}{P_a} = \frac{\rho g H z_{st}\, Q}{P_a} \tag{5.5}$$

Herein, the disk friction losses P_{RR} are calculated separately from the remaining hydraulic losses, even though they arise from friction losses in the hub. Thus, are considered hydraulic losses by definition. Besides the disk friction losses, no other losses are considered separately from the group to which they belong.

If equations Eq. 5.4 and Eq. 5.5 are joined together, the total efficiency results in the expression enunciated by Eq. 5.6.

$$\eta = \frac{\eta_{vol}\eta_{hyd}}{1 + \eta_{vol}\eta_{hyd}\left(\dfrac{P_{RR}}{P_u} + \dfrac{P_{mec}}{P_u}\right)} \tag{5.6}$$

Apart from the specific mechanical losses P_{mec}/P_u, which are assumed to be constant both for the model and prototype, the remaining losses are Reynolds and roughness dependent.

The factors obtained from Eqs. 5.7, 5.8 and 5.9, are used to correct the characteristics of the prototype that were once estimated through the affinity laws. These correction factors represent the influence that the Reynolds number and roughness have on the PAT characteristics.

$$f_\eta = \frac{\eta_p}{\eta_M} \qquad f_{\eta hyd} = \frac{\eta_{hyd,p}}{\eta_{hyd,M}} \qquad f_{\eta vol} = \frac{\eta_{vol,p}}{\eta_{vol,M}} \qquad f_{\eta mec} = \frac{\eta_{mec,p}}{\eta_{mec,M}} \tag{5.7}$$

$$f_Q = \frac{\varphi_p}{\varphi_M} \qquad or \qquad f_Q = \frac{Q_p}{Q_M} \tag{5.8}$$

$$f_H = \frac{\Psi_p}{\Psi_M} \qquad or \qquad f_H = \frac{H_p}{H_M} \tag{5.9}$$

Once these factors only take into account the deviations from the model laws, any supplementary calculations of the rotational speed N and/or impeller diameter D_2 must be performed before applying this corrective model, [16].

After doing some equation handling[4], the total efficiency correction factor f_η expressed by Eq. 5.7

[4]Although indispensable, the numerical procedure required to achieve Eq. 5.10 will not be addressed in this work. For detailed information, see [16].

can also be written as

$$f_\eta = \frac{\eta_p}{\eta_M} = \frac{f_{\eta_{hyd}} \cdot f_{\eta_{vol}} \left[1 + \left\{ \left(\frac{P_{RR}}{P_u} \right)_M + \left(\frac{P_m}{P_u} \right)_M \right\} \eta_{vol,M} \cdot \eta_{hyd,M} \right]}{1 + \left\{ \left(\frac{P_{RR}}{P_u} \right)_M \cdot \frac{k_{RR,p}}{k_{RR,M}} + \left(\frac{P_{mec}}{P_u} \right)_M \frac{\rho_M f_{\eta mec}}{\rho_p} \right\} \frac{f_{\eta hyd} \cdot f_{\eta vol}}{f_H f_Q} \eta_{vol,M} \cdot \eta_{hyd,M}} \tag{5.10}$$

Despite the evident complexity associated with Eq. 5.10, several assumptions can be considered to convert it into a more practical and accessible formula, such as Eq. 5.11:

- Since identical fluids are expected to flow through the model and prototype, their densities are deemed as equal, $\rho_M = \rho_p$.
- As mentioned previously, once the specific mechanical losses P_{mec}/P_u do not vary from the model to the prototype, the mechanical factor can be assumed as equal to one, $f\eta_{mec} = 1$.
- In the case where the geometry of the annular seal is known, the factor that corrects the volumetric efficiency $f\eta_{vol}$ can be determined according to [16]. Otherwise, it is reasonable to assume $f_{\eta vol} \simeq 1$.
- In his book,[16] only specifies the estimation of the flow rate correction factor f_Q for highly viscous fluids (this is, $\nu \simeq 10^{-4}\ m^2/s$) . Therefore, it is stipulated, as a first approximation, that the flow rate of the prototype is simply obtained according to the affinity laws and is not affected by the roughness or Reynolds number, meaning, $f_Q = 1$.
- Lastly, the head correction factor f_H is matched to the hydraulic efficiency factor $f_{\eta hyd}$, i.e. $f_H = f_{\eta hyd}$, considering that the specific work of the blades Y_{th} remains constant. This assumption is required once the head is affected by several factors that cannot be quantified from tests, such as: changes in Reynolds number that end-up modifying the amount of flow that circulates through the impeller and, consequently, shifts the Q-H curve; variations of the roughness inside the impeller's passages that cause head increments; and increases of flow momentum near the walls of the impeller shrouds since the circumferential flow velocity in their boundary layers is around the transport velocity U . Apart from these factors, Eq. 5.20, that will be later analyzed, also explains why the head factor f_H can be correlated with the hydraulic efficiency factor $f_{\eta hyd}$.

With these assumptions, it is possible to estimate the efficiency factor according to Eq. 5.11, [16].

$$f_\eta = \frac{f_{\eta_{hyd}} \left[1 + \left\{ \left(\frac{P_{RR}}{P_u} \right)_M + \left(\frac{P_m}{P_u} \right)_M \right\} \eta_{vol,M} \cdot \eta_{hyd,M} \right]}{1 + \left\{ \left(\frac{P_{RR}}{P_u} \right)_M \cdot \frac{k_{RR,p}}{k_{RR,M}} + \left(\frac{P_{mec}}{P_u} \right)_M \right\} \frac{\eta_{vol,M} \cdot \eta_{hyd,M}}{f_Q}} \tag{5.11}$$

The *Similarity Laws* (SL) defined by Eqs. 3.11, 3.12 and 3.14, along with the *Correction Factors* (CF) from Eqs. 5.8, 5.9 and 5.11, express the corrected characteristics of the PAT that take into account a *Roughness and Reynolds number Correction* (RRC), Eqs. 5.12, 5.13 and 5.14. Notice that [16] in his

methodology corrects the similarity laws presented in chapter 3 by introducing the density and number of stages ratios in Eqs. 3.12 and 3.14.

$$\left(\frac{Q_p}{Q_M}\right)_{RRC} = \left(\frac{Q_p}{Q_M}\right)_{SL} \cdot \left(\frac{Q_p}{Q_M}\right)_{CF} = \frac{N_p}{N_M}\left(\frac{D_{2p}}{D_{2M}}\right)^3 \cdot f_Q \tag{5.12}$$

$$\left(\frac{H_p}{H_M}\right)_{RRC} = \left(\frac{H_p}{H_M}\right)_{SL} \cdot \left(\frac{H_p}{H_M}\right)_{CF} = \left(\frac{N_p}{N_M}\right)^2\left(\frac{D_{2p}}{D_{2M}}\right)^2 \frac{z_{st,p}}{z_{st,M}} \cdot f_H \tag{5.13}$$

$$\left(\frac{P_p}{P_M}\right)_{RRC} = \left(\frac{P_p}{P_M}\right)_{SL} \cdot \left(\frac{P_p}{P_M}\right)_{CF} = \left(\frac{N_p}{N_M}\right)^3\left(\frac{D_{2p}}{D_{2M}}\right)^5 \frac{\rho_p}{\rho_M}\frac{z_{st,p}}{z_{st,M}} \cdot f_\eta \tag{5.14}$$

5.2.2 Correction of the PAT performance

Through the analysis of Eq. 5.11 it is noticeable that each term of the efficiency factor expression f_η describes a specific loss affecting the PAT. In the end, this correction factor will represent the total influence that the Reynolds number and roughness have on the PAT's efficiency.

Volumetric losses

As explained previously, the volumetric losses consist of leakages through several components of the pump that result in kinetic energy losses and, consequently, head and efficiency reductions. The impact of these leakages on the PAT is evaluated by means of Eq. 5.15, which expresses the volumetric efficiency η_{vol}.

$$\eta_{vol} = \frac{Q}{Q + Q_{sp} + Q_E + Q_{s3}\dfrac{\Delta H_{s3}(z_{st}-1)}{H_{st}z_{st}}} \tag{5.15}$$

This equation represents the fraction of the total flow rate that circulates through the PAT without leaking through the impeller annular seal Q_{sp}, the axial thrust balance device Q_E and/or the inter-stage annular seal Q_{s3}, in case of multistage PATs.

The parameters Q_{sp} and Q_{s3} are estimated through Eqs. 4.2 and 4.5 respectively, while Q_E is assumed as equal to Q_{sp}. Moreover, for the valuation of Q_{s3}, it is considered that $H_{s3}/H_{st} = 0.4$ is a reasonable supposition once the flow in the axial clearance only receives part of the full blade work, recall chapter 4.

Mechanical losses

Fortunately, mechanical losses do not entail a complex set of equations or considerations. If no information is provided by the pump manufacturer, the model mechanical losses P_{mec}/P_u can be computed by Eq. 4.1 for its BEP. If in one hand, these losses can reach extremely high values of efficiency for large size pumps, on the other (i.e. small pumps.), they can represent a significant amount of the useful power P_u .

Disk friction losses

The disk friction losses belong to the type of hydraulic losses created through the interaction between the fluid and the surface boundary layers of the pump. These losses are expressed by Eq. 4.25 and involve a considerable number of suppositions and calculations.

The friction coefficient k_{RR} associated with Eq. 4.25 can be achieve through different approaches. However, since an essential part of the PAT geometry is not available and the second experiment overestimates the friction coefficient for turbulent flows, this parameter is determined based on the Eq. 4.21. It depends on the axial clearance of the sidewall gap s_{ax}, the Reynolds number Re, the leakage flow correction factor f_L and the roughness factor f_R .

According to the guidelines provided by [16] to design the impeller sidewall gap, the axial clearance to radius ratio s_{ax}/r should vary between 0.03 and 0.08. In this thesis, the average value of this range was considered, meaning, $s_{ax}/r = 0.55$. Such value is assumed as constant for both the model and prototype.

As mentioned in chapter 4.3.1, upon the characterization of the friction coefficient c_f, the Reynolds number is given by wL/ν , with L representing the length of a flat plate. However, to simplify its computation in the impeller shrouds and hydraulic channels, the parameter L is replaced by the outlet radius of the impeller r_2.

Afterwards, the technical roughness ε of the impeller is stipulated so that the roughness factor f_R can be estimated via Eq. 4.23. In Table 4.3, it was illustrated the roughness of several types of materials that may be used in a pump system. In this work, the *drawn steel pipes, new* example was thought to represent the material that better describes the impeller. Since this specification ranges from 0.02 to 0.1 mm, the equivalent sand roughness ε is averaged to a value of 0.06 mm, or 60 μm. Alternatively to this approach, the technical roughness can also be drawn from the literature. For instance, [92] assumes an equivalent sand roughness of 100 μm.

The leakage flow factor f_L is established according to Eq. 4.24. Herein, the leakage flow circulating through the sidewall gap is represented by the leakage flow coefficient φ_{sp} , with the transport velocity given by $U = \omega \cdot r_2$ in m/s, notice Eq. 5.16.

$$\varphi_{sp} = \frac{Q_{sp}}{\pi \, r_2^2 \, U} \tag{5.16}$$

Back to Eq. 4.25, the head coefficient Ψ_{opt} of the PAT at its BEP still remains unknown. To predict its value, the following equation is applied:

$$\Psi_{opt} = \frac{2gH}{U^2} \tag{5.17}$$

Lastly, and specifically for the disk friction losses, the described calculation procedure must be applied for both the model and prototype as represented in the efficiency factor equation f_η . The calculation of the prototype disk friction losses implies that part of the volumetric loss procedure must be assigned for the prototype as well. This is necessary since the leakage flow rate Q_{sp} is essential for the prediction of the leakage flow coefficient φ_{sp} .

Hydraulic losses

The hydraulic losses in a PAT are described by the friction and mixing losses, $\zeta_F = f(Re, \varepsilon)$ and ζ_M, respectively (recall chapter 4.3). These losses can be assessed by solving Eq. 5.6 with respect to the hydraulic efficiency η_{hyd}, see Eq. 5.18 below.

$$\eta_{hyd,M} = \frac{\eta}{\eta_{vol}\left\{1 - \eta\left[\left(\frac{P_{RR}}{P_u}\right)_M + \frac{P_{mec}}{P_u}\right]\right\}} \tag{5.18}$$

Moreover, in the case where the theoretical head coefficients of the model and prototype are considered to be equals, it results in the following

$$\Psi_{th} = \Psi_M + \zeta_{F,M} + \zeta_{M,M} = \Psi_p + \zeta_{F,p} + \zeta_{M,p} \tag{5.19}$$

If the specific blade work Y_{th} of a pump is inferred as constant, then the head correction factor f_H must be similar to the factor $f\eta_{hyd}$, just like justified in Eq. 5.20.

$$f_{\eta,hyd} = \frac{\eta_{hyd,p}}{\eta_{hyd,M}} = \frac{\frac{Y_p}{Y_{th,p}}}{\frac{Y_M}{Y_{th,M}}} = \frac{Y_p}{Y_M} = \frac{gH_p}{gH_M} = \frac{H_p}{H_M} = f_H \qquad with \qquad Y_{th,p} = Y_{th,M} \tag{5.20}$$

Joining Eqs. 5.19 and 5.20 and assuming that the mixing losses depend neither on the Reynolds number nor on the roughness (i.e. $\zeta_{M,M} = \zeta_{M,p}$), then the hydraulic efficiency factor is defined by means of Eq. 5.21.

$$f_{\eta hyd} = \frac{\eta_{hyd,p}}{\eta_{hyd,M}} = 1 - \frac{\zeta_{F,M}}{\Psi_M}\left(\frac{\zeta_{F,p}}{\zeta_{F,M}} - 1\right) \tag{5.21}$$

with $\zeta_{F,M}/\Psi_M$ representing the amount of friction losses that inherent to the fluid's head Ψ_M . This ratio, which depends on the dimensional specific speed, the pump type and the geometry of hydraulic components, is determined by Eq. 5.22. Its coefficients, a_1 and b_1 , are the product of a series of experimental tests performed by [93] for centrifugal pumps.

$$\zeta_{F,M}/\Psi_{M,opt} = \left\{\frac{1}{\eta_{hyd,M}} - 1\right\}\left(a_1 - b_1\Omega\sqrt{f_q}\right) \qquad with \qquad \begin{cases} a_1 = 0.635 \\ b_1 = 0.08464 \end{cases} \tag{5.22}$$

In addition, to avoid complex calculations associated with the friction losses in the model and prototype, a proportional relationship between the factor $\zeta_{F,p}/\zeta_{F,M}$ and the respective friction coefficients c_f is assumed. Consequently, Eq. 5.21 can be equivalently written as Eq. 5.23.

$$f_{\eta hyd} = 1 - \frac{\zeta_{F,M}}{\Psi_M}\left(\frac{c_{f,p}}{c_{f,M}} - 1\right) \tag{5.23}$$

Finally, to obtain the hydraulic correction factor, the friction coefficients of the model and prototype have to be predicted via Eqs. 4.8 and 4.9, depending on the flow conditions verified inside the PAT.

The evaluation of these coefficients is based on the average roughness $\varepsilon_{av,h}$ of the hydraulic channels, as expressed by Eq. 5.24. In his work, [93] provides a correlation that allows the determination of this parameter based on the impeller roughness ε_{La} , diffuser roughness ε_{Le} and roughness weighting factor a_ε , Eq. 5.24.

In this work, the impeller roughness is 10% lower than the diffuser roughness since the abrasion in the impeller is assumed to be higher than in the diffuser, due to greater cavitation occurrences near the blades.

$$\varepsilon_{av,h} = (1 - a_\varepsilon)\varepsilon_{La} + a_\varepsilon \cdot \varepsilon_{Le} \qquad with \qquad \varepsilon_{La} = 0.9\,\varepsilon_{Le} \tag{5.24}$$

As seen previously, the range of each flow condition is defined by the critical Reynolds number Re_{crit} . To attain this parameter, it is required to characterize the turbulence intensity Tu inside the PAT. According to [79], the turbulence level experienced in a centrifugal pump varies between 7-8%. Assuming the range average value, it comes that $Tu = 7.5\%$.

Performance correction factors and characteristics

With each particular loss identified, the efficiency correction factor can be determined via Eq. 5.11. As a consequence, the performance correction factors that represent the influence of the roughness and Reynolds number are finally characterized:

$$f_{Q,RRC} = 1 \qquad initial\ assumption \tag{5.25}$$

$$f_{H,RRC} = f_{\eta hyd} \qquad from\ equation\ 5.23 \tag{5.26}$$

$$f_{\eta,RRC} = \frac{\eta_p}{\eta_M} \qquad from\ equation\ 5.11 \tag{5.27}$$

These factors from Eqs. 5.25, 5.26 and 5.27, when multiplied by the PAT corresponding characteristics, result in the new performance values that take into account the roughness and Reynolds number variants for a scaled version of the model, Eqs. 5.28, 5.29 and 5.30.

$$Q_{p,RRC} = Q_{p,i} \cdot f_{Q,RRC} \tag{5.28}$$

$$H_{p,RRC} = H_{p,i} \cdot f_{H,RRC} \tag{5.29}$$

$$\eta_{p,RRC} = \eta_{p,i} \cdot f_{\eta,RRC} \tag{5.30}$$

5.2.3 Correction of the PAT specific speed

One of the initial considerations stipulated upon the implementation of this methodology states the following: the model and prototype are undoubtedly geometrically similar. Recalling geometrical similarity, two pumps with similar geometry have the same dimensionless characteristics and so, the same specific speed Ω. Therefore, the specific speed of the prototype must be equal to the specific speed of the model, meaning, $\Omega_p = \Omega_M$.

However, the new characteristic values of the PAT comprehend an error associated with the dimensionless specific speed Ω : this parameter, when estimated with the new characteristics of the PAT,

differs from the specific speed of the model. Such result leads to the conclusion that some assumption is misleading the calculation of the performance correction factors.

The specific speed depends on the rotational speed N, on the useful head H and on the flow rate Q. From these parameters, the only assumption that was not based on any literary sources corresponds to the condition imposed to the flow rate correction factor, $f_Q = 1$. As explained above, this condition results from the lack of information provided by [16] on the calculation of this parameter and states that the roughness and Reynolds number have no significant influence on the flow rate of the PAT. However, it is now perceived that this influence must be considered, otherwise, the geometric similarity condition will not be respected.

To estimate the actual impact that the Reynolds number and roughness have on the flow rate, the condition[5] regarding the specific speed similarity is applied, Eq. 5.31.

$$\Omega_M = \Omega_p \quad \Leftrightarrow \quad \Omega_M = w_p \cdot \frac{\sqrt{\frac{Q_{p,i}}{f_q}}}{\left(gH_{p,i}\right)^{3/4}} \qquad with \qquad Q_{p,i} = Q_{AL} \cdot f_Q \tag{5.31}$$

Herein, Q_{AL} represents the flow rate calculated from the affinity laws' equations and $H_{p,i}$ the prototype useful head obtained by applying the numerical procedure described in chapter 5.2.2 (i.e. already after the head correction factor f_H has been applied to the head).

By solving Eq. 5.31 with respect to flow rate correction factor f_Q, the following equation is obtained.

$$f_Q = \left(\frac{\Omega_M \cdot \left(gH_{p,i}\right)^{3/4}}{w_p} \right)^2 \frac{f_q}{Q_{AL}} \tag{5.32}$$

With f_Q, the flow rate adjusted according to the specific speed similarity condition "SSC" is given by means of Eq. 5.33.

$$Q_{p,SSC} = Q_{p,i} \cdot f_{Q,SSC} \tag{5.33}$$

Notice that, even though the head factor remains constant with the correction of the specific speed (i.e. $f_{H,RRC} = f_{H,SSC}$), the same is not verified with the efficiency correction factor f_η. This parameter varies with f_Q according to Eq. 5.11 and shall be determined with the exact same losses measured for $f_Q = 1$.

In conclusion, the PAT characteristics adjusted to the corrected specific speed are given by Eqs. 5.34, 5.35 and 5.36.

$$Q_{p,SSC} = Q_{p,i} \cdot f_{Q,SSC} \tag{5.34}$$

$$H_{p,SSC} = H_{p,i} \cdot f_{H,SSC} \tag{5.35}$$

$$\eta_{p,SSC} = \eta_{p,i} \cdot f_{\eta,SSC} \tag{5.36}$$

[5] In Eq. 5.31, do not mistake f_Q with f_q. The first corresponds to the flow rate correction factor, while the second represents the number of PAT inlets (which is equal to 1 or 2).

5.2.4 Correction of the PAT diameter

Recall the power equation characterized by the affinity laws along with the roughness and Reynolds number influence, Eq 5.14.

$$P_p = P_M \left(\frac{N_p}{N_M}\right)^3 \left(\frac{D_{2p}}{D_{2M}}\right)^5 \frac{\rho_p}{\rho_M} \frac{z_{st,p}}{z_{st,M}} \cdot f_\eta$$

The presence of the efficiency correction factor in this equation states that one of its terms must change in order to maintain the protoype's power.

At the beginning of this numerical methodology, the power and rotational speed of the prototype were defined as constraint variables, meaning, the result of the calculations that follow them depends on the values that these parameters assume. They cannot be modified in the process as they are considered as certain. In addition, any parameter that characterizes the model cannot vary as well, because this turbomachine is considered as a reference to predict the prototype efficiency curves, Eq. 5.14. Finally, not only was it stipulated that the densities of the model and prototype were equal, but also that the number of stages z_{st} must be the same for both machines in order to respect the geometric similarity condition.

From Eq. 5.14, the only variable that can compensate the variation imposed by the efficiency correction factor is the impeller diameter of the prototype, D_{2p} . This means that, after the acquisition of the PAT characteristics, an impeller *Diameter Correction* (DC) still has to be taken into consideration, see Eq. 5.37.

$$D_{2p,DC} = D_{2M} \cdot \left(\frac{P_p}{P_M}\left(\frac{N_M}{N_p}\right)^3 \cdot f_\eta\right)^{1/5} \qquad with \qquad f_\eta = f_{\eta,SSC} \tag{5.37}$$

Afterwards, it is mandatory to evaluate the difference between the impeller diameter estimated initially $D_{2p,i}$ and the corrected impeller diameter $D_{2p,DC}$, Eq. 5.38.

$$\Delta D_{2p} = \left|D_{2p,i} - D_{2p,DC}\right| \tag{5.38}$$

In the case where $D_{2p} < 1$ mm, the difference[6] verified between both cases is barely significant and not worth the calculation procedure. However, if $\Delta D_{2p} \geq 1$ mm,then the numerical method shall be perceived as an iterative method where the initial impeller diameter is, in fact, the impeller diameter corrected at the end of the previous iteration. In the case where the numerical model stops, then te previously corrected diameter shall be considered as the final prototype PAT diameter. This correction implies the estimation of new loss values, new correction factors and, consequently, new PAT characteristics.

The iterative procedure may be stopped whenever the difference between diameters is lower than 1 mm. In this case, the previously corrected diameter shall be considered as the final prototype PAT diameter.At this stage, the characteristics of the prototype at its BEP are finally known.

To estimate the additional prototype points of operation, the remaining model points of operation

[6]Notice that the minimum value of ΔD_{2p} that allows to characterize the worthiness of an extra iteration is naturally subjective. For this work, $\Delta D_{2p} < 1$ mm is assumed as a good approximation.

shall be taken into consideration and transformed into the prototype ones using Eqs. 5.12, 5.13 and 5.14. Herein, the correction factors are equal to the correction factors estimated for the BEP.

This procedure leads not only to the prototype efficiency curve as a function of the flow rate, but as a function of the head as well.

Chapter 6

SPATEC - Efficiency Curves Scaling Program

The Scaling of PAT Efficiency Curves program or SPATEC is the Microsoft Excel implementation of the numerical methodology presented in chapter 5. This program has a database of 57 PATs, from which 35 are reverse-running centrifugal pumps. In the end, SPATEC offers the possibility of predicting PAT efficiency curves for a total of 25 distinct specific speed PATs ranging from 0.118 to 1.183. However, there are still improvements that should be applied in future work, such as the optimization of the calculation procedure and medium user-friendly interface.

Throughout this chapter, it will be seen what was the procedure that entailed the PAT database and how does the program work (i.e. how is it sectioned, what are the inputs and what should be done to attain the PAT efficiency curves).

6.1 Collection and processing of data

As explained in the beginning of section 5.1, the research developed by [90] presents a list of pumps working as turbines, each with several points of operation. Such data is extremely useful to test the validity of the formulated numerical method.

Observe Table 6.1 that represents one example (VENT PAT) of the general information usually provided for one of the 57 PATs listed in their study. The characteristics presented in this table are not always available for every PAT case, mainly the impeller outlet diameter D_2. However, searching for the original source of the information or for the type of pump listed in the characteristics section, might lead to extra information regarding the specific PAT.

The numerical methodology developed in this thesis relies on a PAT model to calculate the system characteristics of a geometrically scaled prototype. Subsequently, it uses a third PAT (previously defined as resembling prototype) that has a geometry quite similar [1] to verify how precise are the estimated results.

[1] It shall be clear that *quite similar* does not mean *equal*.

PAT	VENT084
Category:	end-suction/volute (radial flow)
Outlet diameter, D:	0.280 m
Original source:	Ventrome82

Turbine-mode BEP			
Q(l/s)	H(m)	N(rpm)	η
120.5	34.00	1550	77.9%

Performance data			
Q(l/s)	H(m)	N(rpm)	η
138.8	43.61	1550	75.8%
132.5	40.06	1550	77.1%
122.0	34.83	1550	78.1%
117.9	32.85	1550	77.9%
103.3	26.66	1550	75.0%
88.7	22.13	1550	66.8%

Table 6.1: Information regarding PAT DIED028 (adapted from [21]).

To understand which PATs have the most similar geometries, the dimensions of both machines must be scaled with similar ratios. Such relation between the prototype and the resembling prototype cannot be verified entirely once literature lacks information regarding pump geometries. Therefore, it is assumed in this work as a first approximation that, PATs with close specific speeds imply resembling geometries[2]. Off course, this condition is not necessarily true. However, at the end of the numerical methodology the deviation between both the prototype and resembling prototype diameters is calculated and its modulus evaluated. As a result of this geometry assumption, the 57 PATs were re-organized by specific speed Ω to understand which PATs come closer to each other geometrically, see Fig. 6.1 or, for more detailed information check Appendix A.1.

Ω	PUMP	Category	Fixed Variable(s)		P_{total} (kW)	D(m)
0.1172	GIDD018	End-suction/volute (radial flow)	N (rpm)	-	17.5	0.200
0.1577	STRA022	End-suction/volute (radial flow)	N (rpm)	-	3.35	0.320
0.1756	WILL026	End-suction/volute (radial flow)	N (rpm)	-	2.06	0.134
0.1799	BUSE024	End-suction/volute (radial flow)	N (rpm)	-	0.05	n/a
0.1993	SENU037	End-suction/volute (radial flow) (semi-open impeller)	N (rpm)	-	0.80	0.101
...	...	...	...	...	...	...
3.0956	MIYA348	bowl (axial flow)	H(m)	-	43.4	0.409
4.1554	SWAN496	bowl (axial flow)	Q (l/s)	-	0.274	0.203

Figure 6.1: Reorganized list of the distinct PATs provided by [90].

Afterwards, each PAT was considered as the model and possible resembling prototypes were selected. If all 57 PATs would correlate between themselves without any restriction, apart from the repetition condition, the total number of possible cases would be equal to 1596 (C_2^{57}). However, it does not make sense to apply the numerical model for two PATs with considerable specific speed differences. As such, the subsequent screening process was implemented according to the following condition: the

[2]recall the relation between dimensionless numbers and geometrically similar pumps

specific speed deviation between the prototype[3] and the resembling prototype should be lower or equal to 0.05, eq. 6.1. From this criterion it was obtained 95 cases that relate different PATs.

$$\Delta\Omega = |\Omega_p - \Omega_{rp}| \leq 0.05 \tag{6.1}$$

The specific speed deviation condition is necessary in the screening process but not sufficient. In addition to this restriction, the 95 cases must also be analyzed with respect to their geometric category, which is provided in each PAT formulae. Table 6.2 illustrates the various types of casings that are observed in the PAT list.

Category	Sub-category	Representation
Single-suction	Radial flow	”End-suction/volute (radial flow)”
	Mixed flow	”End-suction/volute (mixed flow)”
	Diffuser pump	”End-suction/volute (radial flow) (with fixed vanes)”
	Double voulte	”End-suction/volute (radial flow) (double volute)”
	Semi-open impeller	”End-suction/volute (radial flow) (semi-open impeller)”
Double suction	-	”Double-suction”
Multistage pumps	-	”Multistage (x radial flow stages)”
Submersible	Radial flow	”Submersible (radial flow)”
	Mixed flow	”Submersible (mixed flow)”
Bowl	Mixed flow	”Bowl (mixed flow)”
	Axial flow	”Bowl (axial flow)”

Table 6.2: Casing types verified in the PAT database (adapted from [90]).

If one of the previous cases combines two PATs with distinct categories, then it shall be removed from the test data. For example, a ”double-suction” PAT with a ”bowl (axial flow)” PAT: both have similar specific speeds Ω , but their geometry differs significantly, meaning, the condition of quite similar geometry that is imposed between the prototype and the resembling prototype is not respected.

Some PATs are simply described as *End-suction/volute (radial flow* (i.e. characterized in a general way) and thus, their geometry can have sub-categories that are unknown to the researcher. In this work, it is assumed that potential mismatch should not be the reason why these PATs are not be correlated with PATs that derived from its category, such as diffuser, double volute and semi-open impeller pumps. Mean while, it is also barred in mind that this consideration might impair the precision of the PAT efficiency predition. Furthermore, it was also considered that PATs whose category arise from the end-suction/volute type (at the exception of the mixed flow sub-category) can be combined between each other once their sub-category is not correlated, meaning, such specifications can coexist in the same PAT. By applying these geometry criteria to the PATs selected previously, 44 cases are excluded, remaining a total of 51 cases.

The prediction of the prototype's efficiency curve depends on the diameter of the model $D_{2,m}$. Whenever this parameter is unknown for both PATs, the estimation of the efficiency curve is not possible and the respective case must be excluded. From the 51 cases obtained after applying the type-of-casing criterion, 5 of them do not have at least one of the PATs with its diameter identified. This condition leads

[3]Remember that one of the PATs is chosen as the model while the other as the resembling prototype. However, the comparison of results is between the prototype and the resembling prototype candidate. Thus, the specific speed deviation is measured between the prototype and the resembling prototype and not the model and the resembling prototype.

now to a total of 46 cases.

Finally, as for the last restriction, it is stipulated that the rotational speed N_{rp} of the resembling prototype must be constant for the points of operation used in the analysis. These points must have the same rotational speed so that, when compared to the prototype points of operation, both efficiency curves fall over the same coordinate plane, this is, a plane in the three dimensional axis that corresponds to a certain rotational speed $N_{rp} = N_p$. Otherwise, the operating points of the resembling prototype would not represent an efficiency curve in a single rotational speed plane, see Fig. 7.11 from subsection 7.3.2. This restriction could be easily bypassed if the affinity laws were applied to the resembling prototype to achieve new points of operation with a distinct rotational speed [4]. However, the application of these laws would also affect the confidence level of the experimental results as they do not represent the reality flawlessly. To avoid additional errors, it was decided not to include in this work the cases where the transformation of the resembling prototype rotational speed N_{rp} was necessary and thus, from the previous 46 cases, 6 were excluded. At the end of the selective process there are 40 PAT cases out of the 1596 considered initially, see A.2.

6.2 Implementation and working methodology

The numerical model used to predict PAT efficiency curves was implemented using Microsoft Excel. As a consequence, the acquisition and treatment of results for each case was done in this software as well.

The program is divided into four sections: Reynolds and roughness correction, where the the initial correction factor f_H and f_η are determined (remember that f_Q was initialy assumed as equal to one); specific speed correction - smallest section of the program and useful to ensure the similar geometry condition; diameter correction and iterative process, that is a consequence of the efficiency factor f_η presence on the power similarity law; and PAT performance, where both flow rate and head efficiency curves are estimated and drawn graphically.

At the Reynolds and roughness section, the program requires the input of the best efficiency point characteristics of both the model and resembling prototype[5], yellow cells in Fig. 6.2 [6]. With such data the numerical calculations presented in chapter 5.2.2 result in the initial correction factors, f_Q, f_H and f_η, as presented down in Fig. 6.2.

[4] Recall chapter 3 - The affinity laws allow the estimation of equivalent points of operation for different values of their characteristics.

[5] Beware that, in SPATEC, *real prototype* or only *real* represents the *resembling prototype* mentioned in this work.

[6] Figure 6.2 represents only a part of section 1. Appendix B illustrates the complete section with the required calculations to obtain the characteristic correction factors.

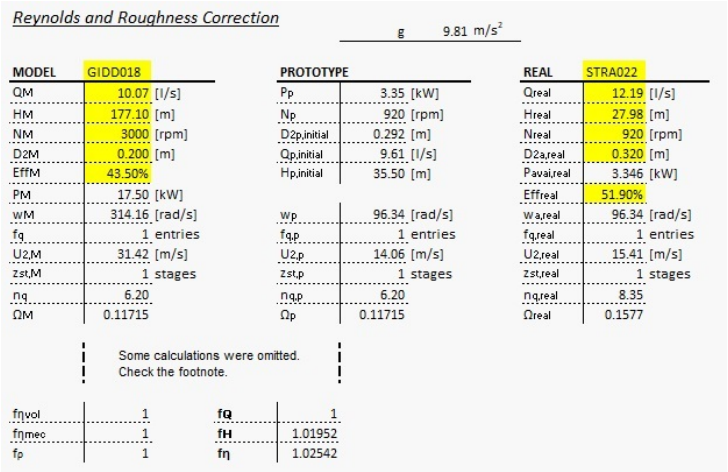

Figure 6.2: Program section 1 - Reynolds and roughness correction.

At the second stage, f_Q, f_η and the impeller diameter are corrected as a consequence of the specific speed correction, Fig. 6.3.

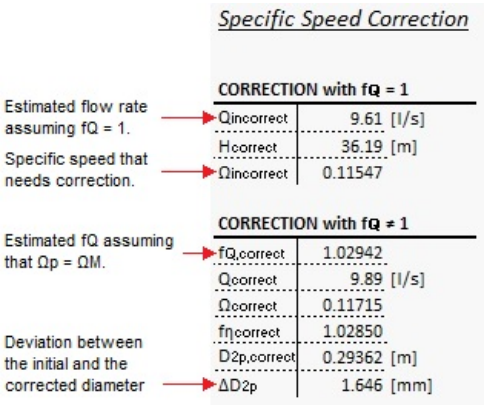

Figure 6.3: Program section 2 - specific speed correction.

The correction factors determined at the first stage are transferred to the *Initial Results* sub-section of the diameter correction section. As for the data obtained in specific speed correction section, it is imparted to the *Final Results* sub-section where the new efficiency correction factor is also calculated. Later the difference between the estimated and the corrected diameter ΔD_{2p} is calculated and used as a reference to evaluate the worthiness of the following iteration: if $\Delta D_{2p} \leq 1\ mm$, then the iterative process stops; otherwise, the initially estimated diameter shall be replaced by the corrected diameter. In this way, the calculations associated with the first and second stages are repeated and the resulting correction factors are attained with a higher precision, see Fig. 6.4.

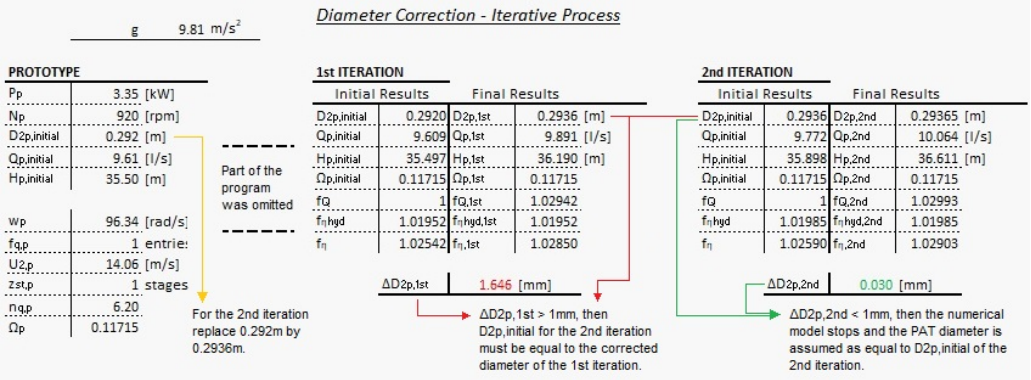

Figure 6.4: Iterative process reasoning.

Three iterations are applied for each case. However, in every cases, it is verified that the numerical method provides satisfying results for one or two iterations only. This implies that the third iteration represents an unnecessary step of the numerical method. In other words, its consideration brings into the work an excessive detail that shall be neglected, Fig. 6.5.

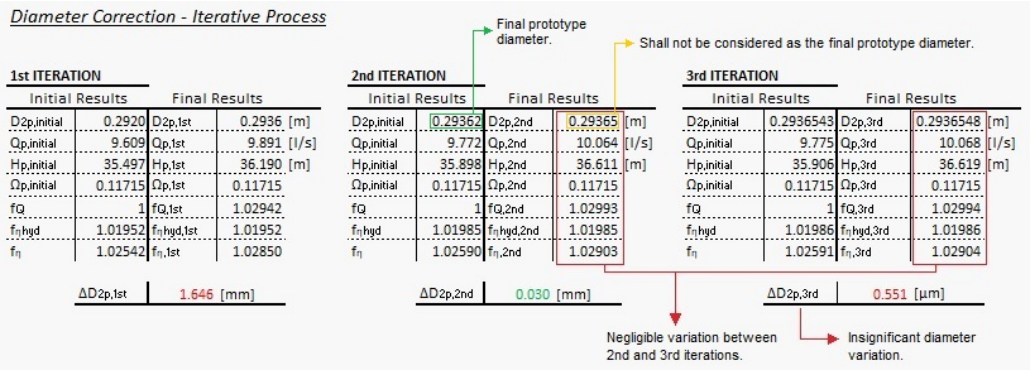

Figure 6.5: Program section 3 - diameter correction, iterative process.

If the difference in diameters drops below the one millimeter condition, the numerical method comes to an end and the achieved results correspond to the actual prototype parameters for a PAT geometrically similar to the model PAT.

The PAT Performance stage (section 4) reproduces the prototype operating points, see Fig. 6.6. Such points are achieved through the application of the correction factors and the affinity laws to the various operating points of the model. If the model has operating points with different rotational speeds, it is still acceptable to apply corrective factors and affinity laws to the model to estimate the operating points of the prototype. As defined at the end of chapter 6.1, the constant rotational speed restriction imposed to the operating points is only applied to the resembling prototype. Notice that the impeller diameter estimated at the beginning of the last iteration is the one considered in the affinity laws, and not the corrected diameter obtained at the end of that same iteration, Fig. 6.5.

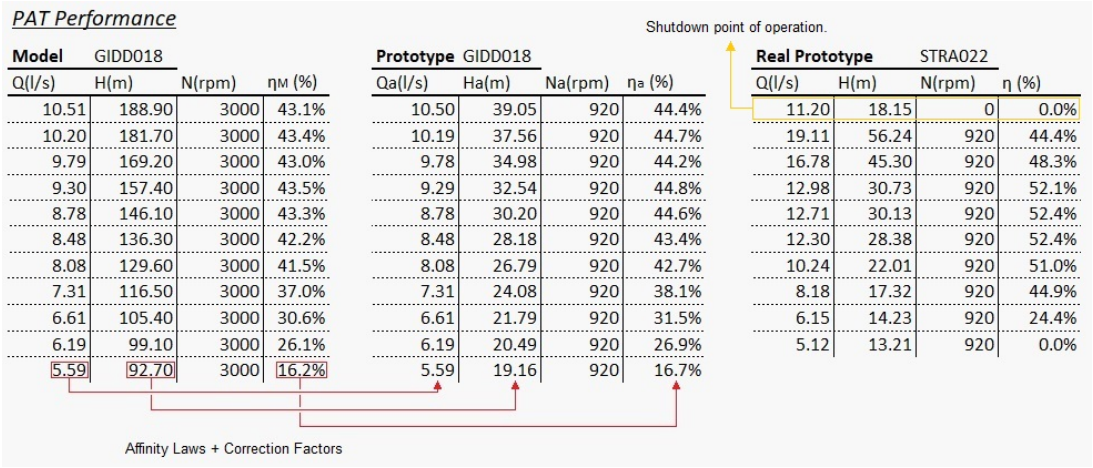

Model	GIDD018		
Q(l/s)	H(m)	N(rpm)	ηM (%)
10.51	188.90	3000	43.1%
10.20	181.70	3000	43.4%
9.79	169.20	3000	43.0%
9.30	157.40	3000	43.5%
8.78	146.10	3000	43.3%
8.48	136.30	3000	42.2%
8.08	129.60	3000	41.5%
7.31	116.50	3000	37.0%
6.61	105.40	3000	30.6%
6.19	99.10	3000	26.1%
5.59	92.70	3000	16.2%

Prototype	GIDD018		
Qa(l/s)	Ha(m)	Na(rpm)	ηa (%)
10.50	39.05	920	44.4%
10.19	37.56	920	44.7%
9.78	34.98	920	44.2%
9.29	32.54	920	44.8%
8.78	30.20	920	44.6%
8.48	28.18	920	43.4%
8.08	26.79	920	42.7%
7.31	24.08	920	38.1%
6.61	21.79	920	31.5%
6.19	20.49	920	26.9%
5.59	19.16	920	16.7%

Real Prototype	STRA022		
Q(l/s)	H(m)	N(rpm)	η (%)
11.20	18.15	0	0.0%
19.11	56.24	920	44.4%
16.78	45.30	920	48.3%
12.98	30.73	920	52.1%
12.71	30.13	920	52.4%
12.30	28.38	920	52.4%
10.24	22.01	920	51.0%
8.18	17.32	920	44.9%
6.15	14.23	920	24.4%
5.12	13.21	920	0.0%

Figure 6.6: Program section 4 - PAT performance.

Sometimes, it is also verified that the first operation point of the model or resembling prototype corresponds to the shutdown point of the PAT, meaning, the specific speed equals to zero $N = 0\ rpm$, Fig. 6.6 (operating point inside the yellow rectangle). These points are not taken into account when calculating the prototype equivalent points of operation or plotting the efficiency curves.

In addition, it is also interesting to notice the prototype operating point outcome that result from the application of the flow rate, head and efficiency similarity laws given by 5.34, 5.35 and 5.36 to the respective model parameters, see Fig. 6.6 (parameters inside red rectangles).

Finally, at the end of the program, the model, prototype and resembling prototype efficiency curves are represented graphically as a function of the flow rate Q and, subsequently, as a function of the PAT's head H, Fig. 6.7. These graphics allow to understand the variation between the model and the prototype and to evaluate the closeness of the prototype and resembling prototype curves.

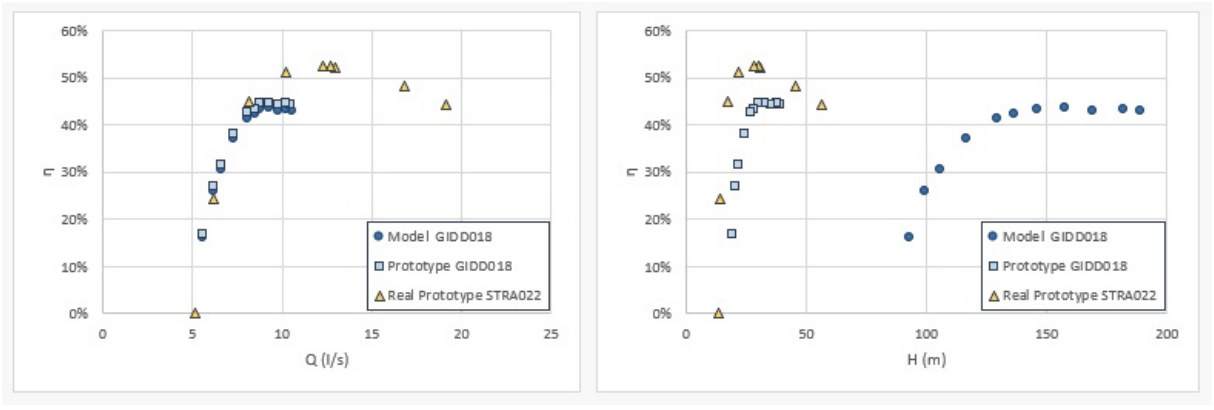

Figure 6.7: Efficiency curves as a function of the flow rate and the head.

Chapter 7

Analysis and Discussion of the Results

From the 40 cases that were selected to test the numerical model, some predicted quite successfully the prototype efficiency curves. However, there were other cases that fall short on what was verified experimentally with their respective resembling prototypes. This chapter helps understanding the accuracy of the numerical model and which parameters affect the deviation between the theoretical and experimental results.

Throughout the results discussion, the 40 cases are mentioned according to their case group instead of their particular case number. A lower, an intermediate and a upper specific speed group are assumed as the best way to divided all cases. This restructuring allow the analysis of the results in a more general way and prevent the discussion from being unnecessarily exhausting.

Even though a quantitatively equal branching of the 40 cases might seem at first as the most suitable procedure to apply (i.e. two case groups with 13 cases and the remaining with 14 cases), the model [1]specific speed difference between two consecutive cases ends-up defining the actual division. From the 1st case to the 40th, there are only three specific speed differences that stand out from the rest of the deviations: a 0.075 difference between the 15th and the 16th cases; a 0.099 deviation between the 29th and the 30th cases; and a specific speed contrast of 0.131 for the 39th and 40th cases, see Appendix A.4.

Taking into account that it is not desirable to have a group with a single case, the specific speed contrast between the 39th and 40th cases is neglected and thus, both are considered to be allocated in the same group. With such assumption, the 40 cases are placed in distinct groups according to the following approach:

- Lower group - includes all the cases that go from the 1st to the 15th case; any prototype inserted in this group has a specific speed between 0.117 and 0.250, both inclusive;

[1]The resembling prototype specific speed is merely used to evaluate the geometrical proximity between two PATs. However, the model specific speed is considered throughout the entire numerical model. Thus, it is natural to perform the cases division according to the model specific specific speed.

- Intermediate group - the cases between the 16th and 29th cases, belong to this particular group; its cases' specific speed ranges from 0.250 (exclusive) to 0.550;
- Upper group - any case equal or higher than the 30th case is integrated in this final group, with a specific speed range between 0.550 (exclusive) and 0.889. 0.902.

Lastly, it is important to understand the difference between these case group and the PAT specific speed ranges that are analyzed is this work. Whilst these case groups have specific speeds varying between 0.117 and 0.889, it does not mean that it is not possible to apply the numerical model to a PAT with higher or lower specific speed. In fact, by looking at the PAT database explicit in Appendix A.1, it is easily perceived that, for a PAT with a specific speed out of the case groups range, there might be a centrifugal-type PAT with which the correlation is possible. Later, on chapter 8 it will be seen an example where this particular case happens.

7.1 Specific speed and diameter comparison

One of the problems faced when developing this methodology is that it is impossible to know whether resembling prototypes have the same geometry as the prototypes to which they were correlated. Due to the lack of information regarding the geometry of the PATs and, in order to proceed with the efficiency prediction study, it was assumed that equal specific speeds imply equal geometries. However, as explained above, it is evident that if the prototype diameter differs considerably from the resembling prototype diameter, then the PATs have different geometries and, therefore, there is a larger error associated with the efficiency prediction.

Viewed as one of the most important variables in this work, the specific speed allows not only to represent the geometry of a PAT family, but also to evaluate the accuracy of the PAT efficiency prediction, as will be seen later in the chapter 7.2. This accuracy naturally depends on the deviation between the specific speed of the prototype and resembling prototype. Baring this in mind, see Fig. 7.1 which represents this deviation as a function of each case.

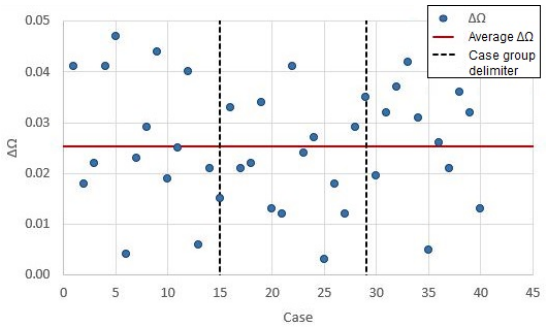

Figure 7.1: Specific speed deviation for each case.

At first sight, it is easily perceived that the difference between specific speeds is uniformely distributed. In fact, the lower and upper case groups have fairly close averages of 0.026 and 0.027, respectively. Although the intermediate group has a better mean value of 0.023, this difference is not

significant enough to disregard the uniform distribution. Consequently, it is concluded that the impact that this parameter has on the efficiency prediction is approximately similar for each of the case groups. In addition, a total average specific speed of 0.025 is perceived as a satisfying result once it is half the acceptable specific speed defined in the cases screening process (i.e. half of 0.05).

One of the outputs of the numerical model characterizes the prototype diameter. This parameter, together with the resembling prototype diameter represents a crucial feature of the case to be analyzed. Through these two variables it is possible to draw conclusions about the geometric proximity, assumed to be similar for the comparison of efficiency curves. Therefore, to understand how diameters differ across the 40 cases, it is necessary to estimate the respective absolute ΔD_{2abs} and relative ΔD_{2rel} errors. The first represents the metric difference between the prototype and the resembling prototype diameters. The second characterizes the percentage difference that the prototype diameter presents compared to the resembling prototype diameter.

If the relative error is greater than 10%, then the similar geometry condition is automatically refuted and the error associated with the efficiency prediction higher. Otherwise (i.e. $\leq$10%), the geometric relationship between the prototype and the resembling prototype is maintained as similar and the error associated with efficiency prediction lower.

Afterwards, analyze the graphs of Fig. 7.2 that represent the absolute and relative errors for each of the 40 cases studied in this work.

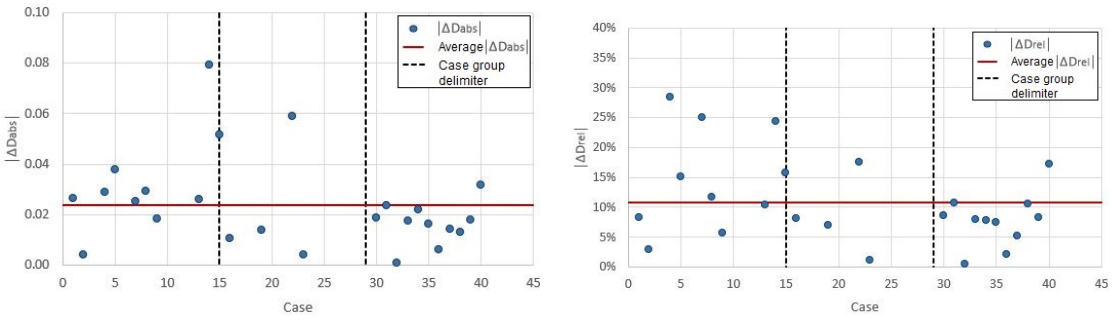

(a) (b)

Figure 7.2: (a) Diameter absolute error, (b) Diameter relative error.

It is clear that, from the 40 cases to which the numerical model has been applied, there is a high number of cases that do not illustrate the diameter difference (more specifically, 15 cases), Fig. 7.2. This is due to the fact that for these respective cases the diameter of the resembling prototype is not explicit and, therefore, the absolute and relative errors are not determined.

In addition, of the 15 missing cases, 9 correspond to the intermediate case group, 5 to the lower case group and 1 to the upper case group. Now, since the perception of these errors is essential for the evaluation of the similar geometry condition, it can be concluded that the intermediate case group has the lower error certainty associated with the efficiency prediction[2]. It is also expected that, since the diameter difference of the high case group is smaller than that of the low case group, the error associated with the prediction of efficiency curves is smaller for the first than for the second.

[2]In other words, without knowledge of the diameter difference it is not possible to assess the validity of the resembling prototype efficiency curve and thus, the corresponding certainty is lower.

From the 25 cases that present results for the diameter differences, 14 are below the 10% mark and 4 between 10% and 12%. In an overall point of view 72% of the cases (excluding the invalid cases) exhibit approximately an impeller diameter difference lower or equal to 10% which is assumed as a satisfying result.

7.2 Efficiency comparison

To compare the efficiency curves between the prototype and the resembling prototype, it is necessary to determine the efficiencies of the prototype that correspond to the diverse flow rates and heads parameters of the resembling prototype. This alignment allows the calculation of the absolute and relative errors associated with each operating point, $\Delta\eta_{abs}$ and $\Delta\eta_{rel}$ respectively.

Once the flow rates and heads of the resembling prototype are always different from the model flow rates and heads, it is not possible to estimate the efficiency of the prototype through the affinity laws. A linear regression is then the most appropriate method to estimate these efficiencies.

Microsoft Excel allows to characterize linear regressions (also defined as trendlines) with polynomials whose degrees vary between the second and the sixth degree. To understand which polynomial degree suits better the flow rate and head efficiency curves, the determination coefficient R^2 inherent to the trendline must be evaluated. This parameter expresses the quality that a certain polynomial equation has to approximate itself from the prototype operating points. On a scale from 0 to 1, a polynomial equation that follows perfectly the operating points as a determination coefficient equal to 1, whilst an equation with a determination coefficient of 0 shall not, by any means, be used to represent the selected characteristic points.

In each case, the determination coefficient is attained for the trendlines with polynomial degrees varying between 2 and 6. Appendix C represents all the determination coefficients associated with the various polynomials. Instead of selecting a particular polynomial degree for each case, it is considered that a polynomial degree for each group of cases is a preferable assumption.

Afterwards, for each group of cases, it is observed the minimal determination coefficient R^2 corresponding to the distinct polynomial degrees. With these values, it is assessed the modulus and percentage increment of the determination coefficient R^2 between two consecutive polynomial degrees (for example, the improvement between a 3rd and a 4th degree polynomial). Finally, the polynomial degree is chosen whenever the percentage increase falls below the 10% mark (i.e. $\Delta R^2 < 10\%$), once these reduced polynomial enhancements do not justify the expansion of the polynomial to the next degree. Table 7.1 clarifies the chosen polynomial degree for the different case groups as a function of the respective efficiency curve (i.e. flow rate or head efficiency curve).

	Lower group	Intermediate group	Upper group
Flow rate trendline	2º	3º	4º
Head trendline	4º	4º	6º

Table 7.1: Trendline degrees for each case group.

With the degrees of the polynomial equations acknowledge, the respective trendlines are easily

obtained. To ensure that no rounding errors are associated with the rounding of the trendline coefficients, these coefficients are specified with twenty decimal places. This inexorability comes from the fact that, for ten decimal places and sometimes even fifteen decimal places, Excel does not predict successfully the prototype efficiency. Therefore, twenty decimal places is considered as the most reliable assumption.

By replacing the resembling prototype flow rates and heads on the prototype trendline, it is determined the absolute and relative error associated with the numerical method developed in this work. Analogously to the diameter prediction, the absolute error $\Delta\eta_{abs}$ is simply characterized by the modular difference between the prototype and resembling prototype efficiencies, while the relative error $\Delta\eta_{rel}$ represents the percentage deviation between the estimated and the experimental results, Eqs. 7.1 and 7.2 respectively.

$$\Delta\eta_{abs} = |\eta_{rp} - \eta_p| \tag{7.1}$$

$$\Delta\eta_{rel} = \frac{\Delta\eta_{abs}}{\eta_{rp}} = \frac{|\eta_{rp} - \eta_p|}{\eta_{rp}} \tag{7.2}$$

For example, if the estimated efficiency of a certain PAT equals 30% but the experimental results demonstrate that, in fact, the maximum efficiency of that PAT is equal to 60%, then the prediction has an absolute error of 30% ($\Delta\eta_{abs} = |60\% - 30\%| = 30\%$) and a relative error of 50% ($\Delta\eta_{rel} = 30\%/60\% = 50\%$).

A feasible comparison of results and subsequent error calculation can only occur between the minimum and maximum flow rates or heads of the prototype (once again, depending on the efficiency curve type being studied). Inside this numerical range it is possible to perceive the linear evolution that the trendline should have based on the prototype operating points. However, beyond this range, the behavior of the prototype efficiency curve is unpredictable and thus, any efficiency estimation shall be pursued with special attention and with a different methodology.

Such beyond-range estimations might be interesting to study whenever there are resembling prototype operating points left to compare, see Fig. 6.7 (yellow curve exceeds the pale blue curve in both flow rate and head efficiency curves). To estimate the prototype efficiency outside its admissible range, it is necessary to incur to the extrapolation method. Once this methodology is easily susceptible to error, there are some restrictions that must be taken into account when extrapolating new prototype operating points:

- $\Delta e_{abs} < \Delta\eta_{abs}$ - if the absolute error Δe_{abs} between the extrapolated efficiency and the resembling prototype is lower than the absolute error of the closer limiting point of operation $\Delta\eta_{abs}$, then the extrapolation is valid, Fig. 7.3 Point B;

- $\Delta e_{rel} \leq 10\%$ - for a particular extrapolated point, if the absolute error increase is 10% lower or equal to the absolute error of the closer limiting point of operation, then the extrapolation is also valid, Fig. 7.3 Point A;

- Otherwise, the extrapolation is assumed as invalid. For example, whenever a extrapolated point is characterized by a negative efficiency $\eta_p < 0.0\%$, Fig. 7.3 Point C.

	Q(l/s)	η_{rp}	η_{TL}	$\Delta\eta_{abs}$	$\Delta\eta_{rel}$	Δe_{abs}	Δe_{rel}	
	2.29	55.9%	55.8%	-0.1%	-0.2%			
	2.19	56.2%	55.4%	-0.8%	-1.5%			
	2.00	56.6%	53.2%	-3.4%	-5.9%			
	1.80	55.2%	49.5%	-5.7%	-10.3%			
	1.60	51.0%	44.1%	-6.9%	-13.5%			
	1.40	44.4%	37.0%	-7.4%	-16.8%			
A	1.20	35.8%	28.1%	-7.7%	-21.6%	0.3%	-3.9%	valid
B	1.01	23.9%	17.8%	-6.1%	-25.7%	1.3%	-17.5%	valid
	0.81	10.5%	5.3%	-5.2%	-49.6%	2.2%	-30.1%	valid
C	0.71	0.0%	-1.5%	-1.5%	#DIV/0!	6.0%	-80.0%	neg. eff

Figure 7.3: Possible extrapolating outcomes.

Finally, with these rules established, the absolute and relative errors associated with the prototype efficiency prediction are evaluated. This evaluation extends itself through the 40 cases and includes the extrapolated points as well.

Q(l/s)	η_{rp}	η_{TL}	$\Delta\eta_{abs}$	$\Delta\eta_{rel}$	Δe_{abs}	Δe_{rel}
19.11	44.4%	-134.4%	-178.8%	-402.8%	172.1%	-2545.4%
16.78	48.3%	-58.4%	-106.7%	-221.0%	100.0%	-1479.0%
12.98	52.1%	21.1%	-31.0%	-59.5%	24.3%	-358.9%
12.71	52.4%	24.6%	-27.8%	-53.0%	21.0%	-310.8%
12.30	52.4%	29.5%	-22.9%	-43.7%	16.1%	-238.8%
10.24	51.0%	44.2%	-6.8%	-13.25%		
8.18	44.9%	42.8%	-2.1%	-4.68%		
6.15	24.4%	25.6%	1.2%	4.72%		
5.12	0.0%	10.8%	10.8%	#DIV/0!	9.6%	837.2%

(a)

H(m)	η_{rp}	η_{TL}	$\Delta\eta_{abs}$	$\Delta\eta_{rel}$	Δe_{abs}	Δe_{rel}
56.24	44.4%	-108.7%	-153.1%	-344.7%	329.8%	-2203.9%
45.30	48.3%	33.8%	-14.5%	-30.0%	6.7%	-86.0%
30.73	52.1%	44.3%	-7.8%	-15.0%		
30.13	52.4%	44.2%	-8.2%	-15.7%		
28.38	52.4%	43.6%	-8.8%	-16.7%		
22.01	51.0%	32.6%	-18.4%	-36.1%		
17.32	44.9%	1.3%	-43.6%	-97.0%	61.0%	-169.0%
14.23	24.4%	-40.3%	-64.7%	-265.2%	229.2%	-635.2%
13.21	0.0%	-59.2%	-59.2%	#DIV/0!	#DIV/0!	#DIV/0!

(b)

Figure 7.4: (a) Flow rate efficiency curve errors, (b) Head efficiency curve errors.

Observe Fig. 7.4. The resembling prototype points of operation inside the valid operation range are represented between the two red lines (in black color), while the extrapolated points of operation are placed outside this region. They can either be illustrated by the red or green color in case the extrapolation is valid or not, respectively. In addition, it might happen that a particular point of operation is represented by the red color. This entails that the prediction is incorrect and happens every time the resembling prototype efficiency is lower than 0.0%.

In order to understand the impact that each error has, it is selected for all cases the minimum and maximum errors[3] verified amongst all operating points and its values plotted in the same graphic. Taking into account that there are absolute and relative errors for both the head and flow rate efficiency curves, four graphics must be plotted to represent the different characteristic errors, see Fig. 7.5.

At the end of the x-axis, these graphics also represent four distinguished error ranges: the first three correspond to the average values of the distinct case groups - lower, intermediate/medium and upper specific speed groups ; and the fourth illustrates the overall error average of the 40 cases.

After calculating the errors, if a certain case does not exhibits at least two valid operating points for a particular curve type, then the respective case is omitted from the corresponding error analysis (including the averages). For example, in the 27th case - efficiency transformation between ENGE057 and THOM062 PATs - due to the lack of resembling prototype operating points, only one operating point

[3]Notice that the absolute and relative minimum errors do not correspond necessarily to the same operating point. See for instance Fig. 7.4: for the flow rate efficiency curve, the operating point with the minimum absolute error (1.2%) does not represent the operating point with the minimum relative error (once 4.72% $>$ 4.68%). The same applies for the absolute and relative maximum errors.

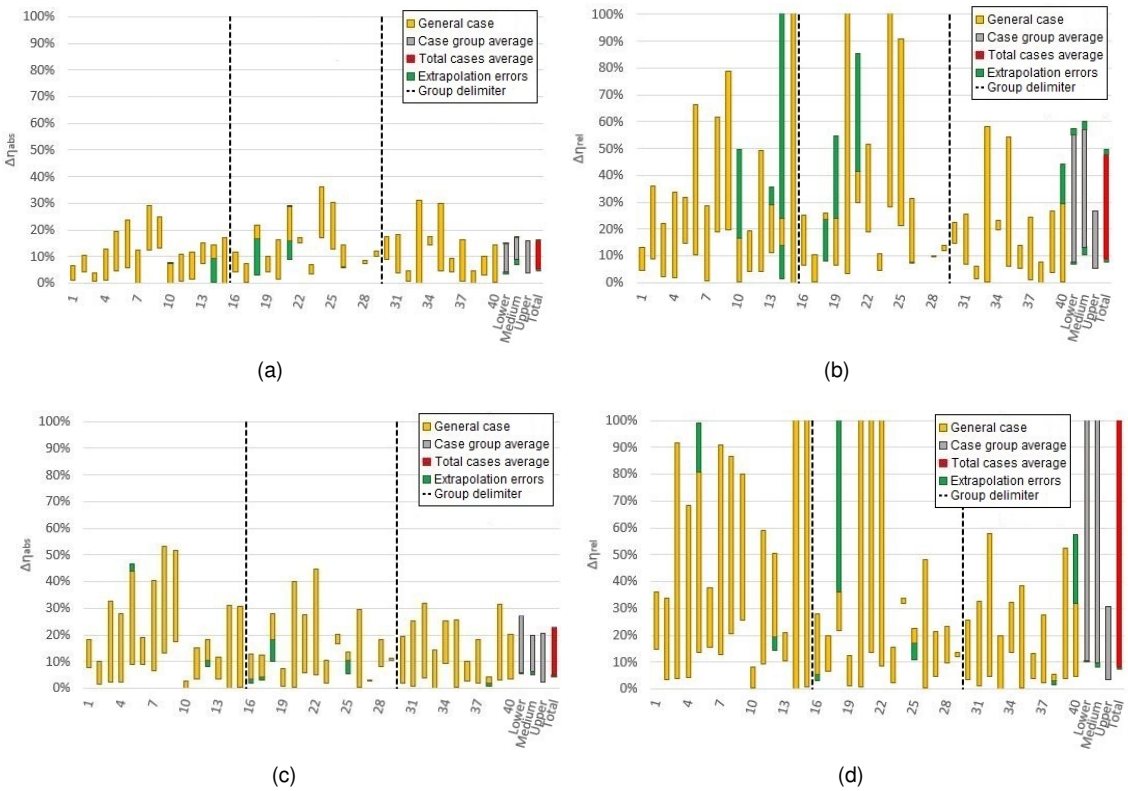

Figure 7.5: Absolute and relative error ranges for the total operating range of the prototype. (a) flow rate absolute error range, (b) flow rate relative error range, (c) head absolute error range, (d) head relative error range.

is validated in the flow rate efficiency curve, while two points are validated for the head curve. As a consequence, this case is omitted from the error graphics related to the flow rate, but not from the error graphics related to the head, check the 27th case through Fig. 7.5(a) and 7.5(b).

Prior to any results' analysis, it is still important to understand the following:

- The relative error is a parameter that represents the deviation that a prediction has in relation to the experimentally verified result. For example, estimating that a turbine has an efficiency of 90% when in reality is verified an efficiency of 85%, is different from predicting a 40% efficiency for another turbine and it exhibits an experimental efficiency of 35%. For both cases a deviation of 5% is verified between the estimated and the experimental values. However, an error of 5% at 35% has a greater impact than 5% at 85%: 14.29% variation for the first case and 5.88% for the second, respectively. It is up to the researcher to decide whether or not the deviation is acceptable to the project being studied.

- The deviations between prototype and resembling prototype efficiencies may acquire positive or negative values if the estimated efficiency for the prototype is above or below the efficiency of the similar prototype, respectively. However, for the purpose of comparing the errors between the 40 cases, it makes more sense that the deviation between both efficiencies is evaluated in module. Hence, the graphics of Fig. 7.5 present only positive values for the error range.

- If one of the graphics of Fig. 7.5 shows an extrapolated operating point whose increase or error

reduction (both absolute and relative) is quite significant, then this point has a positive impact on efficiency prediction. This large gap between the errors is accepted in the extrapolation of operating points because its absolute error is smaller than the absolute error of the nearest operating point that is within the range of flow rate or head. That is, the estimated operating point is associated with more accurate prediction. However, this precision improvement does not prevent the considerable increase of the relative error inherent to the respective absolute error. Hence, the high variations of the relative error for several cases with extrapolated operating points.

- As applied for the extrapolation of operating points, if an estimated point within the range of flow rate and head has a negative efficiency, then it is automatically excluded from the analysis.

That being said, to analyze the obtained results it is made a division of the different error ranges. For each case, it is assumed that both the range length and its minimum value can have high or low values, see Table 7.2.

Qualifier	Error Range Length	Initial Error Value
Small-Small	$\leq$10%	$\leq$10%
Small-Large	$\leq$10%	$>$10%
Large-Small	$>$10%	$\leq$10%
Large-Large	$>$10%	$>$10%

Table 7.2: Qualifier description according to error range length and initial error value.

Naturally, this range characterization has a different meaning depending on the type of error analyzed (absolute or relative). For the absolute error, a small range length means that the prototype and resembling prototype efficiency curves exhibit an approximately similar shape within the allowable range of operation, Fig. 7.6(a). Otherwise (i.e. a large range length), the curves present considerable differences in their shape, Fig. 7.6(b). With respect to the minimum error, for ranges having a minimum error below 10%, it is assumed that the prototype and resembling prototype curves have at least one zone in which the prediction is quite satisfactory, Fig. 7.6(a). Beyond this value, the deviation between the two curves exceeds the acceptable limit, Fig. 7.6(b).

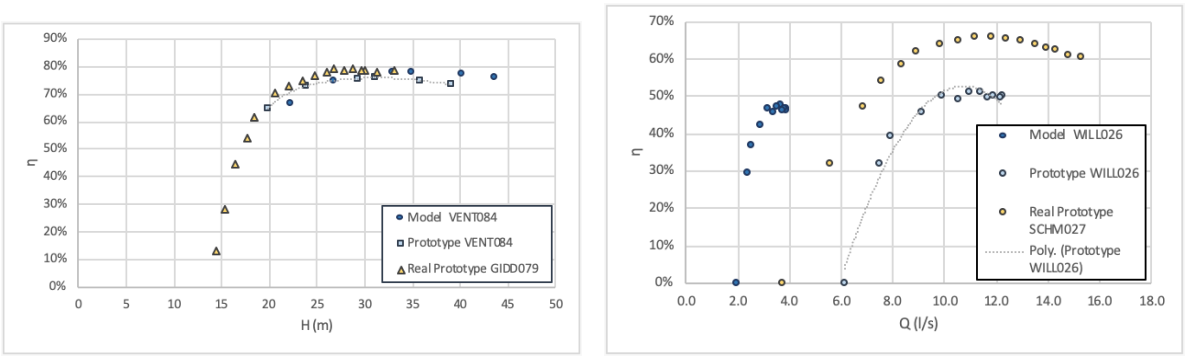

(a) (b)

Figure 7.6: (a) Small error range length and small minimum error, (b) Large error range length and large minimum error.

For the relative error, a range that has a large length characterizes the particular case where the un-

certainty of the predicted results varies significantly, whereas a range with a small length has predictions with constant levels of uncertainty. If, for a relative error range, the minimum error is less than or equal to 10% (i.e. qualified as small), then the respective range is known for having low uncertainty values, while a minimum error range greater than 10% identifies the case where the uncertainty of predicted efficiencies is high. Through correlations between the distinct qualifiers the following definitions are set:

For absolute errors

- Small-Small [4] - Similar curve shape with at least 1 zone of the efficiency curve predicting successfully the prototype efficiency;
- Small-Large - Similar curve shape, but with no region of the efficiency curve predicting successfully the prototype efficiency;
- Large-Small - Considerable differences in the efficiency curve shape with at least 1 zone of the curve predicting successfully the prototype efficiency;
- Large-Large - Considerable differences in the efficiency curve shape with no region of the efficiency curve predicting successfully the prototype efficiency;

For relative errors

- Small-Small - Constant and low uncertainty when compared to the real efficiency value (resembling prototype efficiency);
- Small-Large - Constant and high uncertainty when compared to the real efficiency value;
- Large-Small - Variable uncertainty with low and high values when compared to the real efficiency value (can have acceptable uncertainties if the relative error is lower or equal to 10%);
- Large-Large - Variable uncertainty with medium and high values when compared to the real efficiency value (the uncertainties are not satisfying as the relative error is higher than 10%);

With the groups defined above, each range of the four graphics of Fig. 7.5 is organized according to their characteristics. In this way, the analysis of the graphics is naturally facilitated.

From Fig. 7.5(a), the different cases are organized as shown in Table 7.3 below. In most cases it is found that the error range has either a small length and an initial error (Small-Small qualifier), or is defined as a large interval, but with a small initial error (Large-Small qualifier). Therefore, for the flow-dependent efficiency curve most cases have at least one region of the curve that successfully predicts the prototype efficiency. As for the shape of the curves, there is an almost equal number of cases with similar and not similar efficiency curves, 17 to 15 cases, respectively. Although cases with similar efficiency curves are the most common, the overall average exhibits a Large-Small range, with the error ranging from 4.9 % to 15.8 %. This is due not only to the many cases of the small range family with almost high range lengths (cases 10, 14, 26), but also to the cases of the large range family with range lengths much larger than 10% (cases 6, 21, 33, 35).

[4] The qualifiers are defined according to the following norm: *Range-Minimum error*

Qualifier	Cases	Total
Small-Small	1, 2, 3, 10, 12, 13, 16, 17, 19, 23, 26, 28, 30, 32, 36, 38, 39	17
Small-Large	22, 29, 34	3
Large-Small	4, 5, 6, 7, 11, 14, 15, 18, 20, 21, 31, 33, 35, 37, 40	15
Large-Large	8, 9, 24, 25	4
		39[5]

Table 7.3: Case distribution through the qualifying groups for the flow rate absolute error.

The lower and upper case groups have a similar error range, with the error varying between 3.6 % - 14.7 % and 3.8 % - 15.9 %, respectively. As for the intermediate case, it deviates slightly from the previous two groups with an error range of 7.0 % - 17.1 %. However, this deviation is not considered to be significantly harmful compared to the ranges of the other two groups.

It is still interesting to note that for the upper case group no error increments are observed through extrapolations, see Fig 7.5(a). Although there are cases with extrapolated operating points, none of them present their error module outside the error range obtained within the admissible operating range. This is not only due to the lack of points to extrapolate, but also to the incapacity for these points to respect the extrapolation rules defined above.

Afterwards, note the absolute errors dispersion corresponding to the various efficiency curves dependent on the head, see Table 7.4. These error ranges correspond to Fig. 7.5(c) presented above.

Qualifier	Cases	Total
Small-Small	2, 10, 12, 13, 17, 19, 23, 25, 27, 36, 38	11
Small-Large	24, 29	2
Large-Small	1, 3, 4, 5, 6, 7, 11, 14, 15, 16, 18, 20, 21, 22, 26, 28, 30, 31, 32, 33, 34, 35, 37, 39, 40	25
Large-Large	8, 9	2
		40

Table 7.4: Case distribution through the qualifying groups for the head absolute error.

In more than half of the cases, and consequently, the overall average, the efficiency curves are characterized by having slightly similar shapes and approaching each other in at least one region of the head operating range, successfully predicting the efficiency of the prototype (Large-Small qualifier). Still, 11 of the 40 cases have a similar curve profile with at least a region with satisfactory predictions as well (Small-Small qualifier). The Large-Small characterization comes from the rough prediction of operating points in the linear zone. As seen earlier, small variations in flow rate or head in the linear operating zone result in sudden efficiency variations and, consequently, for slightly similar curves, these small variations are reflected in large efficiency deviations. Compared to the flow-dependent efficiency curves, the head efficiency curves display more frequently operating points in the linear region, therefore, it is understandable that the absolute and relative errors are greater in the second type of curves.

The overall absolute error associated with the head efficiency curves is defined by the range between 4.6% and 22.9%. The intermediate and upper case groups correspond to the error intervals of 5.2% - 20.0% and 2.6% - 20.6%, respectively. Regarding the lower group, it has a maximum error approximately

[5]Recall that for both the absolute and relative errors dependent on the flow rate, the 27th case is not included in the error analysis due to lack of operating points.

7% higher than the other two sets of cases, with an error ranging from 5.6% to 27.4%.

Proceed with the analysis of the results illustrated by Fig. 7.5(b). Table 7.5 presents the distribution of the different cases according to the various efficiency curves dependent n the flow rate relative error range.

Qualifier	Cases	Total
Small-Small	1, 23, 28, 32, 36, 38	6
Small-Large	29, 30, 34	3
Large-Small	2, 3, 4, 7, 10, 11, 12, 14, 15, 16, 17, 18, 19, 20, 26, 31, 33, 35, 37, 39, 40	21
Large-Large	1, 5, 6, 7, 8, 9, 12, 13, 18, 21, 25, 34	9
		39

Table 7.5: Case distribution through the qualifying groups for the flow rate relative error.

In most cases, the behavior of relative error as a function of flow is expressed by the Large-Small qualifier, meaning, the numerical model estimates the prototype efficiencies with both low and high uncertainties. However, there is a close proximity to the Large-Large behavior type as the minimum overall error is 7.7% (9.0% without extrapolation), a value very close to the 10% limit. For the same set of cases it is still important to note the existing maximum error of 49.7%.

Compared to the lower and intermediate case groups, the upper group has a substantially better relative error, this is, with a higher confidence level: 5.5% - 26.6% compared to 6.9% - 57.4% and 10.6% - 60.3% of the lower and intermediate groups, respectively. This is due not only to the fact that there are few operating points in low efficiency zones for the upper group, but also because the predicted points have low absolute errors, which in turn implies low relative errors. As for the two remaining groups, great absolute errors and low efficiency point of operation in the linear region result in extreme relative errors, as in cases 14, 15, 20, 24 and 25 where it is observed relative errors of 105.1%, 317.0%, 297.0%, 107.2% and 90.7%, respectively.

Note that, although some of these relative errors are very high, the absolute error associated with these points might be very low. For example, in the 14th case, where the extrapolating point resulted in a 105.1% relative error, the absolute difference inherent to this point is only 5.7%. Its relative error is extremely high because a 5.7% efficiency deviation from a 5.4% experimental efficiency is more than the double of the expected efficiency. However, a 5.7% deviation is naturally accepted near BEP. It must be up to the researcher to decide whether or not this deviation is considered as satisfactory.

Lastly, the qualifying groups and their respective cases for the head relative error are presented in Table 7.6. This table is also a result of the error ranges showed in Fig. 7.5(d). Just like what happens to the flow rate relative error, the head relative error is defined by a High-Low profile type. As mentioned previously for the absolute error, the existence of many operating points in the linear region with low efficiencies, results in relative errors with values even higher than the ones verified for the relative error dependent of the flow rate. The overall relative error range starts with a minimum value of 7.5% and reaches a maximum of 138.8%. This automatically induces a sense of great uncertainty regarding the efficiency prediction as a function of the head. For the inferior and intermediate groups, the relative error varies between 10.0% - 127.4% and 8.1% - 235.9%, while the upper specific speed group is characterized by an error range between 3.7% and 30.7%.

Qualifier	Cases	Total
Small-Small	10, 36, 38	3
Small-Large	24, 29	2
Large-Small	2, 3, 4, 11, 14, 15, 16, 17, 19, 20, 22, 23, 26, 27, 28, 30, 31, 32, 33, 35, 37 39, 40	23
Large-Large	1, 5, 6, 7, 8, 9, 12, 13, 18, 21, 25, 34	12
		40

Table 7.6: Case distribution through the qualifying groups for the head relative error.

An important aspect that affects the error prediction for each curve is the lack of precision inherent to the trendline equation drawn from the excel. Throughout the error calculation it is verified that, in many cases, the trendline did not represent successfully the behavior of the prototype efficiency points. In most of those cases there is an offset between the trendline and the operating points that shall be improved in order to attain better results of the exact error associated with the efficiency prediction methodology.

Even though the extrapolation method is interesting and enriching at a data point of view, it is verified that very few extrapolating points meet the specifications mentioned above. Such fact might be due to trendlines with high polynomial degrees, to lower prototype efficiency curves (in comparison with the resembling prototype curves) and to slight changes between both curves in the linear operating region. Trendlines with high polynomial degrees usually change drastically its curvature outside the prototype limiting range and, as a consequence, diverge significantly from the resembling prototype operating points. In addition, it can also occur that smaller prototype efficiency curves result in negative efficiencies at the beginning of the resembling prototype linear zone and, as such, are not considered. Finally, slight changes between the prototype and resembling prototype curves at the linear operating region end up increasing the absolute error once the slope in this region is very high and thus, are not validated as well.

		Error Range Without Extrapolation	Error Range With Extrapolation
Flow rate	$\Delta\eta_{abs}$	5.7% - 15.8%	4.9% - 15.8%
	$\Delta\eta_{rel}$	9.0% - 47.7%	7.7% - 49.7%
Head	$\Delta\eta_{abs}$	5.1% - 22.9%	4.6% - 22.9%
	$\Delta\eta_{rel}$	8.3% - 138.3%	7.5% - 138.8%

Table 7.7: Error comparison between the average cases with and without extrapolation.

7.2.1 Efficiency prediction for a range between $\pm$10% of BEP

The errors presented presented and analyzed before demonstrate a numerical model that is associated not only with a high relative error, but also absolute. Such errors have often been justified on the premise that operating points in the linear zone induce quite significant errors. In order to show that these operating points actually have a high impact on the overall model errors, this sub-section discusses the different errors for flow rates and heads that are greater or smaller by 10% on the BEP characteristics.

The procedure to obtain such errors varies slightly from the procedure described before in the full range of flow rates and heads. For this particular situation, it is only necessary to calculate the new

operating ranges of the efficiency curve and to take into account which operating points of the resembling prototype fit into the considered range. The operating range reduction is naturally associated with fewer operating points once the range between ±10% of the BEP is often inserted in the BEP region, and thus the points of the other operating zones are discarded from this analysis. Below, it is presented the different absolute and relative errors for each case, this time, considering only the interval between ±10% of BEP, Fig 7.7.

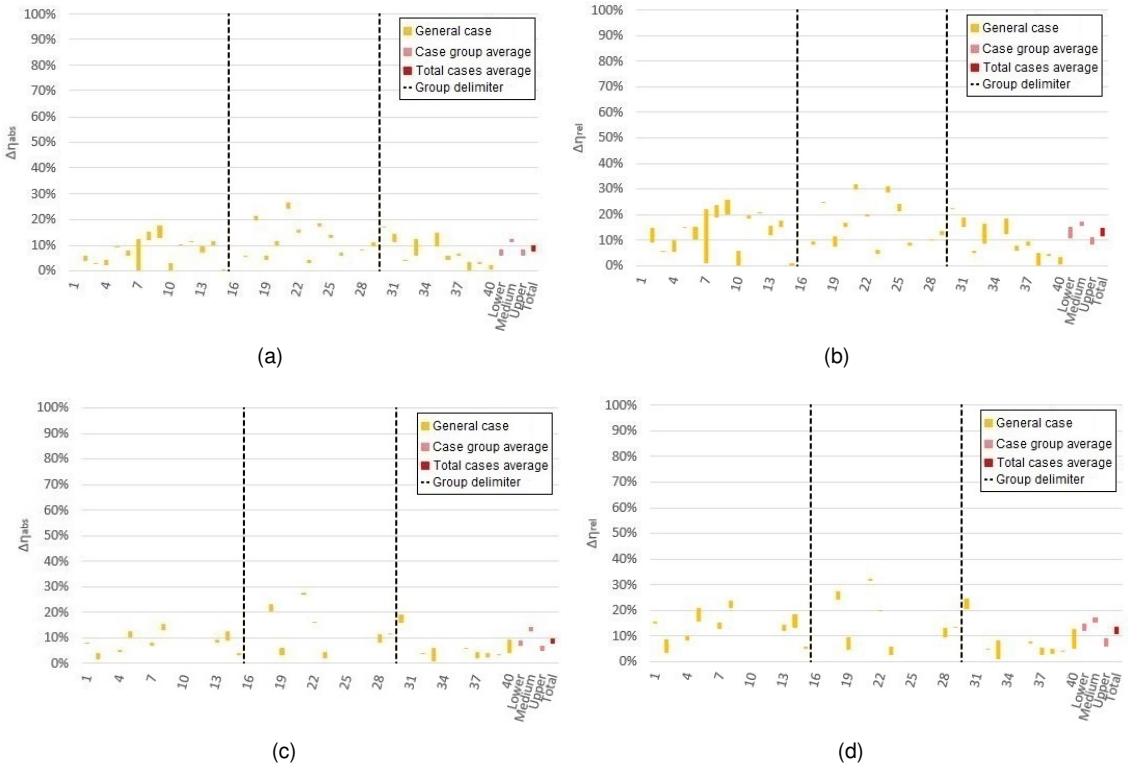

Figure 7.7: Absolute and relative error ranges for ±10%BEP. (a) flow rate absolute error range, (b) flow rate relative error range, (c) head absolute error range, (d) head relative error range.

Although Fig. 7.7 clearly imparts that the length of each error range diminished significantly, it is essential to understand carefully what happened to each error range so that a general outcome of the results can be formulated. From the results obtained for the total operation range, the error ranges for the ±10% of BEP operation range can evolve according to the following principles:

- Increase of the minimum error while the maximum error remains constant;
- Decrease of the maximum error while the minimum error remains constant;
- Increase of the minimum error while the maximum error decreases;
- Both the maximum and minimum errors remain constant.

For the four graphics it is determined which type of range variation corresponds to each case. The cases are then organized by types of variation in order to obtain the absolute and relative frequencies, see Tables 7.8 and 7.9. From these data it is easily predicted which variations occurs more or less frequently.

		e_{min} ↑	e_{max} ↓	e_{min} ↑ & e_{max} ↓	Both const.	Total	Left aside
Flow rate	$\Delta\eta_{abs}$	3	15	17	1	36	4
	$\Delta\eta_{rel}$	3	17	16	0	36	4
Head	$\Delta\eta_{abs}$	1	9	14	0	24	16
	$\Delta\eta_{rel}$	0	9	15	0	24	16

Table 7.8: Absolute frequency of range variation.

		e_{min} ↑	e_{max} ↓	e_{min} ↑ & e_{max} ↓	Both const.	Total
Flow rate	$\Delta\eta_{abs}$	8.3%	41.7%	47.2%	2.7%	100%
	$\Delta\eta_{rel}$	8.3%	47.2%	44.5%	0%	100%
Head	$\Delta\eta_{abs}$	4.2%	37.5%	58.3%	0%	100%
	$\Delta\eta_{rel}$	0%	37.5%	62.5%	0%	100%

Table 7.9: Relative frequency of range variation.

By analyzing the graphics from Fig. 7.7, it is verified that, in most cases, the total error range either reduces its maximum error and withholds its minimum error, or increases its minimum error and reduces its maximum error (compared to the graphics presented in Fig. 7.5). It is only a few percentage of the cases that increase the minimum error and keep the maximum error constant. Except for the 27th case of the flow rate efficiency curve that remains with the same error range length, the range restriction here applied truly increases the certainty of the error associated with the efficiency curves.

For the flow rate absolute error, it is possible to notice a significant difference in the particular averages between the intermediate case group and the lower and upper groups. The overall average range varies between 8.1% and 10.3%, which is a quiet positive reduction when compared to the previous flow rate range obtained for the total operation range equal to 4.9% - 15.8%.

Regarding the head absolute error, despite the lack of data, it is still possible to assure some improvements in the previous error range. The maximum average error decreased more than 50%, with an exact value of 56.8%. However, the minimum average error increased 3.3%, which represents approximately a 71.1% increment in relation to the previous minimum error of 4.6%. In addition, the length of the range reduced drastically from 18.3% to 2.0%, which ensures a much higher certainty regarding the error associated with the head efficiency prediction near the BEP.

When it comes to the relative errors, the valuable change is felt specially in the head efficiency curve, where the average error range varies from 7.5% - 138.8% to 10.8% - 13.7% (specifically with a length reduction of 128.4%). These extreme variations are due to the fact that near the BEP not only the high efficiencies imply lower relative errors, but also because the absolute error between the operating points is lower than the in other zones (mainly, the linear operating zone). Alike the head curves, the flow rate curves also display a very satisfying result once their ranges varies from 7.7% - 49.7% to 11.6% - 14.8% (length reduction of 38.8%). Table 7.10 present the overall error ranges for each graphic and for both ranges of operation.

Finally, it is interesting to understand that the case group that has the lower differences in diameter (upper group) corresponds to the group that has the lower absolute and relative errors. Additionally, it is important to perceive that the 2nd case group is probably the group with the highest diameter differences once the error is influenced by the geometry and the second group has the biggest errors.

		±10% BEP Operating Range	Total Operating Range
Flow rate	$\Delta\eta_{abs}$	8.1% - 10.3%	4.9% - 15.8%
	$\Delta\eta_{rel}$	11.6% - 14.8%	7.7% - 49.7%
Head	$\Delta\eta_{abs}$	7.9%% - 9.9%	4.6% - 22.9%
	$\Delta\eta_{rel}$	10.8% - 13.7%	7.5% - 138.8%

Table 7.10: Error comparison between the adjusted and the total operating ranges.

7.3 Extensive analysis of specific cases

This section analyzes several cases to whom the numerical method was applied. To avoid an exhaustive analysis of the results, a detailed assessment is solely applied to specific cases (that can later be used as a reference): for the first example, the results represent a PAT efficiency curve prediction that has a quiet successful level of precision; the second example characterizes the estimation of the prototype efficiency curve through model operating points that are not integrated in the same plane of reference as the model's BEP, once the rotational speed N was not kept constant; lastly, the third example denotes a specific case where the prototype and resembling prototype efficiency curves exhibit a significant deviation between each other, meaning, the prediction was not accurate.

7.3.1 Example 1 - Accurate Case 2

The first example deepened in this work relates a prototype, whose geometry corresponds to the STRA022's PAT, with the WILL026 PAT, both with 2.06 kW. In addition, the prototype characteristics are attained through the STRA022 model PAT with a power of 3.35 kW, resulting in a small power difference between the model and prototype of 1.29 kW. The figure below display the model, the prototype and the resembling prototype characteristics.

MODEL	STRA022		PROTOTYPE			REAL	WILL026	
Q_M	12.19	[l/s]	P_a	2.06	[kW]	Q_{real}	3.754	[l/s]
H_M	27.98	[m]	N_a	3100	[rpm]	H_{real}	55.86	[m]
N_M	920	[rpm]	$D_{2a,initial}$	0.140	[m]	N_{real}	3100	[rpm]
D_{2M}	0.320	[m]	$Q_{a,initial}$	3.45	[l/s]	$D_{2a,real}$	0.134	[m]
Eff_M	51.90%		$H_{a,initial}$	60.87	[m]	$P_{avai,real}$	2.057	[kW]
P_M	3.35	[kW]				Eff_{real}	47.00%	
w_M	96.34	[rad/s]	w_a	324.63	[rad/s]	$w_{a,real}$	324.63	[rad/s]
f_q	1	entries	$f_{q,a}$	1	entries	$f_{q,real}$	1	entries
$U_{2,M}$	15.41	[m/s]	$U_{2,a}$	22.74	[m/s]	$U_{2,a}$	21.75	[m/s]
$z_{st,M}$	1	stages	$z_{st,a}$	1	stages	$z_{st,a}$	1	stages
n_q	8.35		$n_{q,a}$	8.35		$n_{q,real}$	9.30	
Ω_M	0.15774		Ω_a	0.15774		Ω_{real}	0.1756	

Figure 7.8: Model, prototype and resembling prototype characteristics of accurate case 2.

Both the model and the prototype have a specific speed Ω of 0.1577, whilst the resembling prototype specific speed is equal to 0.1756. Just like this specific speed difference, the impeller diameter difference is also very satisfying (more specifically, 0.140 - 0.134 = 0.006 m). This proximity between the resembling prototype diameter and the estimated prototype diameter reinforces the similar geometry assumption supposed previously.

After two iterations it is achieved the following correction factors: flow rate factor f_Q = 0.94046; head factor f_H = 0.95990; and efficiency factor f_η = 0.92709;

With the different operating points of the model, the operating points of the prototype are determined. For the purpose of comparing the predicted and experimental results, the operating points of the resembling prototype are included in the same graphics. Below, Fig. 7.9 shows the obtained results:

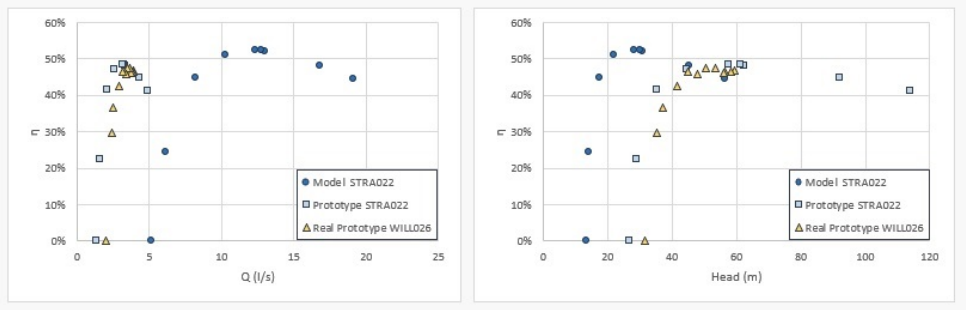

Figure 7.9: Accurate Case 2 - Efficiency curves.

Assuming that the polynomials that best represent the flow rate and head efficiency curves are the 2nd and 4th degrees, respectively, the following equations are drawn from Microsoft Excel:

$$\eta(Q) = -0.08617286867650980000 \cdot Q^2 + 0.61268277410686900000 \cdot Q - 0.56742286835792000000,$$

with $R^2 = 0.901728565519691$.

$$\eta(H) = -0.00000016808538147988 \cdot H^4 + 0.00005134587073198230 \cdot H^3 - 0.00562663990182888000 \cdot H^2 + 0.25979285646850300000 \cdot H - 3.76395567789074000000,$$

with $R^2 = 0.950117844043881$.

These polynomials together with the prototype operating ranges allow the determination of the absolute and relative errors corresponding to each operating point, see Fig. 7.10.

Q(l/s)	ηrp	ηTL	Δηabs	Δηrel
3.90	46.7%	51.1%	4.4%	9.5%
3.88	46.4%	51.3%	4.9%	10.5%
3.80	46.6%	51.7%	5.1%	10.9%
3.72	46.2%	51.9%	5.7%	12.4%
3.63	47.6%	52.1%	4.5%	9.5%
3.50	47.5%	52.1%	4.6%	9.8%
3.37	46.0%	51.9%	5.9%	12.7%
3.15	46.6%	50.8%	4.2%	8.9%
2.91	42.4%	48.6%	6.2%	14.6%
2.51	36.7%	42.8%	6.1%	16.6%
2.38	29.6%	40.2%	10.6%	35.9%
1.95	0.0%	30.0%	30.0%	#DIV/0!

(a)

H(m)	ηrp	ηTL	Δηabs	Δηrel
59.42	46.7%	48.4%	1.7%	3.5%
58.16	46.4%	49.1%	2.7%	5.8%
56.33	46.6%	50.2%	3.6%	7.6%
56.11	46.2%	50.3%	4.1%	8.8%
53.36	47.6%	51.6%	4.0%	8.5%
50.51	47.5%	52.6%	5.1%	10.7%
47.99	46.0%	52.8%	6.8%	14.9%
44.79	46.6%	52.2%	5.6%	11.9%
41.71	42.4%	50.0%	7.6%	18.0%
37.25	36.7%	43.6%	6.9%	18.9%
35.42	29.6%	39.6%	10.0%	33.8%
31.42	0.0%	27.3%	27.3%	#DIV/0!

(b)

Figure 7.10: (a) Flow rate efficiency curve errors, (b) Head efficiency curve errors.

Through Fig. 7.9 it is possible to see that all operating points of the resembling prototype are within the operating range of the prototype. Hence, it is not necessary to appeal to the extrapolating method to compare the efficiencies between the prototype and the resembling prototype.

Note that for both the flow rate and head-dependent systems, the prototype and resembling prototype efficiency curves have similar shapes and at least in one region of these curves, the prediction is made successfully. As previously explained, this is due to the fact that both flow rate and head efficiency curves have a Small-Small profile once the absolute error ranges from 4.4% - 10.6% and 1.0% - 10.0%, respectively. Regarding the relative error, both prototype curves transmit the uncertainty level associated with the Large-Small profile. This implies a variable uncertainty within the operating range and, consequently, results in high or low uncertainty values, see Table 7.11. Case 2 ranges always shows better error limits than the overall ranges, except for the flow rate minimum relative error, where the error is higher. Therefore, it is concluded that this case presents a very successful outcome.

		Case 2	Total Operating Range
Flow rate	$\Delta\eta_{abs}$	4.4% - 10.6%	4.9% - 15.8%
	$\Delta\eta_{rel}$	8.9% - 35.9%	7.7% - 49.7%
Head	$\Delta\eta_{abs}$	1.7% - 10.0%	4.6% - 22.9%
	$\Delta\eta_{rel}$	3.5% - 33.8%	7.5% - 138.8%

Table 7.11: Error comparison between case 2 and the total oprating range.

7.3.2 Example 2 - Special Case 30

By superficially analyzing the efficiency curves of Fig. 7.11, there is something that immediately stands out in relation to the majority of the cases analyzed in this paper: the efficiency curves of the model exhibit completely different forms from those that are normally presented. In most cases, the efficiency curves are represented for a particular rotational speed, which is equivalent to say, in the same plane of reference. However, in this special case the model operating points are associated with different rotational speeds and thus, they only represent part of parallel efficiency curves. To achieve the prototype efficiency curve and, subsequently, compare it with the resembling prototype curve it is necessary to restrict the prototype operating points to a particular rotational speed, which must be equal to the BEP rotational speed so that the correction factors are successfully applied.

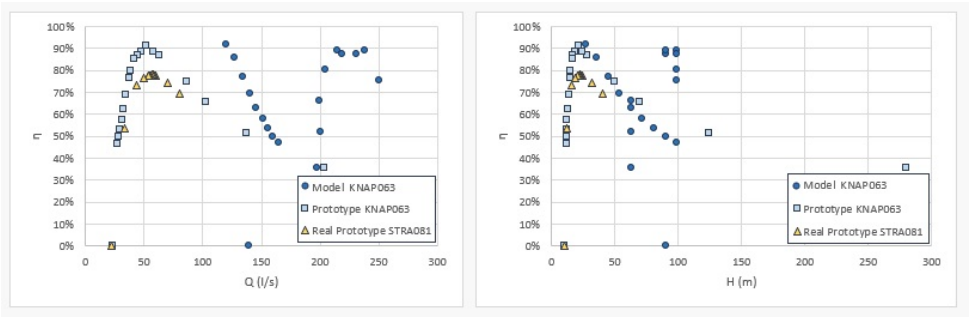

Figure 7.11: Special Case 30 - Efficiency curves.

The 30th case, which correlates the KAP063 and the STRA081 PATs, is one of the special cases presented in this project (along with cases 31, 33, 34th, 35th and 37th). Below, Fig. 7.12 represents the properties of each PAT.

MODEL	KNAP063		PROTOTYPE			REAL	STRA081	
Q_M	267.30	[l/s]	P_a	12.18	[kW]	Q_{real}	56.15	[l/s]
H_M	128.70	[m]	N_a	1500	[rpm]	H_{real}	22.11	[m]
N_M	2500	[rpm]	$D_{2a,initial}$	0.238	[m]	N_{real}	1500	[rpm]
D_{2M}	0.340	[m]	$Q_{a,initial}$	54.81	[l/s]	$D_{2a,real}$	0.219	[m]
Eff_M	90.50%		$H_{a,initial}$	22.65	[m]	$P_{avai,real}$	12.179	[kW]
P_M	337.48	[kW]				Eff_{real}	77.90%	
w_M	261.80	[rad/s]	w_a	157.08	[rad/s]	$w_{a,real}$	157.08	[rad/s]
f_q	1	entries	$f_{q,a}$	1	entries	$f_{q,real}$	1	entries
$U_{2,M}$	44.51	[m/s]	$U_{2,a}$	18.67	[m/s]	$U_{2,a}$	17.20	[m/s]
$z_{st,M}$	1	stages	$z_{st,a}$	1	stages	$z_{st,a}$	1	stages
n_q	33.83		$n_{q,a}$	33.83		$n_{q,real}$	34.86	
Ω_M	0.63905		Ω_a	0.63905		Ω_{real}	0.65857	

Figure 7.12: Model, prototype and resembling prototype characteristics of special case 30.

In this particular case it is intended to calculate the efficiency curve of a prototype with a 12.18 kW power from a geometrically similar model with 337.48 kW. In the end, the curve obtained will be compared with the experimental curve of a PAT with a geometry close to that of the prototype. In fact, although the specific speed difference between the prototype and the resembling prototype is low (0.65857 - 0.63905 = 0.01952), the impeller diameter difference is high (0.238 - 0.219 = 0.019) ad a significant error may arise from this deviation.

Unlike the 2nd case, this special case exhibits satisfying correction factors right after the first iteration of the numerical model. The correction factors for the flow rate f_Q, the head f_H and the efficiency f_η correspond to the values of 0.99913, 0.99942 and 0.99311, respectively.

Once again, the application of these factors along with the affinity laws results in the prototype operating points illustrated in both graphics of Fig. 7.11. The trendline that best fits the flow rate efficiency curve has a polynomial degree equal to 4, whilst a 6 polynomial degree suits best the head efficiency trendline. Notice the influence that the trendline equation has on the error associated with the efficiency prediction, namely on the prototype efficiency curve dependent on the head: extreme fluctuations are verified on the polynomial response. Seeking for alternative polynomials that represent even better the prototype operating points is something that must be taken into account.

The polynomial equations that correspond to this case are the following:

$$\eta(Q) = -0.00000002777246683934 \cdot Q^4 + 0.00001312013998033880 \cdot Q^3 - 0.00212702706596029000 \cdot Q^2 + 0.13485930730655200000 \cdot Q - 1.95965726295986000000,$$

with $R^2 = 0.928985311928852$.

$$\eta(H) = -0.00000000011475819293 \cdot H^6 + 0.00000006484307141949 \cdot H^5 - 0.00001247073747246640 \cdot H^4 + 0.00107597624822131000 \cdot H^3 - 0.04464601234793930000 \cdot H^2 + 0.84492901136476600000 \cdot H - 4.88311694044233000000$$

with $R^2 = 0.933531479648039$.

With these equations and the operating ranges defined by the prototype minimum and maximum operating points, the absolute and relative errors shown in Fig. 7.13 are obtained.

Q(l/s)	η_{rp}	η_{TL}	$\Delta\eta_{abs}$	$\Delta\eta_{rel}$	Δe_{abs}	Δe_{rel}
80.11	69.4%	79.5%	10.1%	14.5%		
70.18	74.5%	89.0%	14.5%	19.5%		
60.00	77.5%	94.9%	17.4%	22.4%		
58.68	77.8%	95.2%	17.4%	22.3%		
57.55	78.1%	95.3%	17.2%	22.0%		
56.83	78.1%	95.3%	17.2%	22.1%		
56.05	77.9%	95.3%	17.4%	22.4%		
55.05	77.9%	95.2%	17.3%	22.2%		
54.24	77.9%	95.1%	17.2%	22.0%		
53.34	77.6%	94.8%	17.2%	22.2%		
50.06	76.4%	93.3%	16.9%	22.1%		
43.59	73.2%	86.4%	13.2%	18.0%		
33.45	53.7%	62.8%	9.1%	16.9%		
22.63	0.0%	14.8%	14.8%	#DIV/0!	5.7%	62.8%

(a)

H(m)	η_{rp}	η_{TL}	$\Delta\eta_{abs}$	$\Delta\eta_{rel}$	Δe_{abs}	Δe_{rel}
40.43	69.4%	59.0%	-10.4%	-15.0%		
31.70	74.5%	67.8%	-6.7%	-9.0%		
24.77	77.5%	88.9%	11.4%	14.7%		
23.66	77.8%	91.9%	14.1%	18.1%		
22.72	78.1%	94.0%	15.9%	20.4%		
22.48	78.1%	94.5%	16.4%	21.0%		
22.07	77.9%	95.2%	17.3%	22.3%		
21.64	77.9%	95.9%	18.0%	23.1%		
21.12	77.9%	96.5%	18.6%	23.8%		
20.71	77.6%	96.8%	19.2%	24.7%		
18.72	76.4%	96.0%	19.6%	25.6%		
15.47	73.2%	82.8%	9.6%	13.2%		
12.50	53.7%	51.9%	-1.8%	-3.4%		
10.37	0.0%	14.1%	14.1%	#DIV/0!	12.3%	-681.7%

(b)

Figure 7.13: (a) Flow rate efficiency curve errors, (b) Head efficiency curve errors.

From both the flow rate and head efficiency curves, only the null efficiency points of the resembling prototype are outside the operating range and thus, these are the only points whose efficiency is extrapolated. However, the extrapolation is not valid since the absolute errors in both cases increase by more than 10 % compared to the absolute error previously verified.

Observe the absolute and relative errors shown in Fig. 7.13. From these it can be concluded that even for an error range length of 8.3% the flow rate-dependent efficiency curves are approximately similar in shape and that, at least in one of the curves region the efficiency is well predicted (Small-Small qualifier). Regarding the relative error, the Small-Large profile indicates that the prediction uncertainty is high, but its variation is considerably low. For the head efficiency curves, the characteristic profiles indicate that these curves do not have a similar shape and that the associated error can assume both low and high values of uncertainties. However, in at least one zone of these curves, the efficiency prediction is made successfully (see the linear operating zone for the respective case, Fig. 7.11). The distinct shapes are justified by the oscillatory behavior that the sixth degree polynomial adopts.

When compared to the absolute and relative overall errors, the head efficiency curves exhibit very satisfying results as their error ranges are always lower than the overall ranges. As for the flow rate efficiency curves, despite finding the errors limits within the overall error ranges, the relative maximum error is the only error that improves compared to the overall limits. The minimum errors increase by almost 100% (85.7% for the absolute minimum error and 88.3% for the relative minimum error), while the absolute maximum error increases by 10.1%, see Table 7.12. In a general point of view, it is found that this case has a satisfying efficiency prediction, even if its flow rate curve could achieve better results.

		Case 30	Total Operating Range
Flow rate	$\Delta\eta_{abs}$	9.1% - 17.4%	4.9% - 15.8%
	$\Delta\eta_{rel}$	14.5% - 22.4%	7.7% - 49.7%
Head	$\Delta\eta_{abs}$	1.8% - 19.6%	4.6% - 22.9%
	$\Delta\eta_{rel}$	3.4% - 25.6%	7.5% - 138.8%

Table 7.12: Error comparison between case 30 and the overall range.

7.3.3 Example 3 - Inaccurate Case 9

As it has been seen for most cases, not all cases have satisfactory predictions of the efficiency curves. The 9th case, which correlates the WILL026 and DIED028 PATs, is one of them. See Fig. 7.14 which describes the characterization of each PAT considered in the numerical model, meaning, the model, the prototype and the resembling prototype characteristics.

MODEL	WILL026		PROTOTYPE			REAL	DIED028	
Q_M	3.75	[l/s]	P_a	107.48	[kW]	Q_{real}	49.53	[l/s]
H_M	55.86	[m]	N_a	3000	[rpm]	H_{real}	221.2	[m]
N_M	3100	[rpm]	$D_{2a,initial}$	0.301	[m]	N_{real}	3000	[rpm]
D_{2M}	0.134	[m]	$Q_{a,initial}$	41.37	[l/s]	$D_{2a,real}$	0.325	[m]
Eff_M	47.00%		$H_{a,initial}$	264.81	[m]	$P_{avai,real}$	107.479	[kW]
P_M	2.06	[kW]				Eff_{real}	68.80%	
w_M	324.63	[rad/s]	w_a	314.16	[rad/s]	$w_{a,real}$	314.16	[rad/s]
f_q	1	entries	$f_{q,a}$	1	entries	$f_{q,real}$	1	entries
$U_{2,M}$	21.75	[m/s]	$U_{2,a}$	47.36	[m/s]	$U_{2,a}$	51.05	[m/s]
$z_{st,M}$	1	stages	$z_{st,a}$	1	stages	$z_{st,a}$	1	stages
n_q	9.30		$n_{q,a}$	9.30		$n_{q,real}$	11.64	
Ω_M	0.17561		Ω_a	0.17561		Ω_{real}	0.2199	

Figure 7.14: Model, prototype and resembling prototype characteristics of case 9.

For a model with 2.06 kW, it is intended to predict its efficiency curve when it has a power equal to 107.5 kW. The existing power gap might naturally induce some errors that are not envisaged in the numerical model.

The predicted impeller diameter differs significantly from the resembling prototype, namely with a gap of 0.024 m (0.325 m for the resembling prototype and 0.301 m for the prototype). In addition, the specific speed deviation between the prototype and the resembling prototype high as well. With a value of 0.044 the specific speed difference almost reaches the maximum acceptable difference between two specific speeds.

At the end of the 2nd iteration the correction factors are equal to f_Q = 1.08661, f_H = 1.05694 and f_η = 1.09098. With these factors and through the affinity laws it is obtained the prototype efficiency curve. Figure 7.15 illustrates this curve as well as the model and resembling prototype efficiency curves.

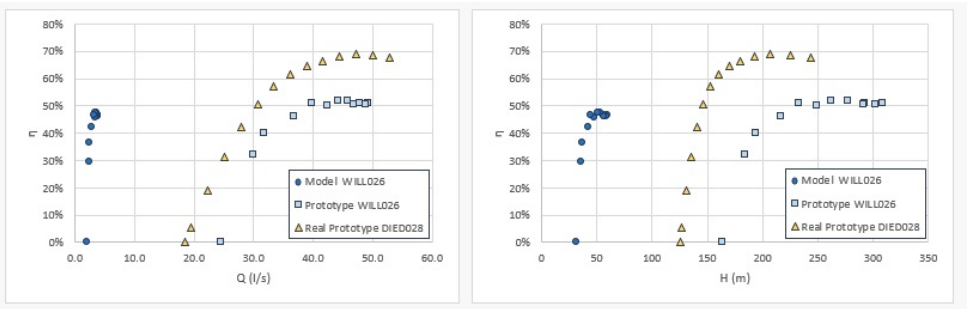

Figure 7.15: Inaccurate Case 9 - Efficiency curves.

Notice in Fig. 7.15 that many operating points of the resembling prototype exceed the prototype operating range at all limits except the upper error limit for the head-dependent curve. This means that extrapolations must be used several times to estimate the prototype efficiency of these operating points. Unfortunately, as will be seen below, no extrapolated point respects the extrapolation rules imposed to the numerical model. This mainly comes from the fact that the prototype efficiency curve has negative

efficiencies beyond the minimum operating value. However, in several times, it also happens that the absolute error increases by more than 10% compared to the absolute error found at the limit of the operating range.

Once the 2nd and 9th cases belong to the same case group, the polynomial degrees for the flow rate and head-dependent trendlines are also equal to the 2nd and 4th degrees, respectively. Contrary to what was verified for the 2nd case, the corresponding polynomial degrees represent in a better way the behavior of the different operating points. Below it is presented the polynomial equations and the corresponding determination coefficients for each curve type.

$$\eta(Q) = -0.00144081629750967000 \cdot Q^2 + 0.12432806534275300000 \cdot Q - 2.14569383445420000000,$$

with $R^2 = 0.964582087229808$.

$$\eta(H) = -0.00000000586791503372 \cdot H^4 + 0.00000611254330035590 \cdot H^3 - 0.00238230741804508000 \cdot H^2 + 0.41196330575655800000 \cdot H - 26.17878907545140000000,$$

with $R^2 = 0.995818242173203$.

Having the trendlines and the prototype operating ranges defined, the absolute and relative errors associated with each operating point are easily estimated.

Q(l/s)	ηrp	ηTL	Δηabs	Δηrel	Δeabs	Δerel
52.81	67.7%	40.2%	-27.5%	-40.7%	9.8%	-55.5%
50.05	68.7%	46.8%	-21.9%	-31.9%	4.2%	-23.9%
47.26	68.9%	51.2%	-17.7%	-25.7%		
44.48	68.0%	53.4%	-14.6%	-21.5%		
41.69	66.6%	53.3%	-13.3%	-19.9%		
38.91	64.7%	51.1%	-13.6%	-21.1%		
36.12	61.7%	46.5%	-15.2%	-24.6%		
33.40	57.0%	40.0%	-17.0%	-29.9%		
30.66	50.5%	31.2%	-19.3%	-38.3%		
27.89	42.2%	20.1%	-22.1%	-52.4%		
25.08	31.5%	6.6%	-24.9%	-79.0%		
22.28	19.2%	-9.1%	-28.3%	-147.3%	3.4%	-13.7%
19.52	5.4%	-26.8%	-32.2%	-595.9%	7.3%	-29.3%
18.56	0.0%	-33.4%	-33.4%	#DIV/0!	8.6%	-34.4%

(a)

H(m)	ηrp	ηTL	Δηabs	Δηrel	Δeabs	Δerel
243.30	67.7%	50.4%	-17.3%	-25.6%		
224.90	68.7%	49.5%	-19.2%	-27.9%		
207.20	68.9%	46.2%	-22.7%	-33.0%		
192.70	68.0%	39.1%	-28.9%	-42.5%		
179.90	66.6%	27.5%	-39.1%	-58.7%		
169.60	64.7%	13.0%	-51.7%	-80.0%		
160.40	61.7%	-5.1%	-66.8%	-108.3%	15.1%	-29.1%
152.90	57.0%	-24.2%	-81.2%	-142.4%	29.4%	-56.9%
146.60	50.5%	-43.6%	-94.1%	-186.4%	42.4%	-81.9%
140.70	42.2%	-65.1%	-107.3%	-254.2%	55.5%	-107.3%
135.40	31.5%	-87.3%	-118.8%	-377.2%	67.1%	-129.6%
130.60	19.2%	-110.1%	-129.3%	-673.4%	77.5%	-149.9%
126.50	5.4%	-131.7%	-137.1%	-2538.5%	85.3%	-164.9%
125.30	0.0%	-138.4%	-138.4%	#DIV/0!	86.6%	-167.5%

(b)

Figure 7.16: (a) Flow rate efficiency curve errors, (b) Head efficiency curve errors.

For both flow rate and head efficiency curves, the errors demonstrate that the prototype and resembling prototype curves have a distinct shape, whereas no zone of the prototype curve is successfully predicted and the associated error is quite variable with high and, sometimes even extreme, values. The behavior of this case is justified by the Large-Large profile that characterizes it. Along with the 8th case, these are the only cases that have the four types of error defined by this profile (which naturally imparts that the 8th case is not satisfying as well), recall Tables 7.3, 7.4, 7.5 and 7.6 from sub-chapter 7.2.

Apart from the maximum relative error of the head efficiency curve, all error limits in case 9 exceed the overall error limits. For the absolute error, the minimum errors for both the flow rate and head-dependent curves are even close to the maximum acceptable error for most cases, Table 7.13. Therefore, it is concluded that this case is very unsatisfactory since the inherent errors deviate considerably from the expected results (i.e. at least within the overall error ranges).

		Case 9	Total Operating Range
Flow rate	$\Delta\eta_{abs}$	13.3% - 24.9%	4.9% - 15.8%
	$\Delta\eta_{rel}$	19.9% - 79.0%	7.7% - 49.7%
Head	$\Delta\eta_{abs}$	17.3% - 51.7%	4.6% - 22.9%
	$\Delta\eta_{rel}$	25.6% - 80.0%	7.5% - 138.8%

Table 7.13: Error comparison between case 9 and the overall range.

7.4 Sensitivity Analysis

In addition to the analysis of the errors associated with efficiency predictions, as to the differences between the specific speeds and diameters of the prototype and resembling prototype, it is also interesting to study the sensitivity of the numerical model when certain parameters of its system are subject to variations that consider are significant.

As explained in chapters 4 and 5, there are several factors that contribute to the efficiency differences between two PATs, most notably the roughness ε and the Reynolds Number Re.

Roughness changes are naturally justified by differences that may exist in the material constituting the PATs, whereas Reynolds number variations may result from the change in various system characteristics, such as the angular velocity of the blades (dependent on the rotational speed and, subsequently, on the fluid velocity), the impeller outlet diameter and the kinematic viscosity of the fluid (which varies with the fluid's temperature). In order to facilitate the sensitivity analysis it is assumed in this work that the Reynolds number varies only with fluid viscosity. As such, the PAT geometry and its rotation speed are kept constant.

Just like the efficiency transformation pays attention to roughness and Reynolds number, it is important to understand what impact these factors have on the correction factors imposed on the model operating points (which successively result in the prototype operating points). To do so, in each of the 40 cases, it is studied separately the effect that a variation of $\pm$10% of roughness[6] or kinematic viscosity has on the efficiency prediction.

Take the particular case where the impeller roughness and kinematic viscosity are 64μm and 1.2$\times10^{-6}$ m^2/s for both the model and prototype. From this condition each case is divided into different systems shown below[7].

- System A - Increase of 10% of the kinematic viscosity which automatically implies a reduction in the Reynolds number. The roughness of each PAT is kept constant. Briefly, ν_M = ν_p = 1.32$\times10^{-6}$ m^2/s and $\varepsilon_{imp,M}$ = $\varepsilon_{imp,p}$ = 64 μm;
- System B - Decrease of 10% of kinematic viscosities without modification of PAT roughness. The former assume values of 1.08$\times10^{-6}$ m^2/s, whilst the seconds keep the values of 64 μm;
- System C - Increased impeller roughness by 10% to a corresponding value of 70.4 μm. Additionally, the kinematic viscosity is preserved, meaning, ν_M = ν_p = 1.2$\times10^{-6}$;

[6]Note that in this numerical model the roughness of a PAT was estimated from the impeller roughness. Therefore, to understand the influence of this factor on the efficiency prediction, it is only necessary to change the same roughness that the others automatically change.

[7]When it is said that a variation in roughness or cinematic viscosity is applied, naturally the variation is simultaneously applied to the model and prototype since in both cases these two parameters are assumed to be equal.

- System D - Kinematic viscosity stipulated on the values of 1.2$\times 10^{-6}$ m^2/s with a reduction 10% of the PATs roughnesses, $\varepsilon_{imp,M}$ = $\varepsilon_{imp,p}$ = 57.6 μm.

To avoid a further extensive analysis of the final results it is feasible to directly compare the correction factors obtained at the end of the numerical model rather than to calculate the new prototype operating points and then to compare the efficiency curves. In this way it is possible to understand the displacement imposed by the correction factors in the respective efficiency curves facilitating the numerical processing.

Recall in the numerical model that the initial assumption that f_Q = 1 subsequently implies a correction in the estimated prototype diameter. Since, to different systems correspond not only different corrective factors, but also different prototype diameters, it is still interesting to study the variation that this diameter undergoes when changing roughness and kinematic viscosities.

Applying the procedure defined above to each of the 40 cases studied in this work it is obtained the different results presented in the following figures. Figure 7.17 illustrates the variation of correction factors f_Q, f_H and f_η and the prototype diameter D_{2p} when each case is subject to system A and B, this is, when only the cinematic viscosity changes by $\pm$10%. As for Fig. 7.18, it represents the impact that the variation of the PAT roughness has on the efficiency prediction and real geometry of the prototype.

See also Table 7.14 which indicates the maximum, minimum and mean modulus variations of correction factors and estimated prototype diameter.

		f_Q	f_H	f_η	D_{2p}
+10% ε	Max	0.22%	0.14%	0.22%	0.10%
	Avg	0.04%	0.03%	0.05%	0.00%
	Min	0.00%	0.00%	0.00%	0.00%
-10% ε	Max	0.20%	0.13%	0.23%	0.01%
	Avg	0.05%	0.03%	0.05%	0.00%
	Min	0.00%	0.00%	0.00%	0.00%
+10% ν	Max	0.25%	0.18%	0.21%	0.01%
	Avg	0.05%	0.03%	0.04%	0.00%
	Min	0.00%	0.00%	0.00%	0.00%
-10% ν	Max	0.26%	0.18%	0.22%	0.10%
	Avg	0.05%	0.03%	0.05%	0.00%
	Min	0.00%	0.00%	0.00%	0.00%

Table 7.14: Percentual variation of each factor.

Combining Figs. 7.17 and 7.18 with Table 7.14 it is easily concluded that the numerical model is slightly or simply not sensitive to the variation of its roughness and/or Reynolds number. Even for cases 6 and 20, where the variation of correction factors is greater than in most cases, it still assumes a value that ultimately does not have a significant impact on efficiency prediction. From an overall point of view, an average variation of approximately 0.05% for corrective factors is intuitively insignificant. For prototype geometry, it is noticeable that the variation of these parameters does not affect the final diameter of the prototype at all.

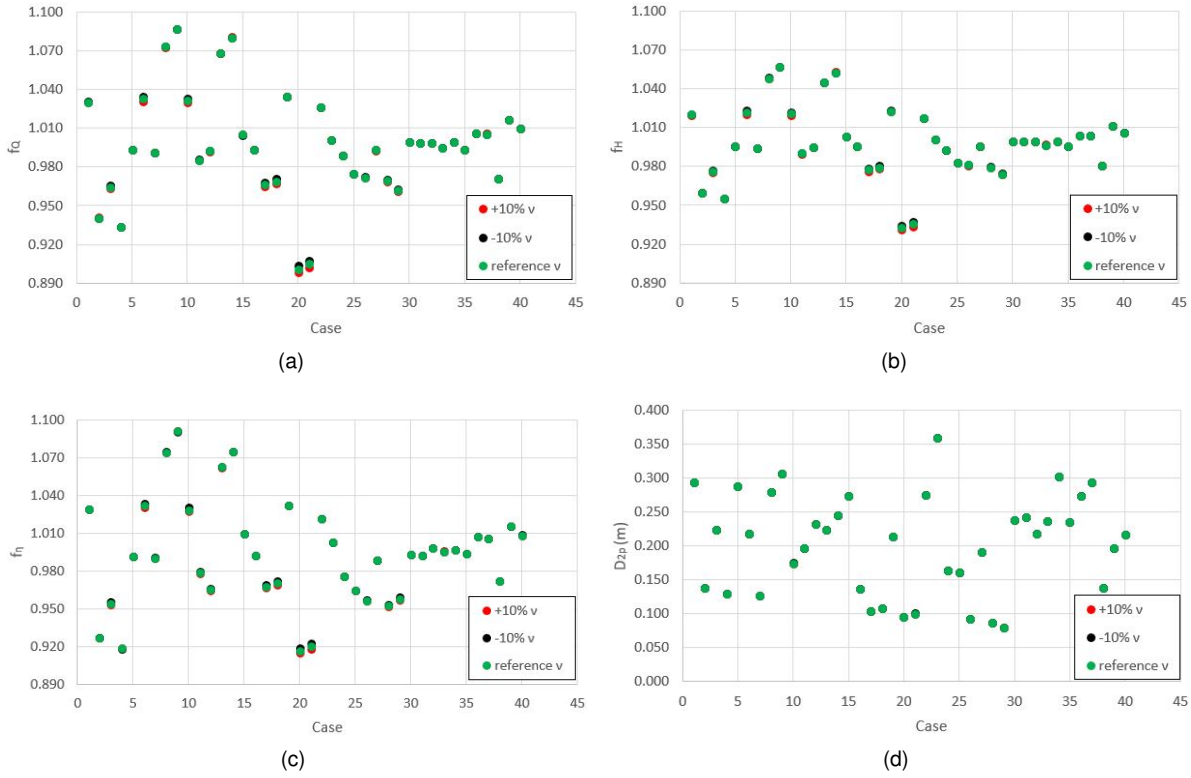

Figure 7.17: Correction factors and prototype diameter variation with viscosity. (a) flow rate factor f_Q variation, (b) head factor f_H variation, (c) efficiency factor f_η variation, (d) prototype diameter D_{2p} variation.

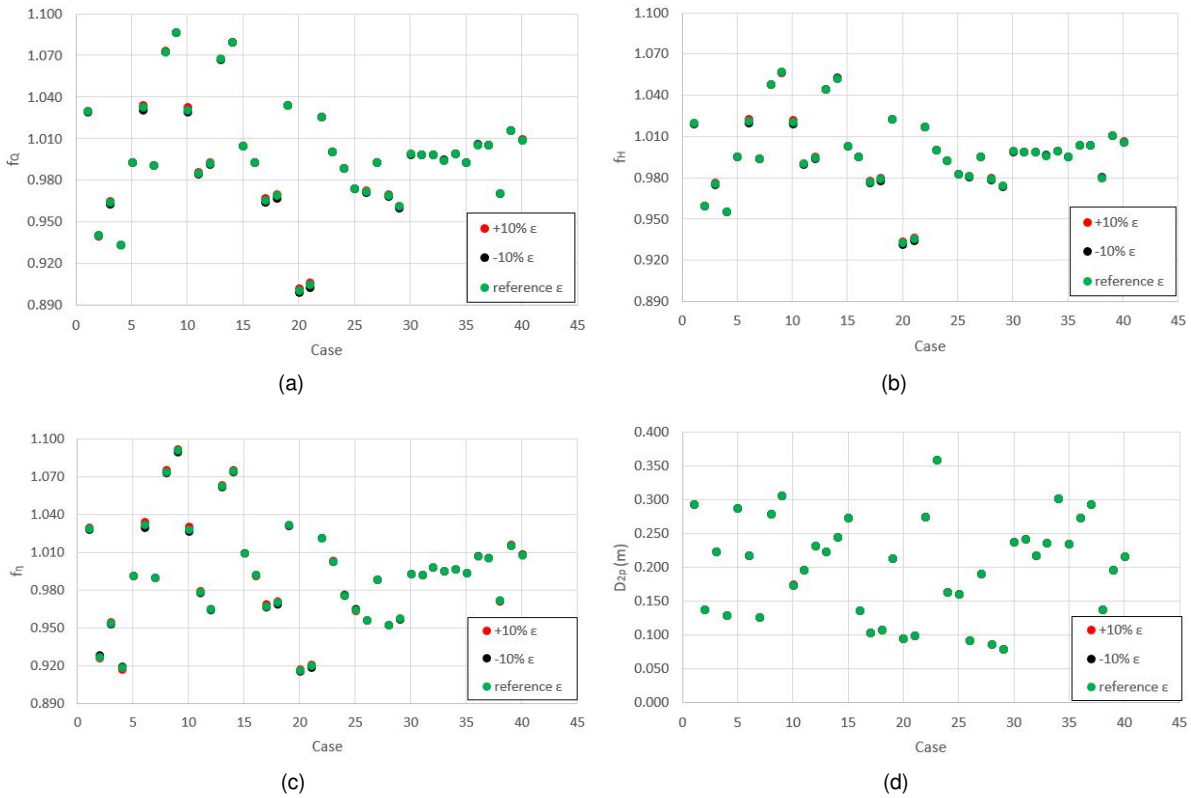

Figure 7.18: Correction factors and prototype diameter variation with roughness. (a) flow rate factor f_Q variation, (b) head factor f_H variation, (c) efficiency factor f_η variation, (d) prototype diameter D_{2p} variation.

Chapter 8

Application of the numerical model to real-life micro-hydropower plants

One of the main objectives of this work is to enable the a priori study of the economic viability of a micro-hydropower system based on the use of a pump working as a turbine for power generation. However, it is essential to understand how the numerical model and its methodology presented in Chapter 7 behave when applied to such systems.

After an extensive research into currently operating micro-hydropower systems, it has only been possible to present two cases with all the information needed to apply the numerical model. As a consequence, this chapter analyzes the application of the numerical model to those two systems and, later, compare the theoretical and experimental results of the PATs efficiencies.

It should be noted that in the literature very little information is available regarding micro-hydropower systems. You can easily find articles or even websites that provide a list with the name and power of several hydro generation systems, see for example [94], [95] and [96]. However, there is a large gap between knowing that a certain hydropower system exists and finding data on the characteristics of that particular system. Whereas, for high power systems information is in most of the cases readily available in the literature, systems with low power or close to 100 kW seem to be of an importance that does not justify (or even remember) the literary publication of such project.

Still, several emails were sent by the author of this thesis to various entities (embassies, researchers and companies) in order to understand if they could help in the search for information or even forward the email to someone more qualified to answer. However, these e-mails would either not be answered or the answer would end up indicating websites that were already encountered. The following work also seizes to suggest the update and optimization of Mr. Jurge Klup's website *Hydro4Africa* that has so much potential for future research in the area of water generation but is so sadly stalled, see [94].

8.1 Waterval's micro-hydropower system, 13kW

8.1.1 System description

The 13kW hydropower system is located on a farm, just north of the town Porteville in Western Cape, South Africa. Through a project developed by [97] from the university of Stellenbosch, the owner of the farm uses the energy produced by the system for self consumption. Despite being connected to the grid, the owner does not inject energy into the grid once the distributor is not seeking for any net metering agreements at the moment.

In the channel of Assegaaibos River, a diversion wire diverts water for the hydroeletric production of energy. A constant flow is then maintained and conveyed along a conduit from the diversion wire at a certain height to the powerhouse at a lower level. The powerhouse contains a PAT coupled to a generator and all the necessary control and protection equipment. In this way, the kinetic energy of the water is transferred to the turbine in the form of mechanical energy, which in turn is transformed into electrical energy in the generator. Subsequently, this energy is sent to the point of use via a transmission line. The water that flowed across the turbine is then expelled from the system back into the river through the tailrace, and thus no water is consumed within the system. In case the water pressure surpasses a particular value, a pressure relief valve opens and lets the water flow through the bypass pipe. Additionally, this bypass line is also useful to avoid water hammer problems that could occur. Fig. 8.1 represents the global scheme of the hydropower system and also details its hydraulic system.

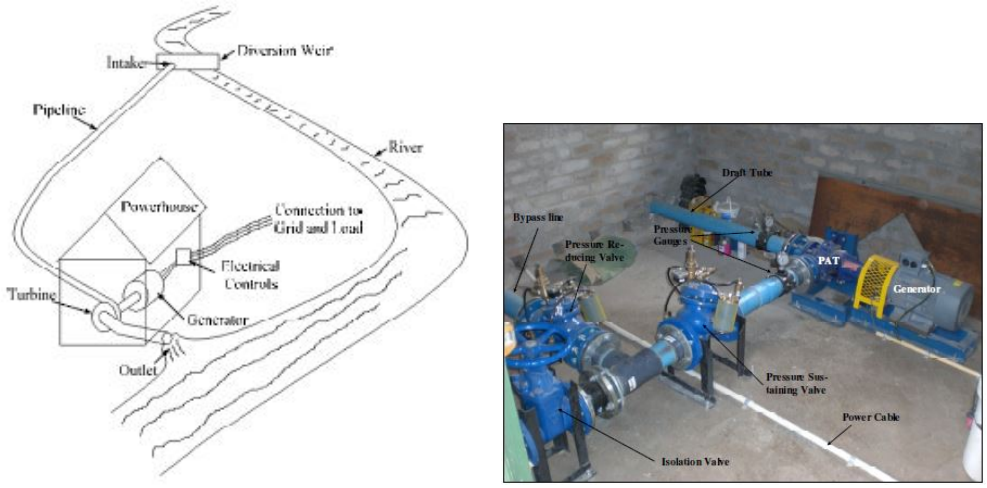

(a) (b)

Figure 8.1: (a) System scheme. (b) Power house [97].

8.1.2 Application of the numerical model

To apply the numerical model to a micro-hydropower system, it is necessary to understand which PATs in the PAT database can correlate with the PAT used in the real case. This is done by using the list of 57 PATs formulated in this work and locating the real case in this list according to its specific velocity

Ω. From the correlation rules[1] of PAT's listed in chapter 6.1, it is determined which cases can correlate with the real case. The case that best approximates the real case is chosen. In addition to the PAT correlation rules, it should be taken into account that a case whose impeller diameter is known should be preferred over a case that does not discriminate its PAT diameter (even if the specific speed of the real case is closer to the specific speed of the PAT with unknown diameter). See Fig. 8.2 which shows the location of Waterval's case in the 57 PATs list.

2nd closest with a known diameter.

Closest, but with an unkown diameter.

Ω	PUMP	Category	P_{total} (kW)	D_2 (m)
0.4030	STRA043	End-suction/volute (radial flow)	33.4	0.334
0.4082	APFE060	double-suction	54.7	0.350
0.4270	HIDR044	End-suction/volute (radial flow)	83.7	0.356
0.4300	JYOT054	End-suction/volute (radial flow)	7.5	n/a
0.4442	**Waterval**	**End-suction/volute (radial flow)**	**13.0**	**0.169**
0.4693	THOR090	double-suction	15.7	0.216
0.4817	MIYA079	double-suction	659.5	0.350
0.4842	WILL047	submersible (radial flow)	7.4	0.184
0.4933	STRU051	End-suction/volute (radial flow)	0.0	n/a
0.4989	THOM062	End-suction/volute (radial flow)	1.1	n/a

Figure 8.2: Waterval hydropower system location on the PAT database.

Waterval PAT can correlate with STRA043, HYDR044, JYOT054, STRU051 and THOM062 PATs[2]. Of these five PATs, the one that best approximates the specific speed of the real case is JYOT054. However, as its diameter is not known, HYDR044 PAT with a diameter of 0.356 m is subsequently considered to correlate best with Waterval's PAT.

In the evaluative context of the numerical model in real systems, it is important to understand what is the definition of model, prototype and resembling prototype. Since the resembling prototype is easily interpreted as the experimental system, that is, one that allows to evaluate the accuracy of the efficiency prediction, it is natural to associate the resembling prototype to the real case PAT (Waterval's PAT). As for the prototype, it is often defined as the theoretical system that comes from the base system, also known as the model. Therefore, the model will be associated with HYDR044 PAT while the prototype corresponds to a PAT geometrically similar to HYDR044, but with a power and rotational speed equal to Waterval's PAT, Fig. 8.3.

MODEL	HIDR044		PROTOTYPE			REAL	Waterval	
Q_M	109.10	[l/s]	P_a	13.03	[kW]	Q_{real}	24	[l/s]
H_M	78.24	[m]	N_a	3080	[rpm]	H_{real}	55.35	[m]
N_M	1800	[rpm]	$D_{2a,initial}$	0.178	[m]	N_{real}	3080	[rpm]
D_{2M}	0.356	[m]	$Q_{a,initial}$	23.25	[l/s]	$D_{2a,real}$	0.169	[m]
Eff_M	76.90%		$H_{a,initial}$	57.13	[m]	$P_{avai,real}$	13.032	[kW]
P_M	83.74	[kW]				Eff_{real}	73.00%	
w_M	188.50	[rad/s]	w_a	322.54	[rad/s]	$w_{a,real}$	322.54	[rad/s]
f_q	1	entries	$f_{q,a}$	1	entries	$f_{q,real}$	1	entries
$U_{2,M}$	33.55	[m/s]	$U_{2,a}$	28.67	[m/s]	$U_{2,a}$	n/a	[m/s]
$z_{st,M}$	1	stages	$z_{st,a}$	1	stages	$z_{st,a}$	1	stages
n_q	22.60		$n_{q,a}$	22.60		$n_{q,real}$	23.51	
Ω_M	0.42696		Ω_a	0.42696		Ω_{real}	0.4442	

Figure 8.3: Model, prototype and resembling prototype characteristics of Waterval's case.

The application of the numerical model is carried on and, at the end, Fif. 8.4 shows the results of

[1] Remember that in the correlation of two PATs the difference between specific speeds cannot exceed the value of 0.05 and its category must be the same.

[2] Notice that the other PATs presented in Fig. 8.2 do not have the same category as Waterval's PAT.

the efficiency prediction for the Waterval's hydropower system. Notice that, for efficiency comparison between the prototype and the resembling prototype, the trendlines polynomial degrees follow the same reasoning applied in sub-section 7.2. As such, in this case, a third and fourth degrees are used to define the flow rate and head trendlines.

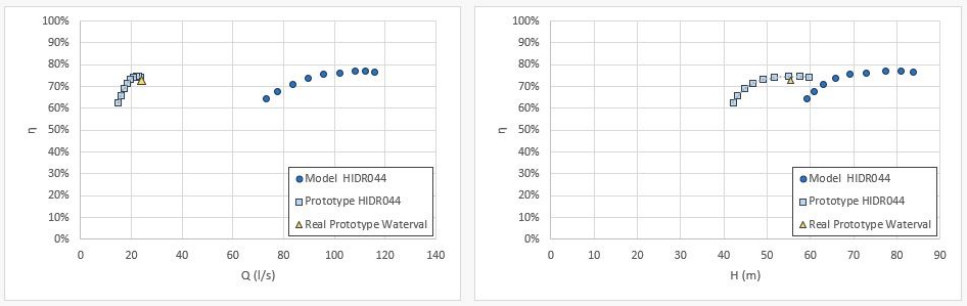

Figure 8.4: Flow rate and head efficiency curves for Waterval's case.

As verified in Fig. 8.4, the prediction presents an extremely high level of success once the absolute and relative errors for both the flow rate and head efficiency curves, listed in Table 8.1, are satisfyingly below the error ranges established for PAT efficiency prediction. As for the prototype diameter, an 8.7 mm difference is also a satisfying result once it is considerably below the 23.8 mm average difference.

		Total Operating Range	±10% BEP Adjusted Range	Waterval's Error
Flow Rate	$\Delta\eta_{abs}$	4.9% - 15.8%	8.1% - 10.3%	1.2%
	$\Delta\eta_{rel}$	7.7% - 49.7%	11.6% - 14.8%	1.7%
Head	$\Delta\eta_{abs}$	4.6% - 22.9%	7.9% - 9.9%	1.6%
	$\Delta\eta_{rel}$	7.5% - 138.8%	10.8% - 13.7%	2.2%

Table 8.1: Comparison between Waterval's error and the established error ranges for efficiency prediction.

8.2 Teuteberg's micro-hydropower system, 117kW

8.2.1 System description

Located on the South Coast of South Africa, the Roman Bay Sea Farm is one of the three well-known Aqunion's businesses in the country that focus its attention on abalone aquaculture. The facility is designed to hold this marine snail in the hatchery throughout its breeding, larvae, settlement and weaning stages where some water is cycled. Afterwards, it is transferred to growing blocks until it reaches marketable size (being this the stage where most of the water is consumed), [98].

The water used in the farm comes from the ocean with the support of four pumps (three manufactured by Rapid Allweine and one by KSB) and is stored in holding tanks for future consumption. Whenever necessary, these tanks release the water into the system and, after its distribution through all the processes of the farm, it returns to the ocean by means of a conduct. Between the penstock and the tailrace (upper and lower conducts, respectively), the water enters a tailing pond in order to separate the debris from the fluid. Later, it is directed to the pump shed where part of its kinetic energy is transformed into mechanical energy through the rotation of a PAT. At the discharge process, this PAT is direct coupled to

the KSB pump replacing the motor that was previously attached to it. In this way, the farm is taking advantage of the waste water that would once be discharged directly to the sea. Additionally, it is important to bare in mind that the discharge pipe must be placed significantly away from the inlet pipe so that the water used previously in the farm is not pumped back in. See Fig. 8.5 that illustrates the Roman Bay Sea Farm hydropower system sceme.

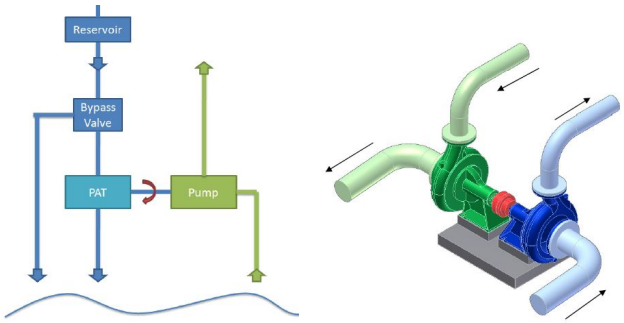

(a) (b)

Figure 8.5: (a) System scheme. (b) PAT and pump coupling [98].

8.2.2 Application of the numerical model

Contrary to the previous case, the specific speed of Teuteberg's hydroelectric system (Ω = 0.9612) exceeds the specific speed restriction defined in this thesis, $\Delta\Omega$. Such fact would imply the exclusion of this case. However, since there are very few micro hydropower systems that can fully test the validity of the numerical model and, as this particular one only exceeds the specific speed by 0.009 (0.9612 - 0.9022 = 0.0590), it has still been considered as valid the application of the numerical model to this case. The results in Figure 8.6 show that the resembling prototype corresponding to Teuteberg's PAT is necessarily correlated with the model given by PAT ENGE122. Similarly to each case, the prototype is characterized by a PAT with geometry similar to ENGE122, but with a power and rotational speed equal to Teuteberg's PAT, see Fig. 8.6. Although this PAT is outside the ranges of the case, it can still be found, in the PAT's database used in this study, a PAT that it relatable with the one of this real-life example. The difference in specific speeds of each PAT exceeds a little the limit considered.

MODEL	ENGE122		PROTOTYPE			REAL	Teutberg	
QM	55.00	[l/s]	Pa	117.33	[kW]	Qreal	520	[l/s]
HM	11.24	[m]	Na	741	[rpm]	Hreal	23	[m]
NM	1250	[rpm]	D2a,initial	0.458	[m]	Nreal	741	[rpm]
D2M	0.185	[m]	Qa,initial	494.31	[l/s]	D2a,real	0.518	[m]
EffM	74.40%		Ha,initial	24.20	[m]	Pavai,real	117.328	[kW]
PM	6.06	[kW]				Effreal	87.00%	
wM	130.90	[rad/s]	wa	77.60	[rad/s]	wa,real	77.60	[rad/s]
fq	1	entries	fq,a	1	entries	fq,real	1	entries
U2,M	12.11	[m/s]	U2,a	17.76	[m/s]	U2,a	20.10	[m/s]
zst,M	1	stages	zst,a	1	stages	zst,a	1	stages
nq	47.75		nq,a	47.75		nq,real	50.88	
ΩM	0.90218		Ωa	0.90218		Ωreal	0.9612	

Figure 8.6: Model, prototype and resembling prototype characteristics of Teuteberg's case.

The application of the numerical model results in the light blue efficiency curves presented in Fig. 8.7 below. The trendlines used to represent the efficiency curves behavior have polynomial degrees based

on the upper group of PATs (fourth and sixth degrees for the flow rate and head trendlines, respectively).

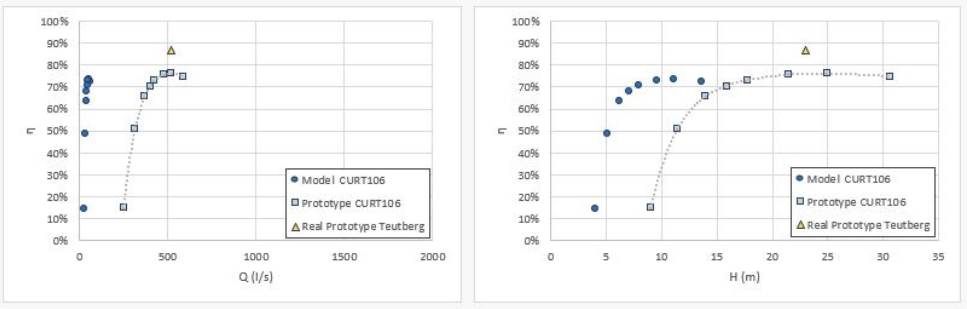

Figure 8.7: Flow rate and head efficiency curves for Teuteberg's case.

Results of Figure 8.4 indicate that the efficiency prediction of the Teuteberg's hydropower system does not exhibit the same quality as in the Waterval's case. For both efficiency curves, Teuteberg's theoretical point of operation has an absolute and relative error of approximately 10% and 12.5%, respectively. Although it is verified a significant absolute error, its importance loses value when associated with a moderately satisfactory relative error. The estimated prototype diameter has a relatively high absolute deviation, about 57 mm (0.518 - 0.461). This indicates that the geometry of ENGE122 does not match successfully Teuteberg's PAT geometry. This naturally leads to higher error associated with the efficiency prediction. Nevertheless, for a case that stands out of the valid specific speed range, the efficiency prediction showed up being quiet acceptable, as shown in Table 8.2 that compares the error associated with Teuteberg's efficiency prediction and the overall error ranges.

		Total Operating Range	$\pm$10% BEP Adjusted Range	Waterval's Error
Flow Rate	$\Delta\eta_{abs}$	4.9% - 15.8%	8.1% - 10.3%	10.7%
	$\Delta\eta_{rel}$	7.7% - 49.7%	11.6% - 14.8%	12.4%
Head	$\Delta\eta_{abs}$	4.6% - 22.9%	7.9% - 9.9%	10.8%
	$\Delta\eta_{rel}$	7.5% - 138.8%	10.8% - 13.7%	12.4%

Table 8.2: Comparison between Teuteberg's error and the established error ranges for efficiency prediction.

Chapter 9

Conclusions

In order to reflect about any problems that may exist in the application of the numerical model, it should be noted the possibility of the assumption of similar geometry being invalid and what implications this has in the prediction of efficiencies. Recall the assumption that pumps with equal dimension coefficients have similar geometries. In fact, *specific speed provides only a rough indication concerning the hydraulic features, configuration and impeller shape of a pump. Depending on the application, a pump with given data N, Q_{opt} and H_{opt} – consequently with a given specific speed – can be equipped with impellers of quite different shapes*, [16]. For example, sewage pumps are usually composed by an impeller outlet two times larger than impeller outlets for non-clogging pumps with similar specific speeds. In addition, based on the suction capability, the ratio between the impeller inlet and outlet might vary significantly for a given specific speed as well. In this work, there were cases with similar and dissimilar diameters. Taking into account that the latest are associated with higher errors, it is up to the user to decide whether or not these errors are acceptable, for example, in the preliminary economic study of an hydropower system.

When it comes to the extrapolation methodology developed in this work, it is brought to a conclusion that, despite having positive influence in the error ranges estimation, the payback fall short when compared to the amount of work invested in the extrapolating process (recall Table 7.7).

9.1 Achievements

With the conclusion of this work, it is imperative to realize the global errors associated with the prediction of PAT efficiency curves. Apart from Table 7.7, it is still important to mature the following characteristics of the efficiency curves: with absolute errors varying between approximately 5 % and 20 %, it is expected that both prototype efficiency curves (i.e. flow rate and head curves) exhibit different shapes when compared to the resembling prototype curves, but at least present an area where the efficiency prediction is carried out with success; as for the relative errors, although their average range differs considerably (8%-50% compared to 8%-140% for the flow rate and head curves, respectively) they represent the same meaning in the prediction of efficiencies – their Large-Small wualifier implies

that the prediction uncertainty might be low or high compared to real life efficiency.

In addition to perceiving the precision of the numerical model along with both efficiency curves, it was also possible to draw conclusions regarding their behavior within a specific operating range, more precisely $\pm$10% BEP. It is now known that to the reduction of the operation range corresponds an almost certain reduction of the maximum error (95%). Likewise, it is concluded that the minimum error is likely to increase or remain constant (55% and 41% respectively). Such results allow not only to realize that the error associated with the efficiency prediction improves, but also that the certainty inherent to the error increases and thus, the results naturally become more reliable.

Variations of $\pm$10% of viscosity hardly affect the prediction of efficiency curves. This is a positive outcome because to these variations correspond temperature changes between 5° and 15° C, which naturally occurs in the channel of a river. Therefore, it is known a priori that the temperature variations of the river, did not considerably affect the efficiency of the micro hydropower system.

Although the sample of real cases is reduced, it can be concluded that the prediction of the BEP efficiency was successfully carried out. In one case, the efficiency was predicted with a very satisfying precision, only diverging about 1.5% in both efficiency curves. In the other case, the efficiency deviated a little further from the experimental value. However, it is essential to take into account that the latter case is characterized by a specific speed deviation slightly greater than acceptable limit but, even so, it presents absolute errors just somewhat bigger than those specified for operating points within the range of $\pm$10% of the BEP, see Table 8.2.

In addition, as it was intended to prove, it is now possible to conclude that the specific speed has a significant impact on the efficiency curves of a PAT. In fact, when analyzing the graphics inserted in Appendix A.5, it is easy to see that PATs with higher specific speeds are naturally associated with efficiency curves with higher efficiencies. For the flow rate efficiency curve, there is an efficiency increase with a curve displacement in the direction of increasing dimensionless flow rate. As for the head curve, the efficiency increase is also observed, but in this case the curve displacement occurs in the decreasing direction of the head coefficient.

That said, it is concluded that the SPATEC program satisfactorily forecasts the flow rate and head efficiency curves for pumps operating as turbines.

9.2 Future Work

If, in any way, it is intended to improve the study herein applied, it is always possible to see the source of each used PAT and do a research in order to find geometric characteristics that define it respective impeller. This is often not possible because pump manufacturers do not provide this type of information for reasons of confidentiality. However, this is still a way to strengthen the evaluation of the numerical model.

The absolute error of the flow-dependent efficiency curve does not vary much compared to the absolute error associated with the efficiency curve depending on the head. However, it is important to realize that in the flow curve the impact of the efficiency deviation is lower than in the head curve. In part,

this difference is due to operating points with relative head errors well above the relative flow rate errors. Cases 14, 15, 20, 21 and 22 are cases that have operating points with these characteristics. It would be interesting to remove these cases from the global average of the error and to study the differences of error existing between the efficiency predictions for flow-dependent curves and for head-dependent curves.

As was verified at the beginning of chapter 7.3, the trendline often does not define the behavior of the prototype operating points with the best quality and, as a consequence, the estimated error between the prototype and the resembling prototype not always corresponds to reality. To avoid this situation, the analysis of results would have to be redone, only this time with linear regressions that better define the curve that correlates all the operating points of the prototype.

In an alternative and simplistic way to the situation of the previous paragraph, it is also possible to improve the assessment of absolute and relative errors by redefining the ranges that characterize the trendlines of each prototype. In this way, to the minimum point of the trendline it shall correspond the operating point of the prototype previous to the first operating point of the similar prototype. If there are no prototype operating points before the operating points of the similar prototype, then the minimum point of the prototype is considered as minimum point of the trendline. The same reasoning is naturally applied to the maximum point of the trendline. As a consequence, high degree polynomials with irregular shapes are avoided and the approximation of the trendline with the operating points increases (reflected by the increase of the determination coefficient R^2). Bare in mind that, despite determination coefficients closer to 1, the shape of the prototype efficiency curve might still different from the real curve shape once several operating points were omitted.

The impact that the variation in roughness has on the numerical model must be deepened. By Table 4.3 it is acceptable to think that the walls of the impeller and the diffuser reach values like 100 μm or even higher. The roughness variation of 10% applied in this work is not enough to cover a wider range of the roughnesses that can be seen in PATs and, hence, express in greater detail and caution, the impact that the roughness can really have on the efficiency of a micro hydropower system.

If it proves worthwhile, it might yet be studied the influence of the Reynolds number and roughness for other combinations of $\pm$10% Re and $\pm$10% ε, for example, the case with +10% Re and +10% ε. These combined variations were not studied because it was considered acceptable to assume that these variations result in efficiencies as insignificant as those obtained for the variations studied in this project.

Research for more hydropower systems operating with a PAT and, subsequent application of the numerical model to these particular systems. In this work it is only studied the efficiency curve prediction of two micro hydropower systems. However, it is important to strengthen the quality of the numerical model output when applied to real operating systems. It might me a good example, to start by the Thima village case in Kenya. This hydropower station project, carried by Nottingham Trent University, provides two hundred 10 W light packages to 110 households [99], [100] and [101].

In order to understand the influence that the specific speed has on the results obtained, it is still important to study how the deviation between diameters and errors are correlated with the difference

between the specific speeds of the prototype and the resembling prototype. In other words, understand the behavior of the functions $\Delta D_2 = f(\Delta\Omega)$ and $\Delta\eta = f(\Delta\Omega)$. In addition, it would also be interesting to graphically represent mechanical losses, volume losses and hydraulic losses depending on each of the case groups (i.e. lower, intermediate and upper groups) defined in this work.

Nevertheless, it is also important to mention that the SPATEC program can be optimized so that, by inserting the characteristics and operating points of the model and resembling prototype, the program automatically returns the efficiency curve of the prototype. In this way, the entire iterative process, that once had to be done manually, would be automatically bypassed.

Finally, it is still extremely important to realize that this model can very easily be combined with a predictive model of an induction generator efficiency and, as so, used in the economic study of an hydropower system. In fact, this efficiency prediction and subsequent economic assessment should be studied for different hydropower system capacities so that, altogether, it would be developed a two-dimensional plane as a function of the power and rotational speed, divided according to the price of the system. In this way, the price of an hydropower system would be easily predicted.

Bibliography

[1] F. Birol. World energy outlook 2010. International Energy Agency, 2010. p 736.

[2] C. S. Kuanda, C. Z. Kimambo, and T. K. Nielsen. A technical discussion on microhydropower technology and its turbines. Renewable and Sustainable Energy Reviews, 2014. 35 445-59.

[3] IEA. World energy state. URL `https://www.iea.org/reports/world-energy-outlook-2019`.

[4] I. H. Association, I. C. on Large Dams, I. A. on Hydropower Technologies, P. E. Agency, and C. H. Association. Hydropower and the world's energy future, November 2000.

[5] A. Williams. Pumps as turbines: A user's guide. Intermediate Technology Publications, 1995.

[6] M. Arriaga. Pump as turbine – a pico-hydro alternative in lao people's democratic republic. *Renewable Energy*, 35(5):1109–1115, May 2010.

[7] S. Derakhshan and A. Nourbakhsh. Experimental study of characteristic curves of centrifugal pumps working as turbines in different specific speeds. *Experimental Thermal and Fluid Science*, 32(3):800–807, January 2008.

[8] A. A. Williams, A. Rodrigues, P. Singh, F. Nestmann, and E. Lai. Hydraulic analysis of a pump as a turbine with cfd and experimental data. In Proceedings of the IMechE Seminar, Computational Fluid Dynamics for Fluid Machinery, November 2003.

[9] H. Nautiyal, Varun, and A. Kumar. Reverse running pumps analytical, experimental and computational study: A review. *Renewable and Sustainable Energy Reviews*, 14(7):2059–2067, September 2010.

[10] H. Nautiyal, K. A. Varun, and S. Yadav. Cfd analysis on pumps working as turbines. Hydro Nepal 2010, 2010.

[11] A. Carravetta, G. D. Giudice, O. Fecarotta, and H. M. Ramos. Pat design strategy for energy recovery in water distribution networks by electrical regulation. *Energies*, 6(1):411–424, January 2013.

[12] A. Carravetta, G. D. Giudice, O. Fecarotta, and H. M. Ramos. Pump as turbine (pat) design in water distribution network by system effectiveness. *Water*, 5(3):1211–1225, August 2013.

[13] S. Derakhshan, B. Mohammadi, and A. Nourbakhsh. Efficiency improvement of centrifugal reverse pumps. *Journal of Fluids Engineering*, 131(2):021103 (9 pages), January 2009.

[14] S. R. Natanasabapathi and J. T. Kshirsagar. Pump as turbine—an experience with cfx 5.6, 2004.

[15] J. M. Chapallaz, P. Eichenberger, and G. Fischer. Manual on pumps used as turbines. Friedr Vieweg Sohn Verlagsgesellschaft, Braunschweig; Informatica International, Inc, 1992.

[16] J. F. Gülich. *Centrifugal Pumps*. Springer, 2nd edition, 2010. Chapters 1-3.

[17] L. Shafer. Practical applications for pumps as hydraulic turbines for small scale hydropower. Waterpower '83 Conference, 1983.

[18] D. Thoma. Vorgange beim ausfallen des antriebes von kreiselpumpen, 1931.

[19] C. P. Kittredge. Centrifugal pumps operated under abnormal conditions. Power, June 1931.

[20] J. Sprecher. The hydraulic power storage pumps of the etzel hydro-electric power scheme. Sulzer Technical Review, 1951.

[21] C. Alatorre-Frenk. *COST MINIMISATION IN MICRO-HYDRO SYSTEMS USING PUMPS-AS-TURBINES*. PhD thesis, University of Warwick, February 1994.

[22] W. Meier. Pompes-turbines. Bulletin Escher-Wyss, 1962. 2.

[23] G. Krivchenko. Hydraulic machines. turbines and pumps, 1986.

[24] J. Raabe. Optimization of pump turbines. Journal of the Energy Division, 1981.

[25] K. Sharma. Small hydro electric projects. use of centrifugal pumps as turbines, 1984.

[26] A. J. Stepanoff. Centrifugal and axial flow pumps. theory, design and application, 1957. 2nd ed.

[27] R. Strub. Investigations and experiments on pumpturbines. Sulzer Technical Review, 1959. 2.

[28] A. Williams. Pumps as turbines used with induction generators for stand-alone micro-hydroelectric power plants. PhDthesis, 1992.

[29] E. Schmiedl. Serien-kreiselpumpen im turbinenbetrieb. Pumpentagung Karlsruhe '88, 1988. Section A6.

[30] A. Engeda and M. Rautenberg. Comparisons of the performance of hydraulic turbines and reversible pumps for small-hydro applications. 5th International Symposium on Hydro Power Fluid Machinery, 1988. FED -68.

[31] J. D. Lawrence. Small-scale hydro: the use of pumps as turbines. Waterpower '79, 1979.

[32] P. N. Garay. Using pumps as hydroturbines. Hydro Review, 1990. 9, 5.

[33] A. A. Grant and J. M. Barn. Pump turbine - the economic answer. 1st International Conference on Small Hydro, IWPDC, 1984.

[34] F. Hochreutiner. Centrale hydroélectrique de tannuwald. Hidroenergia 1991 Conference Proceedings, 2nd International Conference & Exhibition, 1991.

[35] A. A. Williams. Overseas visit report, 1991. Pakistan (unpublished).

[36] G. Ventrone and G. Navarro. Utilizzazione dell'energia idrica su piccola scala: pompa come turbina. L'Energia Elettrica, 1982.

[37] R. N. Torbin, S. D. Lautenschlaeger, and E. D. Thimons. Conference "Water for Resource Development", 1984.

[38] Fraser and Associates. Modular small hydro configuration. Report Nyserda, 1981. 81-16.

[39] P. Hergt, P. Krieger, and S. Thommes. Die strömungstechnischen eigenschaften von kreiselpumpen im turbinenbetrieb. Pumpentagung Karisruhe, 1984. Section Cl.

[40] A. J. Semple and W. Wong. The application of hydraulic power recovery turbines in process plant. Second European Congress on Fluid Machinery for the Oil, Petrochemical and Related Industries (The Hague), 1984. C35.227-34.

[41] W. Wong. The application of centrifugal pumps for power generation. 10th International Conference of the BPMA, 1987.

[42] A. A. Inc. Small hydroplant development program, 1980.

[43] A. Kumar and O. Thapar. Integrated small hydro energy development. Conference "Water for Resource Development", 1984.

[44] K. Mikus. Erfahrungen mit kreiselpumpenanlagen zur energie-rückgewinnung aus dem trinkwassersystem. GWF-Wasser/ Abwasser, 1983.

[45] V. Schnitzer. Water energy recovery from existing water supply systems with pumps as turbines (pat). Hydro 92. Fifth International Conference on Small Hydro, 1992.

[46] E. Wilson and R. Potts. Hydro development at errwood reservoir using a centrifugal pump as turbine. Hydro 92. Fifth International Conference on Small Hydro, 1992.

[47] R. Apfelbacher and F. Etzold. nergy-saving, shockfree throttling with the aid of a reverse running centrifugal pump. KSB Technische Berichte, 1988. 24e.

[48] S. Yedidiah. Application of centrifugal pumps for power recovery purposes. Performance Characteristics of Hydraulic Turbines and Pumps, 1983.

[49] E. D. Vries. Dutch activities on hydropower. Hidroenergia 1991 Conference Proceedings, 2nd International Conference & Exhibition, 1991.

[50] W. Duncan. Proposed use of existing pumps for generation during spring runoff. 2nd Symposium on Small Hydropower Fluid Machinery, 1982.

[51] C. Laux. Reversible multistage pumps as energy recovery turbines in oil supply systems. Sulzer Technical Review, 1980.

[52] G. Naber and K. Hausch. Reversible pumpturbinen in trinkwasserfernleitungen. Wasserwirtschaft, 1987.

[53] V. Schnitzer. Neue perspektiven zur nutzung kleiner und kleinster wasserkräfte durch pumpen in turbinenbetrieb. Wasserwirtschaft, 1985.

[54] L. L. Shafer. Pumps as power turbines. Mechanical Engineering, 1982.

[55] E. Kasperowski. Das bewässerungspumpwerk tjurug west in indonesien. KSB Technische Berichte, 1966. 11.

[56] C. Priesnitz. Einsatzmöglichkeiten von rückwärtslaufenden standardkreiselpumpen als turbinen zur energie-rückgewinnung. Information Pumpen und Verdichter, 1987. 1.

[57] I. Taylor. Some installed power recovery turbines found unusable due to missconceptions of process and performance. Performance Characteristics of Hydraulic Turbines and Pumps, 1983.

[58] W. Bolliger and F. Gajewski. Energierückgewinnung mit pumpen im turbinenbetrieb bei expansion von gasbeladenen flussigkeiten. Pumpentagung Karlsruhe, 1984. Seccion C1.

[59] E. Daffner and W. Dettinger. Hydraulische energierückgewinnung aus fluids bei hohen druckgefallen. Pumpentagung Karlsruhe, 1984. Sektion Cl.

[60] S. Gopalakrishnan. ower recovery turbines for the process industry. 3rd International Pump Symposium, Texas A & M University, 1986.

[61] J. Gulich. Energy recovery from expansion of two-phase mixtures using pumps in the turbine mode. Sulzer Technical Review, 1981. 3.

[62] C. Hamkins, H.-O. Jeske, R. Apfelbacher, and . Schuster. Pumps as energy recovery turbines with two phase flow. Pumping Machinery. FED-81.

[63] C. Hamkins, H.-O. Jeske, R. Apfelbacher, and . Schuster. Performance testing of energy recovery turbines with two phase flow under actual plant conditions. Seminar The Performance Testing of Fluid Machinery, 1989.

[64] P. Kamath and W. Swift. Two-phase performance of scale models of a primary coolant pump. NP2578, Final Report, 1982.

[65] W. Kennedy, M. Jacob, J. Whitehouse, J. Fishbum, and G. Kanupka. Pump thvo-phase performance program. NP-1556, 1980.

[66] L. Nelik and P. Cooper. Performance of multi-stage radial-inflow hydraulic power recovery turbines. ASME paper, 1984. 84-WA/FM-4.

[67] D. Olson. Single and two-phase performance characteristics of the mod-i semiscale pump under steady state and transient fluid conditions. ANCR -1165, 1974. ANCR.

[68] R. Winks. One-third scale air-water pump program: Test program and pump performance. NP -135, 1977.

[69] W. Pumps. Centrifugal pumps used as turbines. World Pumps, April 1985.

[70] A. Salaspini. Picking pumps for ro plant. World Water, 1985.

[71] A. F. O. Falcão. *Mecânica dos Fluidos II*. 1st edition, 2015.

[72] M. O. P. Singh. Mechanical seal and gland packing. URL `https://pt.slideshare.net/om_singh/mechanical-seal-vs-gland-packing`.

[73] SKF. Deep groove ball bearings, . URL `https://www.skf.com/us/products/rolling-bearings/ball-bearings/deep-groove-ball-bearings`.

[74] SKF. Radial spherical plain bearings, . URL `https://www.skf.com/us/products/plain-bearings/bushings-thrust-washers-strips/principles/selecting-bearing-size/calculation-example/productid-GE%204%20C`.

[75] A. F. O. Falcão. *Turbomáquinas*. 1st edition, 2017. Chapter 7.

[76] G. G. Iraktar and A. U. Gandigude. A review on static analysis and material optimization using fea of centrifugal pump impeller. *IJARIIT*, 2017.

[77] T. Liebner, D. Cowan, and S. Bradshaw. The influence of impeller wear ring geometry on suction performance. 2016.

[78] H. P. Bloch. Pump wisdom: Problem solving for operators and specialists. 2011.

[79] J. Feng, F.-K. Benra, and X. Luo. Experimental investigation on turbulence fields in a radial diffuser pump using piv technique. Research article, Xi'an University of Technology and University of Duisburg-Essen, June 2014. Corresponding author: fengjianjunxaut@163.com.

[80] O. Babayigit, O. Kocaaslan, M. H. Aksoy, K. M. Guleren, and M. Ozgoren. Numerical identification of blade exit angle effect on the performance for a multistage centrifugal pump impeller. *EDP Sciences*, 2015. Corresponding author: obabayigit@selcuk.edu.tr.

[81] J. Nikuradse. Strömungsgesetze in rauhen rohren. VDI Forschungsheft 361, 1933.

[82] H. Grein. Einige bemerkungen über die oberflächenrauheit der benetzten komponenten hydraulischer großmaschinen. Escher Wyss Mitteilungen, 1975. Nr. 1, 34-40.

[83] R. D. Blevins. Applied fluid dynamics handbook. Van Nostrand Reinhold, 1984.

[84] I. E. Idelchick. Handbook of hydraulic resistance. CRC Press, 1994.

[85] H. Schlichting. Grenzschicht-theorie. Braun, 1982.

[86] K. Pantell. Versuche über scheibenreibung. Forsch Ing Wes 16, 1949/50. 97-108.

[87] J. W. Dailey and R. E. Nece. Chamber dimension effects on frictional resistance of enclosed rotating disks. ASME J Basic Engng 82, 1960. 217-232.

[88] J. F. Gülich. Disk friction losses of closed turbomachine impellers. Forsch Ing Wes 68, 2003. 87-97.

[89] D. S. Miller. Internal flow systems. BHRA, 1990.

[90] I. S. Paterson and C. S. Martin. Effect of specific speed on pump characteristics and hydraulic transients in abnormal zones of operation. 12th Symposium of the SHMEC "Hydraulic Machinery in the Energy Related Industries", 1984. 151-72.

[91] D. Cyders and D. Ghasvari. Centrifugal pump performance experiment. URL http://www.hds.bme.hu/~fhegedus/VibrationMonitoring/Ali%20Parhizkar/Refrences/Understanding%20Topic/4880-PumpBackground.pdf?fbclid=IwAR2sxiC4yBw8u5LsJNmm2lLjgxSacF_XriAOsHC_a0ocj13H_afCmEjWiz4.

[92] D. Zariatin and S. K. D. Rahmalina. The performance of pump as turbine with machined impellers. Technical report, Universitas Pancasila and ATMI Cikarang, Jakarta, Indonesia, 2018.

[93] J. F. Gülich. Effect of reynolds-number and surface roughness on the efficiency of centrifugal pumps. *ASME J Fluids Engng*, pages 670–679, 125 (2003) 4,.

[94] W. J. Klunne. Hydro4africa. URL http://hydro4africa.net/HP_database/.

[95] U. N. I. D. Organization. World small hydropower development report 2016. URL http://www.smallhydroworld.org/fileadmin/user_upload/pdf/2016/WSHPDR_2016_full_report.pdf.

[96] M. Binama, W.-T. Su, X.-B. Li, F.-C. Li, and Y. Zhao. Investigation on pump as turbine (pat) selection and performance prediction for micro hydropower schemes: A review. 2nd INTERNATIONAL SYMPOSIUM OF CAVITATION AND MULTIPHASE FLOW, October 2016. Corresponding author: suwentao@hit.edu.cn.

[97] A. C. J. Lombard and M. J. Kamper. Design and implementation of a low cost grid-connected 10 kw hydro power system. Master's thesis, Stellenbosch University, March 2010.

[98] B. H. Teuteberg and W. V. Niekerk. Design of a pump-as-turbine microhydro system for an abalone farm. Technical Report 878, Stellenbosch University, March 2010.

[99] P. Maher. Community pico hydro in sub-saharan africa: Case study 2. *Community Pico Hydro in Sub-Saharan Africa*, 2002.

[100] P. Maher, N. Smith, and A. Williams. Assessment of pico hydro as an option for off-grid electrification in kenya. *Renewable Energy*, 2002.

[101] Mirco-hydroelectric project pico hydro project -thima site.

Appendix A

PAT-related information

A.1 PATs database

Ω	PUMP	Category	Fixed Variable(s)		P_{total} (kW)	D(m)
0.1172	GIDD018	End-suction/volute (radial flow)	N (rpm)	-	17.5	0.200
0.1577	STRA022	End-suction/volute (radial flow)	N (rpm)	-	3.35	0.320
0.1756	WILL026	End-suction/volute (radial flow)	N (rpm)	-	2.06	0.134
0.1799	BUSE024	End-suction/volute (radial flow)	N (rpm)	-	0.05	n/a
0.1993	SENU037	End-suction/volute (radial flow) (semi-open impeller)	N (rpm)	-	0.80	0.101
0.2045	SCHM027	End-suction/volute (radial flow)	N (rpm)	-	2.53	0.250
0.2199	DIED028	End-suction/volute (radial flow)	N (rpm)	-	107.5	0.325
0.2717	KNAP044	double-suction	H(m)	-	17.0	n/a
0.2740	THOR042	double-suction	N (rpm)	-	19.3	0.318
0.2824	SMIT035	double-suction	N (rpm)	-	6.03	0.246
0.2897	KITT038	double-suction	Q (l/s)	-	33.3	0.505
0.2953	GIDD035	End-suction/volute (radial flow)	N (rpm)	-	8.98	0.160
0.3283	YEDI038	End-suction/volute (radial flow)	N (rpm)	-	6.94	0.127
0.3487	LUEN043	End-suction/volute (radial flow)	N (rpm)	-	0.022	n/a
0.3499	LAUX039	End-suction/volute (radial flow)	N (rpm)	-	0.021	n/a
0.3616	SANT050	End-suction/volute (radial flow)	N (rpm)	-	16.3	0.200
0.4030	STRA043	End-suction/volute (radial flow)	N (rpm)	-	33.4	0.334
0.4082	APFE060	double-suction	N (rpm)	-	54.7	0.350
0.4270	HIDR044	End-suction/volute (radial flow)	N (rpm)	-	83.7	0.356
0.4300	JYOT054	End-suction/volute (radial flow)	N (rpm)	-	7.47	n/a
0.4693	THOR090	double-suction	N (rpm)	-	15.7	0.216
0.4817	MIYA079	double-suction	H(m)	-	659.5	0.350

Table A.1 continued from previous page

Ω	PUMP	Category	Fixed Variable(s)		P_{total} (kW)	D (m)
0.4842	WILL047	submersible (radial flow)	None	-	7.39	0.184
0.4933	STRU051	End-suction/volute (radial flow)	N (rpm)	H(m)	0.016	n/a
0.4989	THOM062	End-suction/volute (radial flow)	N (rpm)	Q (l/s)	1.12	n/a
0.5112	ENGE057	End-suction/volute (radial flow)	N (rpm)	-	14.4	0.202
0.5403	MEIE056	End-suction/volute (radial flow) (fixed vanes)	N (rpm)	-	0.010	n/a
0.5748	ALAT068	End-suction/volute (radial flow)	None	-	1.53	0.174
0.5878	KNAP064	End-suction/volute (radial flow)	H(m)	-	200.3	n/a
0.6164	KITT074	End-suction/volute (radial flow) (fixed vanes)	N (rpm)	Q (l/s)	3.08	0.312
0.6390	KNAP063	End-suction/volute (radial flow)	H(m)	-	337.5	0.340
0.6586	STRA081	End-suction/volute (radial flow)	N (rpm)	-	12.2	0.219
0.6799	NELI044	multistage (2 radial flow stages)	N (rpm)	-	24.0	0.284
0.6912	KNAP067	End-suction/volute (radial flow) (double volute)	H(m)	-	305.8	0.340
0.6959	ENGE082	End-suction/volute (radial flow) (semi-open impeller)	N (rpm)	-	4.08	0.219
0.7008	PECK098	End-suction/volute (radial flow)	H(m)	-	4.65	0.273
0.7219	VENT084	End-suction/volute (radial flow)	N (rpm)	-	40.2	0.280
0.7578	GIDD079	End-suction/volute (radial flow)	N (rpm)	-	8.51	0.125
0.7903	DIED088	End-suction/volute (radial flow)	N (rpm)	-	74.9	0.215
0.8890	CURT106	End-suction/volute (radial flow) (with fixed vanes)	N (rpm)	-	9.00	0.177
0.9022	ENGE122	End-suction/volute (radial flow)	N (rpm)	-	6.06	0.185
1.0093	WILL126	submersible (mixed flow)	N (rpm)	-	11.9	0.140
1.0539	MIKU049	multistage (3 radial flow stages)	N (rpm)	-	37.9	0.315
1.1548	YANG123	bowl (mixed flow)	N (rpm)	-	0.016	n/a
1.1596	DIED037	multistage (6 radial flow stages)	N (rpm)	-	3.09	0.180
1.1833	ENGE151	End-suction/volute (radial flow) (semi-open impeller)	N (rpm)	-	23.9	0.224
1.2215	JYOT183	End-suction/volute (mixed flow)	N (rpm)	-	4.70	n/a
1.2402	KENN157	End-suction/volute (mixed flow)	None	-	382.8	n/a
1.6171	HIDR177	bowl (mixed flow)	N (rpm)	-	31.0	n/a
1.8710	MIYA194	bowl (mixed flow)	H(m)	-	96.6	0.409
1.9996	THOM150	multistage (2 radial flow stages)	N (rpm)	-	1175.3	1.372
2.6150	SWAN274	bowl (mixed flow)	Q (l/s)	-	3.09	0.210

Table A.1 continued from previous page

Ω	PUMP	Category	Fixed Variable(s)		P_{total} (kW)	D (m)
2.6359	COOP297	bowl (mixed flow)	N (rpm)	-	225.1	0.686
2.6566	STIR348	bowl (axial flow)	H(m)	-	90.8	n/a
2.8509	COOP346	bowl (mixed flow)	N (rpm)	-	268.0	0.686
3.0956	MIYA348	bowl (axial flow)	H(m)	-	43.4	0.409
4.1554	SWAN496	bowl (axial flow)	Q (l/s)	-	0.274	0.203

Table A.1: List of all 57 PATs organized by specific speed Ω.

A.2 PAT-correlated cases

Case	Ω_M	Ω_p	$\lvert\Delta\Omega\rvert$	Model	Prototype
1	0.117	0.158	0.0410	GIDD018	STRA022
2	0.158	0.176	0.0180	STRA022	WILL026
3	0.158	0.180	0.0220	STRA022	BUSE024
4	0.158	0.199	0.0410	STRA022	SENU037
5	0.158	0.205	0.0470	STRA022	SCHM027
6	0.176	0.180	0.0040	WILL026	BUSE024
7	0.176	0.199	0.0230	WILL026	SENU037
8	0.176	0.205	0.0290	WILL026	SCHM027
9	0.176	0.220	0.0440	WILL026	DIED028
10	0.199	0.180	0.0190	SENU037	BUSE024
11	0.199	0.205	0.0060	SENU037	SCHM027
12	0.199	0.220	0.0210	SENU037	DIED028
13	0.205	0.180	0.0250	SCHM027	BUSE024
14	0.205	0.220	0.0150	SCHM027	DIED028
15	0.220	0.180	0.0400	DIED028	BUSE024
16	0.295	0.328	0.0330	GIDD035	YEDI038
17	0.328	0.349	0.0210	YEDI038	LUEN043
18	0.328	0.350	0.0220	YEDI038	LAUX039
19	0.328	0.362	0.0340	YEDI038	SANT050
20	0.362	0.349	0.0130	SANT050	LUEN043
21	0.362	0.350	0.0120	SANT050	LAUX039
22	0.362	0.403	0.0410	SANT050	STRA043
23	0.403	0.427	0.0240	STRA043	HIDR044
24	0.403	0.430	0.0270	STRA043	JYOT054
25	0.427	0.430	0.0030	HIDR044	JYOT054

Table A.2 continued from previous page

Case	Ω_M	Ω_p	—$\Delta\Omega$—	Model	Prototype
26	0.493	0.511	0.0180	STRU051	ENGE057
27	0.511	0.499	0.0120	ENGE057	THOM062
28	0.511	0.540	0.0290	ENGE057	MEIE056
29	0.540	0.575	0.0350	MEIE056	ALAT068
30	0.639	0.659	0.0195	KNAP063	STRA081
31	0.659	0.696	0.0370	STRA081	ENGE082
32	0.691	0.659	0.0320	KNAP067	STRA081
33	0.691	0.722	0.0310	KNAP067	VENT084
34	0.696	0.722	0.0260	ENGE082	VENT084
35	0.701	0.659	0.0420	PECK098	STRA081
36	0.701	0.696	0.0050	PECK098	ENGE082
37	0.701	0.722	0.0210	PECK098	VENT084
38	0.722	0.758	0.0360	VENT084	GIDD079
39	0.758	0.790	0.0320	GIDD079	DIED088
40	0.889	0.902	0.0130	CURT106	ENGE122

Table A.2: List of the 40 correlated cases.

A.3 PATs personal information

PATs informations provided in the following pages.

PAT	ALAT068
Category:	end-suction/volute (radial flow)
Outlet diameter, D:	0.174 m
Original source:	Alatorre

Turbine-mode BEP			
Q(l/s)	H(m)	N(rpm)	η
17.33	8.99	1200	77.9%

Performance data			
Q(l/s)	H(m)	N(rpm)	η
15.00	6.29	0	0.0%
18.03	8.65	378	31.8%
18.07	8.46	553	46.4%
17.99	8.52	618	51.2%
17.77	8.24	691	57.9%
17.73	8.23	763	63.4%
17.86	8.42	871	69.1%
17.46	8.40	1026	77.1%
17.29	8.57	1104	78.3%
17.24	8.64	1134	78.5%
17.06	8.59	1167	78.6%
16.64	8.80	1234	77.8%
16.38	8.76	1302	76.2%
16.04	9.00	1377	73.4%
15.87	9.76	1508	68.1%
14.81	9.86	1581	61.9%
14.12	10.36	1722	52.0%
13.61	10.58	1756	44.4%
11.00	10.58	1823	0.0%

PAT	BUSE024
Category:	end-suction/volute (radial flow)
Outlet diameter, D:	n/a
Original source:	Buse81

Turbine-mode BEP			
Q(l/s)	H(m)	N(rpm)	η
2.10	2.41	401.6	56.0%

Performance data			
Q(l/s)	H(m)	N(rpm)	η
2.29	2.79	401.6	55.9%
2.19	5.58	401.6	56.2%
2.00	2.22	401.6	56.6%
1.80	1.91	401.6	55.2%
1.60	1.63	401.6	51.0%
1.40	1.38	401.6	44.4%
1.20	1.19	401.6	35.8%
1.01	1.02	401.6	23.9%
0.81	0.92	401.6	10.5%
0.71	0.88	401.6	0.0%

PAT	CURT106
Category:	end-suction/volute (radial flow)
Sub-category:	(fixed vanes)
Outlet diameter, D:	0.177 m
Original source:	Curtis83

Turbine-mode BEP			
Q(l/s)	H(m)	N(rpm)	η
47.30	19.40	2000	73.0%

Performance data			
Q(l/s)	H(m)	N(rpm)	η
171.50	305.90	2000	25.5%
151.20	228.80	2000	29.1%
133.30	176.10	2000	32.8%
119.40	137.40	2000	36.4%
104.20	99.90	2000	41.3%
85.70	66.10	2000	49.7%
69.60	41.80	2000	60.3%
63.00	34.40	2000	64.8%
54.40	25.60	2000	70.3%
49.30	20.90	2000	72.9%
45.60	18.00	2000	73.7%
41.50	15.50	2000	72.5%
37.50	13.20	2000	67.8%
33.40	11.00	2000	57.4%
30.60	9.70	2000	48.1%
29.30	9.50	2000	39.1%
26.00	8.10	2000	23.7%
23.30	7.90	2000	0.0%

Table A.3: PATs unique information (1/10).

PAT	DIED028
Category:	end-suction/volute (radial flow)
Outlet diameter, D:	0.325 m
Original source:	Diedrich57

Turbine-mode BEP			
Q(l/s)	H(m)	N(rpm)	η
49.53	221.2	3000	68.8%

Performance data			
Q(l/s)	H(m)	N(rpm)	η
43.44	146.40	0	0.0%
52.81	243.30	3000	67.7%
50.05	224.90	3000	68.7%
47.26	207.20	3000	68.9%
44.48	192.70	3000	68.0%
41.69	179.90	3000	66.6%
38.91	169.60	3000	64.7%
36.12	160.40	3000	61.7%
33.40	152.90	3000	57.0%
30.66	146.60	3000	50.5%
27.89	140.70	3000	42.2%
25.08	135.40	3000	31.5%
22.28	130.60	3000	19.2%
19.52	126.50	3000	5.4%
18.56	125.30	3000	0.0%

PAT	DIED088
Category:	end-suction/volute (radial flow)
Outlet diameter, D:	0.215 m
Original source:	Diedrich57

Turbine-mode BEP			
Q(l/s)	H(m)	N(rpm)	η
114.00	66.96	2900	83.4%

Performance data			
Q(l/s)	H(m)	N(rpm)	η
102.00	68.99	0	0.0%
127.90	82.11	2900	83.1%
122.40	75.99	2900	83.5%
116.70	69.70	2900	83.5%
111.20	64.24	2900	83.2%
105.60	59.02	2900	82.5%
100.10	54.18	2900	81.3%
94.60	49.79	2900	79.4%
89.00	45.79	2900	76.7%
83.50	42.29	2900	72.8%
77.90	38.96	2900	67.5%
72.30	35.97	2900	60.0%
66.70	33.19	2900	50.3%
61.20	30.87	2900	37.4%
55.80	28.72	2900	20.7%
51.00	27.01	2900	0.0%

PAT	ENGE057
Category:	end-suction/volute (radial flow)
Outlet diameter, D:	0.262 m
Original source:	Engeda86

Turbine-mode BEP			
Q(l/s)	H(m)	N(rpm)	η
51.48	28.60	1475	82.1%

Performance data			
Q(l/s)	H(m)	N(rpm)	η
62.25	40.89	1475	80.0%
55.79	32.41	1475	80.9%
46.12	24.05	1475	79.6%
36.16	18.91	1475	62.7%
28.12	16.17	1475	38.6%
21.57	14.73	1475	6.9%

Table A.4: PATs unique information (2/10).

PAT	ENGE082
Category:	end-suction/volute (radial flow)
Sub-category:	(semi-open impeller)
Outlet diameter, D:	0.219 m
Original source:	Engeda86

Turbine-mode BEP			
Q(l/s)	H(m)	N(rpm)	η
40.51	10.27	1050	82.0%

Performance data			
Q(l/s)	H(m)	N(rpm)	η
49.26	14.12	1050	79.1%
44.78	12.10	1050	81.1%
42.39	11.02	1050	81.8%
38.02	9.38	1050	81.9%
34.60	8.19	1050	80.0%
30.93	6.99	1050	75.6%
27.55	6.11	1050	69.6%
23.67	5.36	1050	55.2%

PAT	ENGE122
Category:	end-suction/volute (radial flow)
Outlet diameter, D:	0.185 m
Original source:	Engeda86

Turbine-mode BEP			
Q(l/s)	H(m)	N(rpm)	η
55.00	11.24	1250	74.4%

Performance data			
Q(l/s)	H(m)	N(rpm)	η
61.50	13.64	1250	72.4%
54.45	11.13	1250	73.7%
50.04	9.59	1250	73.2%
44.65	7.90	1250	70.8%
41.81	7.11	1250	68.1%
38.32	6.20	1250	63.5%
32.90	5.09	1250	49.0%
26.27	4.01	1250	14.6%

PAT	GIDD018
Category:	end-suction/volute (radial flow)
Outlet diameter, D:	0.200 m
Original source:	Giddens91

Turbine-mode BEP			
Q(l/s)	H(m)	N(rpm)	η
10.07	177.10	3000	43.5%

Performance data			
Q(l/s)	H(m)	N(rpm)	η
10.51	188.90	3000	43.1%
10.20	181.70	3000	43.4%
9.79	169.20	3000	43.0%
9.30	157.40	3000	43.5%
8.78	146.10	3000	43.3%
8.48	136.30	3000	42.2%

Table A.5: PATs unique information (3/10).

PAT	GIDD035
Category:	end-suction/volute (radial flow)
Outlet diameter, D:	0.160 m
Original source:	Giddens91

Turbine-mode BEP			
Q(l/s)	H(m)	N(rpm)	η
14.14	64.74	3000	69.2%

Performance data			
Q(l/s)	H(m)	N(rpm)	η
16.59	80.16	3000	68.2%
15.80	74.51	3000	67.8%
15.19	71.04	3000	68.3%
14.89	68.75	3000	68.0%
14.49	66.94	3000	68.7%
13.99	63.77	3000	69.4%
13.42	59.95	3000	69.1%
12.60	56.79	3000	69.7%
11.70	53.12	3000	69.7%
10.91	49.72	3000	65.6%
10.11	47.03	3000	63.7%
9.51	44.66	3000	61.1%
8.57	41.67	3000	55.3%
8.01	40.25	3000	49.6%
7.60	39.42	3000	44.2%
6.81	36.93	3000	30.4%

PAT	GIDD079
Category:	end-suction/volute (radial flow)
Outlet diameter, D:	0.125 m
Original source:	Giddens91

Turbine-mode BEP			
Q(l/s)	H(m)	N(rpm)	η
29.10	29.81	3000	78.6%

Performance data			
Q(l/s)	H(m)	N(rpm)	η
30.78	33.07	3000	78.4%
29.68	31.18	3000	78.2%
29.20	30.00	3000	78.5%
29.00	29.60	3000	78.5%
28.51	28.70	3000	79.5%
27.99	27.79	3000	78.8%
27.37	26.77	3000	79.1%
26.99	26.09	3000	77.8%
25.88	24.68	3000	76.4%
24.78	23.48	3000	74.7%
23.87	22.07	3000	72.7%
22.68	20.58	3000	70.6%
20.39	18.39	3000	61.5%
18.80	17.60	3000	53.9%
17.60	16.50	3000	44.6%
16.09	15.29	3000	28.2%
14.81	14.51	3000	12.9%

PAT	HIDR044
Category:	end-suction/volute (radial flow)
Outlet diameter, D:	0.356 m
Original source:	Hidrostal90

Turbine-mode BEP			
Q(l/s)	H(m)	N(rpm)	η
109.10	78.24	1800	76.9%

Performance data			
Q(l/s)	H(m)	N(rpm)	η
115.80	83.87	1800	76.6%
112.30	81.00	1800	76.9%
108.20	77.32	1800	76.9%
102.20	72.84	1800	76.4%
95.90	69.17	1800	75.5%
89.60	65.80	1800	73.7%
83.50	63.08	1800	71.2%
77.70	60.85	1800	67.9%
73.00	59.24	1800	64.6%

Table A.6: PATs unique information (4/10).

PAT	JYOT054
Category:	end-suction/volute (radial flow)
Outlet diameter, D:	n/a
Original source:	Jyoti

Turbine-mode BEP			
Q(l/s)	H(m)	N(rpm)	η
17.10	44.52	3000	60.7%

Performance data			
Q(l/s)	H(m)	N(rpm)	η
16.09	39.13	3000	59.7%
15.43	36.70	3000	60.9%
13.80	30.09	3000	52.0%
12.76	26.73	3000	49.5%
11.22	23.43	3000	33.6%

PAT	KNAP063
Category:	end-suction/volute (radial flow)
Outlet diameter, D:	0.340 m
Original source:	Knapp41

Turbine-mode BEP			
Q(l/s)	H(m)	N(rpm)	η
267.3	128.7	2500	90.5%

Performance data			
Q(l/s)	H(m)	N(rpm)	η
234.9	103.8	0	0.0%
197.1	62.9	497	35.7%
199.9	62.9	746	51.9%
199.2	62.9	998	66.1%
250.2	98.9	1483	75.4%
230.5	89.9	1889	87.5%
238.5	98.9	2098	89.3%
119.8	27.0	1179	91.8%
214.8	89.9	2309	89.3%
218.8	98.9	2533	87.5%
127.1	36.0	1556	85.6%
204.9	98.9	2712	80.3%
133.9	45.0	1845	77.1%
140.7	54.0	2094	69.4%
145.8	62.9	2300	63.0%
151.5	71.9	2512	58.0%
156.0	80.9	2691	53.6%
160.0	89.9	2864	50.1%
164.5	98.9	3047	47.1%
139.8	89.9	3057	0.0%

PAT	KNAP067
Category:	end-suction/volute (radial flow)
Sub-category	(double volute)
Outlet diameter, D:	0.340 m
Original source:	Knapp41

Turbine-mode BEP			
Q(l/s)	H(m)	N(rpm)	η
268.30	116.20	2500	89.6%

Performance data			
Q(l/s)	H(m)	N(rpm)	η
234.8	75.6	0	0.0%
156.8	32.4	252	23.3%
159.3	33.2	497	44.1%
161.3	34.6	746	62.7%
242.3	80.9	1400	72.3%
236.6	80.9	1663	81.3%
231.9	80.9	1832	85.8%
228.2	80.9	1961	88.6%
216.2	80.9	2253	90.6%
211.0	80.9	2343	88.6%
181.0	62.9	2115	87.1%
182.6	66.2	2213	85.8%
185.1	71.9	2346	82.7%
187.6	80.9	2533	78.3%
191.2	89.9	2688	73.4%
194.3	98.9	2854	69.7%
197.3	107.9	2998	66.1%
150.3	80.9	2691	51.9%
110.9	80.9	2903	0.0%

Table A.7: PATs unique information (5/10).

PAT	LAUX039
Category:	end-suction/volute (radial flow)
Outlet diameter, D:	n/a
Original source:	Laux80

Turbine-mode BEP			
Q(l/s)	H(m)	N(rpm)	η
1.409	1.487	664.4	85.4%

Performance data			
Q(l/s)	H(m)	N(rpm)	η
1.604	1.804	664.4	82.9%
1.500	1.625	664.4	84.6%
1.374	1.438	664.4	85.0%
1.311	1.345	664.4	85.1%
1.257	1.275	664.4	84.5%
1.130	1.127	664.4	81.8%
0.999	0.990	664.4	76.9%
0.889	0.902	664.4	70.1%
0.758	0.810	664.4	57.6%
0.632	0.736	664.4	38.2%
0.502	0.678	664.4	10.5%
0.464	0.663	664.4	0.0%

PAT	LUEN043
Category:	end-suction/volute (radial flow)
Outlet diameter, D:	n/a
Original source:	Lueneberg85

Turbine-mode BEP			
Q(l/s)	H(m)	N(rpm)	η
1.349	1.659	734.6	71.0%

Performance data			
Q(l/s)	H(m)	N(rpm)	η
1.499	1.979	734.6	69.2%
1.396	1.755	734.6	70.3%
1.299	1.558	734.6	70.4%
1.196	1.385	734.6	69.9%
1.094	1.241	734.6	67.6%
0.996	1.130	734.6	63.0%
0.896	1.027	734.6	55.3%
0.796	0.947	734.6	45.4%
0.698	0.885	734.6	30.8%
0.600	0.836	734.6	5.5%
0.587	0.831	734.6	0.0%

PAT	MEIE056
Category:	end-suction/volute (radial flow)
Sub-category	(fixed vanes)
Outlet diameter, D:	n/a
Original source:	Meier82

Turbine-mode BEP			
Q(l/s)	H(m)	N(rpm)	η
1.095	0.923	813.8	86.1%

Performance data			
Q(l/s)	H(m)	N(rpm)	η
1.188	1.059	813.8	85.0%
1.168	1.027	813.8	85.4%
1.128	0.969	813.8	86.0%
1.086	0.910	813.8	86.4%
1.046	0.858	813.8	86.3%
1.006	0.805	813.8	86.1%
0.965	0.755	813.8	85.1%
0.925	0.706	813.8	83.7%
0.884	0.662	813.8	81.7%
0.843	0.619	813.8	79.2%

Table A.8: PATs unique information (6/10).

PAT	PECK098
Category:	end-suction/volute (radial flow)
Outlet diameter, D:	0.273 m
Original source:	Peck51

Turbine-mode BEP			
Q(l/s)	H(m)	N(rpm)	η
51.85	9.15	857	73.8%

Performance data			
Q(l/s)	H(m)	N(rpm)	η
37.74	9.15	0	0.0%
40.61	9.15	110	14.3%
43.24	9.15	222	27.4%
45.53	9.15	330	39.3%
47.47	9.15	436	50.1%
49.09	9.15	547	59.8%
50.26	9.15	654	66.7%
51.37	9.15	764	70.8%
51.88	9.15	873	73.6%
51.98	9.15	986	72.3%
49.95	9.15	1096	61.3%
46.23	9.15	1204	36.7%
40.67	9.15	1290	0.0%

PAT	SANT050
Category:	end-suction/volute (radial flow)
Outlet diameter, D:	0.200 m
Original source:	Santolaria92

Turbine-mode BEP			
Q(l/s)	H(m)	N(rpm)	η
32.95	50.58	2000	63.4%

Performance data			
Q(l/s)	H(m)	N(rpm)	η
40.90	78.77	2000	59.3%
39.38	72.67	2000	60.7%
37.84	67.30	2000	61.9%
36.43	61.56	2000	62.8%
34.87	56.56	2000	63.4%
33.67	52.31	2000	63.5%
32.49	49.17	2000	63.6%
31.34	45.41	2000	63.0%
29.90	42.41	2000	62.2%
28.57	38.93	2000	61.1%
27.19	35.97	2000	58.4%
25.03	32.43	2000	55.0%
22.88	29.10	2000	50.0%
20.25	25.91	2000	42.4%
17.84	22.72	2000	31.2%
14.55	20.17	2000	10.2%

PAT	SCHM027
Category:	end-suction/volute (radial flow)
Outlet diameter, D:	0.250 m
Original source:	Schmied83

Turbine-mode BEP			
Q(l/s)	H(m)	N(rpm)	η
11.88	21.74	1000	65.4%

Performance data			
Q(l/s)	H(m)	N(rpm)	η
15.31	31.99	1000	60.5%
14.80	30.20	1000	61.3%
14.27	28.76	1000	62.6%
13.96	27.72	1000	63.1%
13.48	26.25	1000	64.0%
12.91	24.58	1000	64.8%
12.37	23.12	1000	65.3%
11.78	21.59	1000	65.9%
11.19	20.25	1000	65.8%
10.57	18.67	1000	65.1%
9.80	16.95	1000	64.1%
8.92	15.27	1000	61.8%
8.32	14.07	1000	58.4%
7.53	12.92	1000	54.3%
6.84	12.14	1000	47.1%
5.54	11.16	1000	32.0%
3.73	10.15	1000	0.0%

Table A.9: PATs unique information (7/10).

PAT	SENU037
Category:	end-suction/volute (radial flow)
Sub-category:	(semi-open impeller)
Outlet diameter, D:	0.1014 m
Original source:	Senu90

Turbine-mode BEP			
Q(l/s)	H(m)	N(rpm)	η
2.801	29.14	2500	53.6%

Performance data			
Q(l/s)	H(m)	N(rpm)	η
3.180	35.27	2500	51.8%
3.000	33.13	2500	53.2%
2.900	30.99	2500	53.4%
2.800	29.26	2500	54.3%
2.700	27.32	2500	55.5%
2.600	25.38	2500	56.7%
2.500	24.06	2500	54.2%
2.400	22.83	2500	50.6%
2.300	21.51	2500	49.0%
2.200	20.59	2500	47.7%
2.100	19.16	2500	46.0%
2.000	18.25	2500	44.6%
1.900	16.82	2500	42.7%
1.800	16.11	2500	41.0%
1.700	14.88	2500	38.3%
1.600	14.17	2500	35.0%
1.500	13.25	2500	27.8%

PAT	STRA022
Category:	end-suction/volute (radial flow)
Outlet diameter, D:	0.320 m
Original source:	Strate90

Turbine-mode BEP			
Q(l/s)	H(m)	N(rpm)	η
12.19	27.98	920	51.9%

Performance data			
Q(l/s)	H(m)	N(rpm)	η
11.20	18.15	0	0.0%
19.11	56.24	920	44.4%
16.78	45.30	920	48.3%
12.98	30.73	920	52.1%
12.71	30.13	920	52.4%
12.30	28.38	920	52.4%
10.24	22.01	920	51.0%
8.18	17.32	920	44.9%
6.15	14.23	920	24.4%
5.12	13.21	920	0.0%

PAT	STRA043
Category:	end-suction/volute (radial flow)
Outlet diameter, D:	0.334 m
Original source:	Strate90

Turbine-mode BEP			
Q(l/s)	H(m)	N(rpm)	η
63.39	49.01	1500	80.5%

Performance data			
Q(l/s)	H(m)	N(rpm)	η
80.11	40.43	1500	69.4%
70.18	31.70	1500	74.5%
60.00	24.77	1500	77.5%
58.68	23.66	1500	77.8%
57.55	22.72	1500	78.1%
56.83	22.48	1500	78.1%
56.05	22.07	1500	77.9%
55.05	21.64	1500	77.9%
54.24	21.12	1500	77.9%
53.34	20.71	1500	77.6%
50.06	18.72	1500	76.4%
43.59	15.47	1500	73.2%
33.45	12.50	1500	53.7%
22.63	10.37	1500	0.0%

Table A.10: PATs unique information (8/10).

PAT	STRA081
Category:	end-suction/volute (radial flow)
Outlet diameter, D:	0.219 m
Original source:	Strate90

Turbine-mode BEP			
Q(l/s)	H(m)	N(rpm)	η
56.150	22.11	1500	77.9%

Performance data			
Q(l/s)	H(m)	N(rpm)	η
80.11	40.43	1500	69.4%
70.18	31.70	1500	74.5%
60.00	24.77	1500	77.5%
58.68	23.66	1500	77.8%
57.55	22.72	1500	78.1%
56.83	22.48	1500	78.1%
56.05	22.07	1500	77.9%
55.05	21.64	1500	77.9%
54.24	21.12	1500	77.9%
53.34	20.71	1500	77.6%
50.06	18.72	1500	76.4%
43.59	15.47	1500	73.2%
33.45	12.50	1500	53.7%
22.63	10.37	1500	0.0%

PAT	STRU051
Category:	end-suction/volute (radial flow)
Outlet diameter, D:	n/a
Original source:	Strub59

Turbine-mode BEP			
Q(l/s)	H(m)	N(rpm)	η
1.305	1.274	866.8	85.6%

Performance data			
Q(l/s)	H(m)	N(rpm)	η
1.669	1.950	867	80.6%
1.495	1.598	867	83.9%
1.319	1.304	867	85.6%
1.230	1.175	867	86.1%
1.142	1.046	867	85.6%
0.967	0.828	867	79.4%
0.791	0.681	867	61.1%
0.617	0.623	867	30.0%
0.499	0.599	867	0.0%

PAT	THOM062
Category:	end-suction/volute (radial flow)
Outlet diameter, D:	n/a
Original source:	Thoma31 Kittredge31

Turbine-mode BEP			
Q(l/s)	H(m)	N(rpm)	η
14.16	8.043	1060	79.9%

Performance data			
Q(l/s)	H(m)	N(rpm)	η
9.74	5.490	1060	67.4%
5.30	4.062	1060	12.5%
4.45	3.876	1060	0.0%

Table A.11: PATs unique information (9/10).

PAT	VENT084
Category:	end-suction/volute (radial flow)
Outlet diameter, D:	0.280 m
Original source:	Ventrome82

Turbine-mode BEP			
Q(l/s)	H(m)	N(rpm)	η
120.5	34.00	1550	77.9%

Performance data			
Q(l/s)	H(m)	N(rpm)	η
138.8	43.61	1550	75.8%
132.5	40.06	1550	77.1%
122.0	34.83	1550	78.1%
117.9	32.85	1550	77.9%
103.3	26.66	1550	75.0%
88.7	22.13	1550	66.8%

PAT	WILL026
Category:	end-suction/volute (radial flow)
Outlet diameter, D:	0.134 m
Original source:	Williams82

Turbine-mode BEP			
Q(l/s)	H(m)	N(rpm)	η
3.754	55.86	3100	47.0%

Performance data			
Q(l/s)	H(m)	N(rpm)	η
3.902	59.42	3100	46.7%
3.875	58.16	3100	46.4%
3.795	56.33	3100	46.6%
3.715	56.11	3100	46.2%
3.634	53.36	3100	47.6%
3.501	50.51	3100	47.5%
3.367	47.99	3100	46.0%
3.153	44.79	3100	46.6%
2.913	41.71	3100	42.4%
2.512	37.25	3100	36.7%
2.378	35.42	3100	29.6%
1.951	31.42	3100	0.0%

PAT	YEDI038
Category:	end-suction/volute (radial flow)
Outlet diameter, D:	0.127 m
Original source:	Yedidah83

Turbine-mode BEP			
Q(l/s)	H(m)	N(rpm)	η
11.53	61.4	3550	65.0%

Performance data			
Q(l/s)	H(m)	N(rpm)	η
21.67	184.0	3550	47.9%
18.61	134.2	3550	53.2%
14.89	89.2	3550	61.6%
10.59	56.3	3550	63.9%
8.64	44.4	3550	60.6%
6.76	38.3	3550	46.4%

Table A.12: PATs unique information (10/10).

A.4 Case group division

Case	Ω_M	$\Delta\Omega_M$	$\Delta\Omega_M > 0.05$
1	0.117	0.041	-
2	0.158	0.000	-
3	0.158	0.000	-
4	0.158	0.000	-
5	0.158	0.018	-
6	0.176	0.000	-
7	0.176	0.000	-
8	0.176	0.000	-
9	0.176	0.023	-
10	0.199	0.000	-
11	0.199	0.000	-
12	0.199	0.006	-
13	0.205	0.000	-
14	0.205	0.015	-
15	0.220	0.075	0.075
16	0.295	0.033	-
17	0.328	0.000	-
18	0.328	0.000	-
19	0.328	0.034	-
20	0.362	0.000	-
21	0.362	0.000	-
22	0.362	0.041	-
23	0.403	0.000	-
24	0.403	0.024	-
25	0.427	0.066	0.066
26	0.493	0.018	-
27	0.511	0.000	-
28	0.511	0.029	-
29	0.540	0.099	0.099
30	0.639	0.020	-
31	0.659	0.032	-
32	0.691	0.000	-
33	0.691	0.005	-
34	0.696	0.005	-
35	0.701	0.000	-
36	0.701	0.000	-
37	0.701	0.021	-
38	0.722	0.036	-
39	0.758	0.131	0.131
40	0.889		

Table A.13: Specific speed difference between cases that leads to the case group division adopted in this thesis.

A.5 Specific speed influence on the PAT efficiency

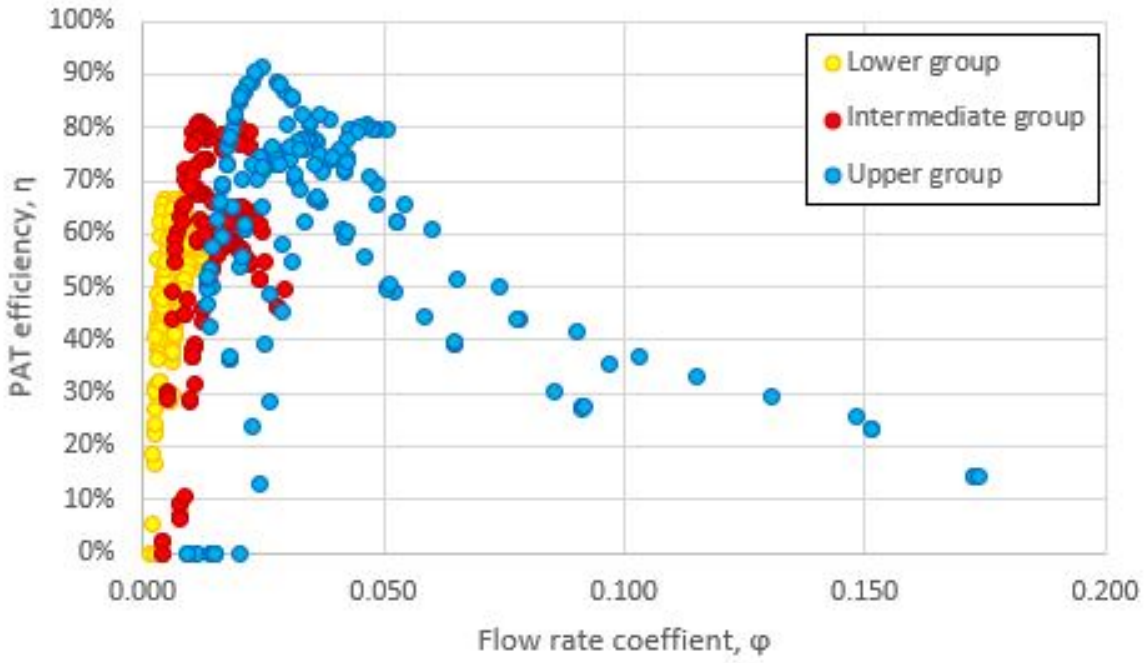

Figure A.1: PAT efficiency as a function of the flow rate coefficient Φ.

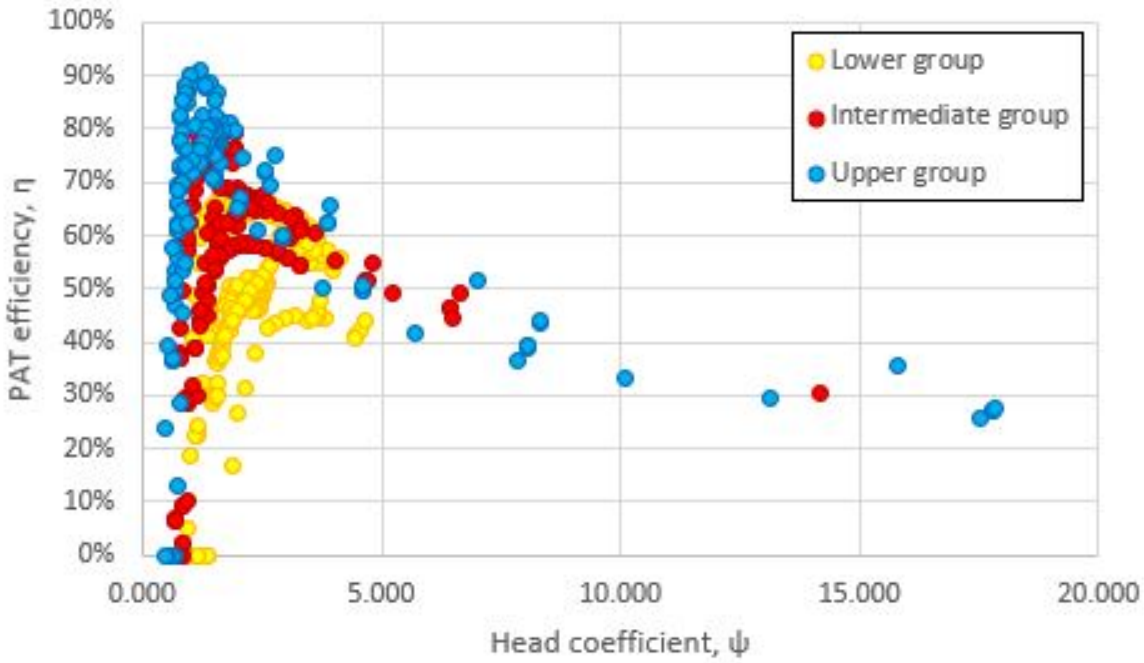

Figure A.2: PAT efficiency as a function of the head coefficient Ψ.

Appendix B

SPATEC Program

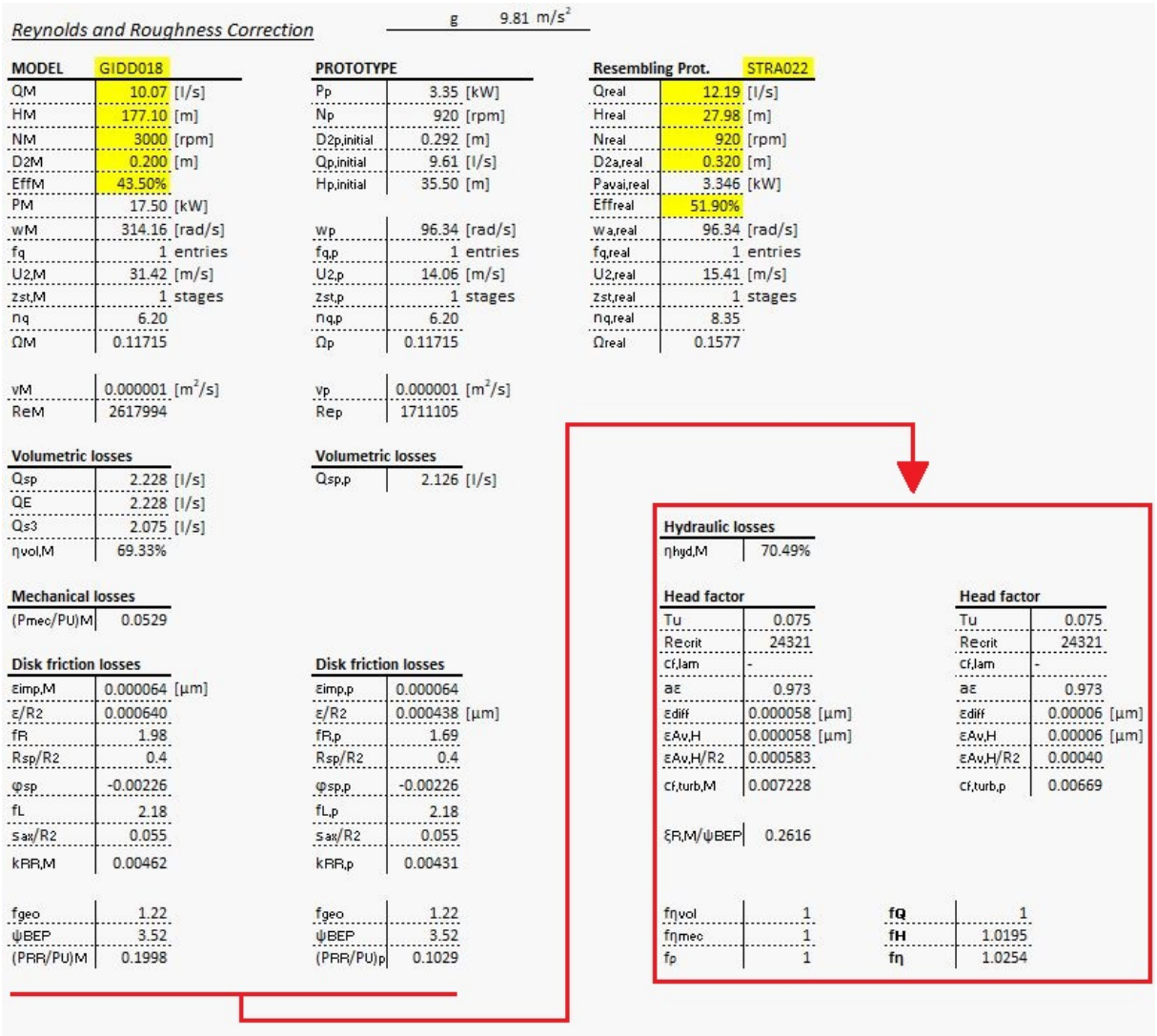

Reynolds and Roughness Correction

g 9.81 m/s²

MODEL	GIDD018	
QM	10.07	[l/s]
HM	177.10	[m]
NM	3000	[rpm]
D2M	0.200	[m]
EffM	43.50%	
PM	17.50	[kW]
ωM	314.16	[rad/s]
fq	1	entries
U2,M	31.42	[m/s]
zst,M	1	stages
nq	6.20	
ΩM	0.11715	
νM	0.000001	[m²/s]
ReM	2617994	

PROTOTYPE		
Pp	3.35	[kW]
Np	920	[rpm]
D2p,initial	0.292	[m]
Qp,initial	9.61	[l/s]
Hp,initial	35.50	[m]
ωp	96.34	[rad/s]
fq,p	1	entries
U2,p	14.06	[m/s]
zst,p	1	stages
nq,p	6.20	
Ωp	0.11715	
νp	0.000001	[m²/s]
Rep	1711105	

Resembling Prot.	STRA022	
Qreal	12.19	[l/s]
Hreal	27.98	[m]
Nreal	920	[rpm]
D2a,real	0.320	[m]
Pavai,real	3.346	[kW]
Effreal	51.90%	
ωa,real	96.34	[rad/s]
fq,real	1	entries
U2,real	15.41	[m/s]
zst,real	1	stages
nq,real	8.35	
Ωreal	0.1577	

Volumetric losses

Qsp	2.228	[l/s]
QE	2.228	[l/s]
Qs3	2.075	[l/s]
ηvol,M	69.33%	

Volumetric losses

Qsp,p	2.126	[l/s]

Mechanical losses

(Pmec/PU)M	0.0529

Disk friction losses

εimp,M	0.000064	[µm]
ε/R2	0.000640	
fR	1.98	
Rsp/R2	0.4	
φsp	-0.00226	
fL	2.18	
sax/R2	0.055	
kRR,M	0.00462	
fgeo	1.22	
ψBEP	3.52	
(PRR/PU)M	0.1998	

Disk friction losses

εimp,p	0.000064	
ε/R2	0.000438	[µm]
fR,p	1.69	
Rsp/R2	0.4	
φsp,p	-0.00226	
fL,p	2.18	
sax/R2	0.055	
kRR,p	0.00431	
fgeo	1.22	
ψBEP	3.52	
(PRR/PU)p	0.1029	

Hydraulic losses

ηhyd,M	70.49%

Head factor

Tu	0.075	
Recrit	24321	
Cf,lam	-	
aε	0.973	
εdiff	0.000058	[µm]
εAv,H	0.000058	[µm]
εAv,H/R2	0.000583	
Cf,turb,M	0.007228	
ξR,M/ψBEP	0.2616	
fηvol	1	
fηmec	1	
fp	1	

Head factor

Tu	0.075	
Recrit	24321	
Cf,lam	-	
aε	0.973	
εdiff	0.00006	[µm]
εAv,H	0.00006	[µm]
εAv,H/R2	0.00040	
Cf,turb,p	0.00669	
fQ	1	
fH	1.0195	
fη	1.0254	

Figure B.1: SPATEC program (only containing the roughness and Reynolds correction part).

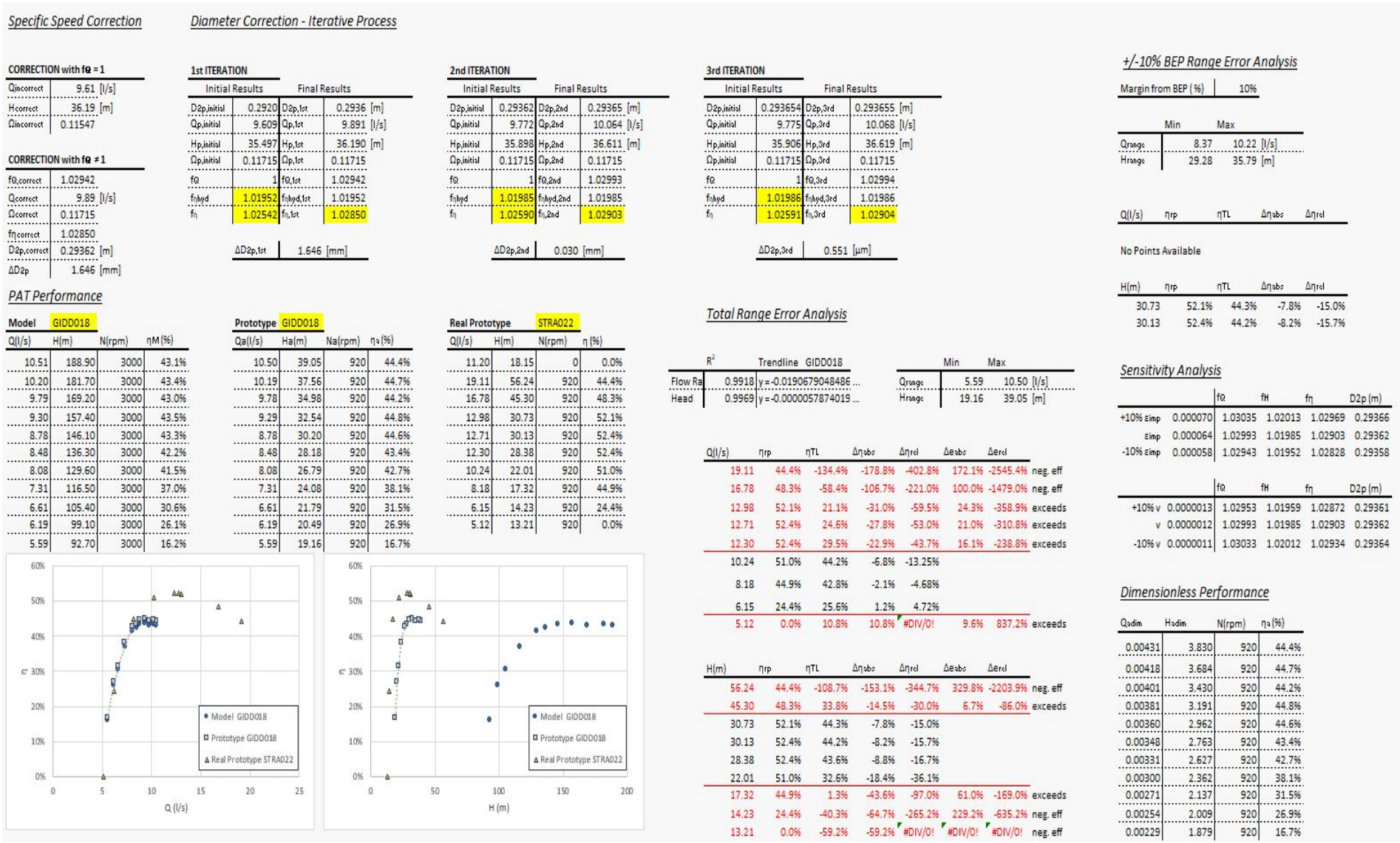

Figure B.2: SPATEC program (continuation).

Appendix C

Trendline polynomial degrees

The results presented in Tables C.1 to C.6 are the outcome of a series of detailed measurements on the determination coefficient R^2 for both efficiency curves throughout the 40 cases defined in this thesis. For each efficiency curve, it was selected the determination coefficient corresponding to each polynomial degree. Afterwards, the values were organized according to the lower, intermediate and upper groups. The lowest determination coefficient verified in a case group is illustrated in the column R^2 of each table.

Note that the polynomial degree that is verified before ΔR^2_{rel} reaches a value lower than 10%, is considered as the most suitable polynomial degree to fit the efficiency curve. In each table, the arrow indicates the polynomial degree that must be chosen.

	Polynomial degree	R^2	ΔR^2_{abs}	ΔR^2_{rel}
$\Longrightarrow$	2°	>0.9017	0.0684	7.59%
	3°	>0.9701	0.0057	0.59%
	4°	>0.9758	0.0169	1.73%
	5°	>0.9927	0.0003	0.03%
	6°	>0.9930		

Table C.1: Variation of the determination coefficient as a function of the trendline polynomial degree, for the flow rate efficiency curves of the lower gourp.

	Polynomial degree	R^2	ΔR^2_{abs}	ΔR^2_{rel}
	2°	>0.7057	0.1403	19.76%
	3°	>0.8460	0.1041	12.25%
$\Longrightarrow$	4°	>0.9501	0.0348	3.66%
	5°	>0.9849	0.0094	0.96%
	6°	>0.9943		

Table C.2: Variation of the determination coefficient as a function of the trendline polynomial degree, for the head efficiency curves of the lower group.

Polynomial degree	R^2	ΔR^2_{abs}	ΔR^2_{rel}
2°	>0.7850	0.1989	25.34%
3°	>0.9839	0.0081	0.82%
4°	>0.9920	0.0062	0.63%
5°	>0.9982	0.0001	0.01%
6°	>0.9983		

$\Longrightarrow$

Table C.3: Variation of the determination coefficient as a function of the trendline polynomial degree, for the flow rate efficiency curves of the intermediate group.

Polynomial degree	R^2	ΔR^2_{abs}	ΔR^2_{rel}
2°	>0.4531	0.3245	71.62%
3°	>0.7776	0.1496	19.24%
4°	>0.9266	0.0637	6.87%
5°	>0.9903	0.0009	0.09%
6°	>0.9912		

$\Longrightarrow$

Table C.4: Variation of the determination coefficient as a function of the trendline polynomial degree, for the head efficiency curves of the intermediate group.

Polynomial degree	R^2	ΔR^2_{abs}	ΔR^2_{rel}
2°	>0.2479	0.3468	139.90%
3°	>0.5947	0.2978	50.08%
4°	>0.8925	0.0835	9.36%
5°	>0.9760	0.0107	1.10%
6°	>0.9867		

$\Longrightarrow$

Table C.5: Variation of the determination coefficient as a function of the trendline polynomial degree, for the flow rate efficiency curves of the upper group.

Polynomial degree	R^2	ΔR^2_{abs}	ΔR^2_{rel}
2°	>0.1236	0.1564	126.54%
3°	>0.2800	0.1609	57.46%
4°	>0.4409	0.1631	36.99%
5°	>0.6040	0.1345	22.27%
6°	>0.7385		

$\Longrightarrow$

Table C.6: Variation of the determination coefficient as a function of the trendline polynomial degree, for the head efficiency curves of the upper group.